OPTIMIZATION OF FLUORESCENCE LIFETIME IMAGING MICROSCOPY (FLIM) FOR STUDYING THE ACTIVITY OF ENZYMES IN LIVE CANCER CELLS

BY

JOHN PAUL EICHORST

DISSERTATION

Submitted in partial fulfillment of the requirements
for the degree of Doctor of Philosophy in Biophysics and Computational Biology
in the Graduate College of the
University of Illinois at Urbana-Champaign, 2013

Urbana, Illinois

Doctoral Committee:

Associate Professor Yingxiao Wang, Chair
Professor Steve Granick
Professor Robert B. Gennis
Assistant Professor Kimani C. Toussaint Jr.

Abstract

This dissertation describes the process of optimizing a Fluorescence Lifetime Imaging Microscopy (FLIM) system in order to observe the dynamics of enzymes in live cancer cells. The enzyme studied throughout this research is Membrane Type 1 Matrix Metalloproteinase (MT1-MMP) which is a membrane-bound protein principally responsible for degrading extra-cellular matrix (ECM) proteins in the local environment of a migrating cell. However, MT1-MMP has an intricate role in the regulation of the cell's migration separate from its simple proteolytic functions. In addition, the increased expression of MT1-MMP has been positively correlated with the invasive potential of tumor cells. In spite of the importance of MT1-MMP in understanding a cancer cell's decision making as it leaves a tumor, very few reports have quantitatively studied the activity of this enzyme in live cells. Even fewer reports have examined the spatiotemporal activity of MT1-MMP in live cells cultured in 3-dimensional settings such as matrices of ECM proteins. These 3-dimensional settings can parallel the environment encountered by metastasizing cells in tissues. Studying live cells in 3-dimensional matrices is crucial for biologically relevant investigations. A cell's morphology and migratory behavior can vary significantly when comparisons are made between cells cultured on two dimensional substrates and those cultured in 3-dimensional matrices. The purpose of this project was to understand the coordinated functions of MT1-MMP as live cancer cells interact with and move through a 3-dimensional matrix of ECM proteins. Specifically, we are ultimately interested in the spatiotemporal activation patterns of MT1-MMP in live cancer cells in order to build a quantitative (systems-level) model

describing MT1-MMP's role in the cell's decision making as it is leaves a tumor site.

Acknowledgments

I want to thank Dr. Glenn Fried and Dr. Mayandi Sivaguru for their patience and generosity towards both my education and my research throughout my years in graduate school. I appreciate the support of many people in the labs of Professor Robert Clegg and Associate Professor Yingxiao Wang including Kai Wen Teng, Wagner Shin Nishitani, Jie Sun, Bryan Spring, Ulai Noomnarm, Jihye Seong, He Huang Li-Jung Lin, Yi Wang, Taejin Kim, Lei Lei Yue Zhou, Hao Cai, Kathy Lu and David Park. I am extremely grateful to both Eugene Colla and Jack Boparai in the Physics department for their support and encouragement in the development and teaching of several physics courses. Without the material resources and assistance from Associate Professor Yingxiao Wang and his efforts publishing articles, none of these investigations would have been possible. Prof. Clegg introduced me to the usefulness of lifetime imaging and encouraged my efforts in this area as well. I also thank all of the students that I have taught during my teaching assistantships so that I could have the financial means to support myself. I appreciate very much the efforts of Cindy Dodds helping me through the requirements in Biophysics. Most of all, I thank my parents for sacrificing so much throughout my life so that both I and my sisters had the opportunities for higher education.

Table of Contents

Chapter 1

Overview and Background of the Dissertation

Introduction

The MT1-MMP enzyme can be monitored in a live cell using an intracellular genetically-encoded biosensor developed in the lab of Yingxiao Wang [1, 2]. The biosensor contains two fluorescent proteins and a protein sequence specific for the catalytic domain of MT1-MMP. The fluorescence emission of the biosensor changes in both color and intensity when a nearby active MT1-MMP enzyme interacts with it, allowing for the active and inactive states of the enzyme to be detected.

In order to obtain a physically robust mapping of the biosensor's configuration in images of live cells, Fluorescence Lifetime Imaging Microscopy (FLIM) was used to monitor the activation of the biosensor [3-5]. Unlike methods that detect the average (steady-state) fluorescence emitted by a sample [6-10], a lifetime measurement relates the time an electron spends in the excited state by recording time-dependent features of the fluorescence emission [11-14]. Lifetime measurements are absolute measurements and therefore, do not require the extensive corrections needed to equate measured steady-state intensities to physical parameters describing the sample. However, measuring lifetimes in an image often requires multiple exposures of the sample to the exciting light in order to generate a single lifetime image. As a result, the temporal resolution of lifetime imaging is fundamentally degraded and live samples can be readily damaged by the effects of photoxicity and photobleaching during imaging sessions. Throughout the literature

describing the study of live cells with lifetime imaging, extended imaging sessions that regularly monitor the activity of proteins for periods of an hour are simply not possible.

In the course of this research, considerable work has been undertaken to improve the speed and contrast of the FLIM system with a technique referred to as phase suppression [3-5, 15-20]. Phase suppression requires only two brief exposures of the sample to spatially highlight features in an image according to phase (indicative of the lifetime). This technique was crucial to monitoring the kinetics of our biosensor without incurring excessive photo-damage to the cells. New instrument control software has reduced the image acquisition to one tenth of that of the original system. In parallel, improved analysis of spatial frequencies within the image has increased the certainty when assigning pixels to specific configurations of the biosensor. With the lifetime distributions of the fluorescent proteins used in this project (mOrange2/mCherry), I was able to quantitatively show an equivalence between the traditional analysis of each configuration of the biosensor using the polar plot and separately using phase suppression. At this time, the activity of the MT1-MMP enzyme can be monitored with images acquired at nearly twenty time points over the period of an hour.

Furthermore, in this dissertation, a novel combination of computational analysis and experimentation has provided new insights for selecting fluorescent proteins for these types of applications. The selection of fluorescent proteins dictates the contrast and resolution of the two configurations of the biosensor when detected in live cells. With a combination of quantitative steady-state, lifetime and spectral imaging, new conclusions are presented about the problems and complications that arise specifically when the enhanced cyan fluorescent protein (ECFP) and the yellow fluorescent protein for FRET

(Förster Resonance Energy Transfer) (YPet) proteins are used for FRET-based studies in live cells. This research furthermore addresses the long-standing problem about why apparent large changes in energy transfer are observed when the proteins are examined with steady-state techniques, but not when studied with lifetime imaging.

This chapter begins with an introduction to the MT1-MMP enzyme and the biology of cancer. Following sections establish the fundamentals behind the theory and instrumentation for measuring lifetimes in the microscope. In the second chapter, the analysis of the MT1-MMP biosensor containing the cyan and yellow fluorescent proteins is presented in conjunction with the theory of measuring energy transfer. The third chapter of the dissertation describes the experiments and optimization of the existing FLIM system to study the dynamics of live cancer cells containing the long wavelength variant (mOrange2/mCherry) of the MT1-MMP biosensor. A final chapter is provided where a series of new experiments developed for teaching graduate students the principles of measuring time-dependent fluorescence are presented.

Biological Motivation

MT1-MMP and the Biology of Cancer

When cancerous cells become metastatic, they migrate from a tumor and invade neighboring tissues. In order to migrate and eventually invade neighboring tissues, a cancer cell must initially break through the matrix of proteins surrounding a tumor and migrate toward a blood vessel. Dense mesh works of collagen located throughout tissues comprise the most abundant mechanical barriers for invading cells. Consequently, these metastatic cells must be able to negotiate through the extra-cellular matrix (ECM)

surrounding the cell as well as coordinate the activity of the cell's own migratory mechanism. Collagen-I, being the most abundant protein in the ECM, represents a substantial barrier for metastatic cells. Recently, the enzyme MT1-MMP has generated great interest in the study of metastasis because of its ability to not only degrade collagen in the ECM but also to regulate signaling cascades responsible for migration and the cell's communications with its local environment [21-25]. However, MT1-MMP's role in regulating and promoting invasiveness is not established but at the same time, the over-expression of MT1-MMP has been positively correlated with metastatic potential of tumor cells [26-28].

Structurally, MT1-MMP is a membrane-bound enzyme consisting of three domains which include a cytosolic domain, an ECM protein binding domain referred to as the hemopexin domain and a catalytic domain containing the active zinc site (Fig. 1.1) [29]. It is known that many functions and interactions of MT1-MMP not directly associated with the degradation of ECM proteins can inhibit and enhance an invasive cell's migration [24]. More specifically, the functions of MT1-MMP during metastatic events stem from MT1-MMP's effect on and relationships to other proteins and enzymes in various signal transduction cascades. Kinases such as Src [30] which are responsible the turnover and development of adhesion sites, have been implicated as possibly interacting with MT1-MMP's cytosolic tail to modulate its function. In addition, MT1-MMP's role regulating migration has been linked to its internalization at the membrane [31], its ability to control the shedding of other membrane proteins such as CD44 [32] and syndecan-I [33] and possibly its processing of the products of ECM destruction. Some have even suggested that the site of proteolysis of collagen for cells containing

MT1-MMP is not along the leading edge at all, but posterior to it [34]. In any case, understanding the spatiotemporal activation patterns of MT1-MMP is crucial in order to develop a complete model of its biochemical functions in cells that direct events necessary for metastasis and invasion.

Previous Studies of MT1-MMP in Live Cells

Recent studies have emphasized the importance of studying live cells in 3-dimensional settings [35-37]. Striking differences in the morphology, migratory patterns and adhesion formation exist when comparing cells cultured in 2-dimensional settings to those growing in 3-dimensional constructs. In this research, the adhesion sites which mediate the cell's contact with the ECM are essential areas to study in order to learn MT1-MMP's role in translating features from the local environment into cues directing the cell's behavior.

Previous attempts to study the activity of MT1-MMP in live cells have included novel sensors tethered to collagen as well as a set of intracellular biosensors. Interestingly, studies using sensors tethered to the collagen to monitor a variety of cancer cells migrating in 3D matrices of collagen indicated that MT1-MMP is likely active along the leading edge of the cell [36]. The biosensor used in this study was targeted for multiple MMPs including but not exclusively specific for MT1-MMP. An intracellular biosensor developed by Ouyang et al. monitored the activation of MT1-MMP following stimulation by the Epidermal Growth Factor (EGF) [2]. This biosensor was genetically encoded and labeled the cell's entire membrane simplifying the process of correlating MT1-MMP's activity to specific sub-cellular structures and organelles. The active MT1-MMP enzyme, visualized with this biosensor was present primarily along the periphery

of HeLa cells. In this case however, the active MT1-MMP enzyme was exogenously introduced into the HeLa cells. However, in this dissertation, the activity of MT1-MMP was monitored using the biosensor developed by Ouyang et al (Fig. 1.2). Although other reports exist that studied the localization of MT1-MMP in live cells, very few have quantitatively examined its activity in settings similar to those encountered by invasive cancer cells (e.g. matrix of collagen).

HT-1080 cells

Throughout this research, the MT1-MMP biosensor has been and will continue to be examined in HT1080 cells [38]. These cells were originally derived from a cancer in the soft tissue of a human male and have been established as a stable cell line. Although similar to fibroblasts, HT1080 cells lack contact inhibition potentially forming microtumors in the culture and endogenously express MT1-MMP. The metastatic potential of the HT1080 cells was demonstrated by early experiments where the cells were transplanted into NIH Swiss mice. Within a period of days of the transplantation, large tumors grew which demonstrated invasion of their surrounding tissues. As a result, HT1080 cells are characterized by many properties indicative of cancerous and metastatic cells, making them well-suited as the broad biological system to study for this work.

Fluorescence Lifetimes

Introduction

Fluorescence requires that electrons within a molecule change energies between singlet states referred to as the lowest unoccupied molecule orbital (LUMO) and the highest occupied molecular orbital (HOMO). Energy loss during this transition of

energies results in a lower energy photon being emitted after a higher energy photon was absorbed. In steady-state imaging, a continuous light source excites a volume of fluorescent molecules and the average intensity of the emitted fluorescence is detected. However, unlike steady-state measurements, a measured lifetime indicates the amount of time an electron spends in the excited state before returning to the ground state. Therefore, detailed information about the time-dependent emission of the fluorescent molecule is necessary to determine a lifetime. Lifetimes are very susceptible to factors in the local environment of the fluorescent molecule and as a result, make excellent measured criteria for analyzing complex biological systems.

Furthermore, lifetimes are absolute measurements that are characteristic of a molecule and require minimal corrections to extract. Intensities recorded from steady-state measurements vary from instrument to instrument. Careful control measurements and corrections can translate these intensities into an absolute (quantitative) form but at the same time, introduce cumulative uncertainties from each of the corrections applied.

The Fundamental Fluorescence Response

The lifetime of the fluorophore (fluorescent molecule) is the average amount of time that the fluorophore spends in the excited state. The manner by which a molecule returns to the ground state after being excited is physically modeled as a competitive first order kinetic rate process [11, 13]. Essentially, this model assumes that once a molecule has been excited, it reaches an approximate steady-state with respect to energy (at lowest vibrational level of lowest excited singlet state) before returning to the ground state. As this “steady-state” occurs, all available pathways of de-excitation are simultaneously competing to return the molecule to the ground state. These pathways are often indicative

of the fluorophore's local environment and represent processes such as non-radiative de-excitation, collisional quenching, FRET and possibly intersystem crossing to a triplet state. As a result, each pathway of de-excitation has an associated rate constant indicating how often it is used to return a molecule to the ground state. This rate constant is simply the probability per unit time that a pathway will be implemented to return an excited molecule to the ground state. Therefore, the probability that a fluorophore will remain in the excited state following a brief excitation decays exponentially in time.

Experimentally, the lifetime can be measured directly by exciting the molecule with a very brief (with respect to the lifetime) pulse of light and recording the fluorescent decay. The measured intensity at any point along the decay is proportional to the number of molecules remaining in the excited state at that time. The general equation for the fluorescent decay of a sample containing a set of fluorophores with different lifetimes is written Eq. (1),

$$F_{\delta}(t) = \sum_{i} \alpha_i e^{-t/\tau_i} \tag{1}$$

In Eq. (1), the factor (α_i) is proportional to the normalized concentration (referred to as species fraction) of fluorophore (i) with lifetime (τ_i).

In the above hypothetical experiment, the presence of additional pathways of de-excitation such as FRET does not change the magnitude of the rate constant associated with fluorescence emission. Therefore, at any specific time along the decay curve of the fluorescence emission, the number of molecules in the excited state is always proportional to the fluorescence intensity with the proportionality constant being the rate constant of the fluorescence emission. However, the presence of additional pathways of

de-excitation will increase the total probability that an excited molecule will leave the excited state and consequently, will shorten the lifetime of the observed decay.

Time-Domain

Most fluorophores studied in biology such as the fluorescent proteins [39], have lifetimes on the order of nanoseconds. Detecting the decay of fluorescence can be done with a technique referred to as time-correlated single photon counting (TCSPC) [12]. This technique requires extremely short pulses of excitation light and carefully synchronized detectors. Each detected photon needs to be correlated with the specific pulse that generated it. In other words, the system must be able to know the precise pulse that generated each detected photon. Likewise, the excitation pulses must be sufficiently spaced in time so that the decay instigated by a given pulse will have dampened in intensity sufficiently prior to the arrival of the next exciting pulse. Without sufficient spacing of the exciting pulses of light, the effects from the "pulse pile-up" can add significant artifacts to a measured lifetime.

Frequency Domain

A fluorophore's lifetime can be measured in the frequency domain by exciting the sample with light having its intensity repetitively modulated. Any waveform that consistently repeats over a given period can be used to modulate the intensity of the excitation light. This is because any sinusoidal constituent of an arbitrary repetitive waveform can be analyzed independently by Fourier analysis. However, for simplicity, the waveform modulating the intensity of the exciting light $E(t)$ can be assumed sinusoidal,

$$E(t) = E_o + E_\omega \cos(\omega_E t + \varphi_E) \tag{2}$$

In response to $E(t)$, the intensity fluorophore's emitted fluorescence $S(t)$ will also be sinusoidally modulated at a radial frequency (ω_E). However, the fluorescence emission of the sample is shifted in phase and de-modulated with respect to the excitation light.

$$S(t) = S_o + S_\omega \cos(\omega_E t - (\varphi - \varphi_E)) \tag{3}$$

De-modulation refers to a change in the amplitude of oscillation of the sinusoid with respect to the DC offset.

Both the shift in phase delay (φ) and modulation ratio (M) are functionally dependent on the lifetime of the sample.

$$\varphi = \tan^{-1}(\omega_E \tau_\varphi) \tag{4}$$

$$M = \frac{S_\omega / S_o}{E_\omega / E_o} = \frac{1}{\sqrt{1 + (\omega_E \tau_M)^2}} \tag{5}$$

The relationships described in Eqs. (4) and (5) can be derived by convoluting the fluorophore's fundamental fluorescence response (Eq. 1) with the waveform of the exciting light's intensity (Eq. 2). The convolution assumes that at each infinitesimally small piece of $E(t)$ produces an exponential decay indicative of the sample's lifetime. Equivalent equations relating the measured lifetime to the phase shift and de-modulation

of the sample's emitted fluorescence can be obtained by taking the Fourier Transform of the fundamental fluorescence response.

Very often, the equation describing the intensity modulated fluorescence of the sample $S(t)$, presented with a multiplicative constant accounting for the brightness or concentration of the sample. In this derivation, this factor has been omitted because the division by the DC offset in the calculation of the modulation ratio (M) eliminates this dependence.

Correcting Measurements taken in the Frequency Domain

Extracting the actual phase delay (φ) and modulation ratio (M) of an unknown fluorophore requires knowledge about the amplitude of oscillation and phase of the waveform modulating the intensity of the excitation light. For example, the value experimentally measured for the phase of an unknown fluorophore is equal to $(\varphi - \varphi_E)$. In order to find the phase delay of the fluorophore (φ), the phase of the excitation light (φ_E) must be added to the experimentally recorded value of the phase. Likewise, the calculation of a sample's modulation ratio (M) involves dividing the ratio of the amplitude of oscillation and the DC offset measured from the unknown fluorophore $\left(S_\omega / S_o\right)$ by that of the excitation light $\left(E_\omega / E_o\right)$. Values for $\left(E_\omega / E_o\right)$ and (φ_E) can be determined by measuring a fluorophore (referred to as the reference) with a known single lifetime. Several papers highlight fluorophores spanning a variety of excitation and emission wavelengths that can be used as references [12, 40]. In some cases, instrumental drift, changes in the gain of a detector or the output of the excitation source

can alter the values of $\left(E_\omega / E_o \right)$ and $\left(\varphi_E \right)$ during an experiment. It is therefore, prudent to measure the reference often during experiments.

Characterizing Different Lifetime Distributions

If a sample containing fluorophores is characterized by a single lifetime, the lifetime derived from the phase delay and modulation ratio will both equal the lifetime of the fluorophore itself. However, many of fluorophores applied to study biological systems are characterized by multiple discrete lifetimes as well as by continuous distributions of lifetimes. Examples of multi-component lifetimes include many of the fluorescent proteins such as the Enhanced Cyan Fluorescent Protein (ECFP) [16, 41-43]. In these cases, the lifetime extracted from the phase delay and the lifetime determined from the modulation ratio will not be equal. Neither of these lifetimes will equal the lifetime of any constituent of the sample.

Mathematically, the phase delay $\left(\varphi \right)$ and modulation ratio $\left(M \right)$ detected for the sample must be related to the constituent lifetimes present and their relative contributions. In order to make these relationships, the intensity-modulated fluorescence of the sample $S\left(t \right)$ detected can be re-written with dependencies on the constituent lifetimes as shown below,

$$S(t) = E_o \sum_i \alpha_i \tau_i + E_\omega \sum_i \frac{\alpha_i \tau_i}{\sqrt{1 + \left(\omega_E \tau_i \right)^2}} \cos(\omega_E t - (\varphi_i - \varphi_E)) \qquad (6)$$

In this equation, the coefficients (S_o) and (S_ω) from equation (2) are simply replaced by the functional dependencies that arise from the convolution integral. Each constituent lifetime contributes independently to the DC offset, amplitude of oscillation and detected phase shift. Therefore, regardless of the number of lifetimes present in the sample, only one modulation ratio and phase delay characteristic of the sample can be recorded. This can be seen by normalizing $S(t)$ by its DC offset (DC).

$$\frac{S(t)}{DC} = 1 + \frac{E_\omega}{E_o} \sum_i \frac{a_i}{\sqrt{1 + (\omega_E \tau_i)^2}} \cos(\omega_E t - (\varphi_i - \varphi_E)) \tag{7}$$

$$\frac{S(t)}{DC} = 1 + \frac{E_\omega}{E_o} M \cos(\omega_E t - (\varphi - \varphi_E)) \tag{8}$$

In equation (7), the factor (a_i) is the fractional contribution of the fluorescent emission from the species with lifetime (τ_i) to the steady-state intensity.

By measuring the phase, amplitude of oscillation and DC signal from $S(t)$ at a large set of modulation frequencies $\{\omega_E\}$, iterative fitting can determine the constituent lifetimes and their contributions to the measured signal [44-46]. The relationships between these features of the fluorescence emission of a sample resulting from intensity-modulated excitation and the corresponding constituent lifetimes of a fluorescent sample can be derived from Fourier analysis [11, 12, 14]. The fluorescence emission of a sample resulting from a repetitive excitation can be expressed as the Fourier transform of the normalized fundamental fluorescence response $F_\delta(t)$. The real part of the fluorescence

emission of sample at a modulation frequency (ω_n) can then be expressed as a sum of orthogonal basis functions weighted by the coefficients (A) and (B), defined as the cosine and sine transforms from the Fourier transform [47, 48].

$$A = \int_0^\infty F_\delta(t)\cos(\omega_n t)\,dt \tag{9}$$

$$B = \int_0^\infty F_\delta(t)\sin(\omega_n t)\,dt \tag{10}$$

The integrals in equations (9) and (10) do converge regardless of the lifetime distribution being analyzed[1]. Therefore, the fluorescence response of samples with extremely complicated lifetime distributions can be expressed in the frequency domain as a single sinusoidal function oscillating at a repetition frequency (ω_n) with a single amplitude of oscillation $M = \sqrt{A^2 + B^2}$ and phase $\varphi = \tan^{-1}\left(\frac{B}{A}\right)$. These relationships can be derived from the trigonometric identity, $A\cos(\omega_n t) + B\sin(\omega_n t) = \sqrt{A^2 + B^2}\cos(\omega_n t + \varphi)$ and are shown as a function of the constituent lifetimes and their fractional contributions in the following equations.

[1] The factor of $\left(\frac{1}{\sqrt{2\pi}}\right)$ has been omitted in equations (9) and (10). In frequency-domain FLIM, the harmonic response of the sample is compared to that of a fluorophore with a known single lifetime to compute the phase delay and modulation ratio. Therefore, this factor is not necessary.

$$\varphi = \tan^{-1}\left(\frac{\sum_s \frac{a_s \omega_n \tau_s}{1+(\omega_n \tau_s)^2}}{\sum_s \frac{a_s}{1+(\omega_n \tau_s)^2}}\right) \tag{11}$$

$$M = \sqrt{\left(\sum_s \frac{a_s}{1+(\omega_n \tau_s)^2}\right)^2 + \left(\sum_s \frac{a_s \omega_n \tau_s}{1+(\omega_n \tau_s)^2}\right)^2} \tag{12}$$

The weighting terms $[A, B]$ derived as the cosine and sine transforms can be considered as vectors in the space created by the orthogonal basis of a sine and cosine functions oscillating at a specific radial frequency (ω_n). Both the modulation ratio (M) and the phase delay (φ) of the sample can be determined graphically when $[A, B]$ are projected on a set of orthogonal axes. With two simulated lifetimes, the size of the resulting vector equivalent to the modulation ratio (M) and the corresponding phase delay (φ) can be found with vector addition. As will be discussed in later sections, the transformation to this space can simplify the analysis of lifetime images and can greatly reduce the acquisition time necessary to characterize a fluorescent sample.

Frequency Mixing

Many of the common fluorophores applied in biology have lifetimes on the order of nanoseconds. As a result, the intensity-modulated fluorescence emission from these samples will not have a significant shift in phase or incur a change in the amplitude of oscillation (relative to that of the exciting light) unless modulation frequencies in the range of megahertz are used. Experimentally, the noise which is also present at those high frequencies will also be acquired if fluorescence signals oscillating in intensity at such

high frequencies are measured directly. Furthermore, most detectors such as the cameras found on imaging systems, do not have the temporal resolution necessary to acquire images at rates in the megahertz range [49].

A technique referred to as frequency mixing lowers the frequency of the repetitive signal from which the modulation ratio and phase delay of the sample can be determined [3, 5, 45, 50]. In order to apply frequency mixing, a separate radio frequency is injected into the gain of the detector (referred to as $G(t)$). In other words, the gain of the detector is then increased or decreased repetitively during an experiment according to the following equation.

$$G(t) = G_o + 2G_\omega \cos(\omega_G t + \varphi_G) \tag{13}$$

The acquired signal is then the product of the function modulating the detector's gain $G(t)$ and intensity modulated fluorescence emission $S(t)$. The terms resulting from this multiplication $\left(G(t) \bullet S(t)\right)$, include a term (sinusoidal function) oscillating at the difference frequency $(\omega_G - \omega_E)$, a term with no time-dependence and high frequency terms oscillating at frequencies of (ω_E), (ω_G) and $(\omega_G + \omega_E)$.

If $\omega_E = \omega_G$, determining the phase delay and modulation ratio of the sample only requires the acquisition of a series of steady-state intensity images using a process referred to as homodyning. In this case, all high frequency terms average to zero during the acquisition times common to imaging (millisecond exposure times), leaving only the

DC offset term and the term oscillating at the difference frequency, which consequently has no time dependence as shown below,

$$[G(t) \bullet F(t)]_{LF} = G_o E_o \sum_s a_s \tau_s + 2G_\omega E_\omega \sum_s \frac{a_s \tau_s}{\sqrt{1+(\omega_E \tau_s)^2}} \cos\left((\omega_G - \omega_E)t + \varphi_G - \varphi_E + \varphi_s\right) \qquad (14)$$

When acquiring lifetimes by homodyning on the FLIM system, a series of images are collected at various phase shifts applied to the detector (φ_G) (referred to as detector phases) sampled evenly from 0 to 2π. Alternatively, the phase offset of $E(t)$ can be varied in a similar manner for homodyne detection provided that (φ_G) remains fixed.

The measured phase delay and modulation ratio are commonly determined on a pixel-wise basis by taking the Discrete Fourier Transform (DFT) of the set of images collected by homodyning or by iterative least square fitting the data to a sine wave. Since iterative fitting and digital Fourier Transform result in the same phase delay and modulation ratio, (and because DFT is faster), there is no need for iterative fitting techniques when determining the modulation ratio and the phase delay at any of the component frequencies [51].

The DFT analysis of the fluorescence signal will produce a single measured phase delay (φ) and modulation ratio (M) (see Eqs. 11 and 12). The process of relating (φ) and (M) to the intensities measured by homodyning begins by normalizing the function $[G(t) \bullet F(t)]_{LF,Homo}$ to its corresponding steady-state intensity (SS) as shown in equation (15).

$$\left(\frac{[G(t)\bullet F(t)]_{LF,Homo}}{SS}\right)=1+\frac{G_\omega E_\omega}{G_o E_o}Mcos\left(\varphi_G-\varphi_E+\varphi\right) \tag{15}$$

Experimentally, $\left(\frac{[G(t)\bullet F(t)]_{LF,Homo}}{SS}\right)$ is discretely sampled over a specific set of evenly spaced phase delays. The detector phases can be expressed as a function oscillating at a frequency that depends on the number of detector phases (N) sampled. If eight detector phases ($N = 8$; (N) could be larger or smaller, but must be at least 3) are used, then, for every value of (n), from $n = 0$ to $n = N - 1$

$$\left(\frac{[G(t)\bullet F(t)]_{LF,Homo}}{SS}\right)_n=1+\frac{G_\omega E_\omega}{G_o E_o}Mcos\left(\varphi_G^0+\left(\frac{\pi}{4}\right)n-\varphi_E+\varphi\right), \tag{16}$$

where $\left(\varphi_G^0\right)$ is the phase of the intensifier modulation when $n = 0$. The average intensity over the repetition period is also measured at every pixel.

The amplitude of oscillation $\left(\frac{G_\omega E_\omega}{G_o E_o}M\right)$ and the phase delay value $\left(\varphi_G^0-\varphi_E+\varphi\right)$ can be calculated by taking the digital sine and cosine transforms (Eqs. 17 and 18) using the measured values $\left(\frac{[G(t)\bullet F(t)]_{LF,Homo}}{SS}\right)_n$ over the n values of the measurement.

$$F_{sin,i}=\sum_{n=0}^{N-1}S_i\sin\left(\left(\frac{\pi}{4}\right)n\right) \tag{17}$$

$$F_{cos,i} = \sum_{n=0}^{N-1} S_i \cos\left(\left(\frac{\pi}{4}\right)n\right) \tag{18}$$

$\left(\varphi_G^0\right)$ and $\left(\varphi_E\right)$ are known, so $\left(\varphi\right)$ can be determined.

In heterodyne detection, the frequencies of the modulation of the detector's gain and that of the intensity modulation of the excitation differ typically only by a few hundred hertz (for the detection of nanosecond lifetimes). This difference frequency is often referred to as the cross-correlation frequency. Analog or digital filtering techniques can effectively determine the amplitude oscillation and phase offset of $[G(t) \bullet F(t)]_{LF}$ in order to find the phase delay and modulation ratio of the sample. Additionally, recent applications of heterodyne-based detection do exist that do not require direct modulation of the detector's gain, relying instead on detection with digital photon counting combined with heterodyning in the detection circuitry [52].

Polar Plot

As discussed previously, regardless of the number of lifetimes present in the sample or their contribution to the measured signal, the intensity-modulated fluorescent emission of the sample is characterized by a single modulation ratio and a single phase delay. In the case of imaging, measuring these values with a large set of modulation frequencies in order to derive specifics about the constituent lifetimes is not feasible and can result in the destruction of the sample (particularly when studying live samples). Recently, a model-free analysis called the polar plot can transform data collected in the frequency domain into a coordinate space from which conclusions about the fluorescent

species present can be graphically determined [44, 53-56]. The polar plot is generated from the raw data and does not require fitting or excessive corrections.

The polar plot transforms the phase delay and modulation ratio into a vector on the Cartesian plane. The derivation of the coordinate transforms of the polar plot begins by examining the intensity-modulated fluorescence of the sample normalized by it DC offset, $S(t)/DC$. In equation (19), it is assumed that the sample contains a set of fluorophores each having a distinct lifetime.

$$\frac{S(t)}{DC} = 1 + \frac{E_\omega}{E_o} \sum_i \alpha_i M_i \cos(\omega_E t - \varphi_i) \tag{19}$$

In equation (19), the factors (M_i) and (φ_i) are the modulation ratio and phase delay that would have been detected if each constituent fluorophore could be measured independently. As described previously, (a_i) is the fractional contribution that each lifetime component has to the measured steady-state intensity,

$$a_i = \frac{\alpha_i \tau_i}{\sum_i \alpha_i \tau_i} \tag{20}$$

Equivalently, the function $S(t)/DC$ can be written with a single modulation ratio and phase delay that result from the emission of all the constituent fluorophores in the sample.

$$\frac{S(t)}{DC} = 1 + \frac{E_\omega}{E_o} M \cos(\omega_E t - \varphi) \tag{21}$$

By applying simple algebraic manipulations, equations (19) and (21) can be re-written as follows,

$$\frac{E_o}{E_\omega}\left(\frac{S(t)}{DC} - 1\right) = M \cos(\omega_E t - \varphi) \tag{22}$$

$$\frac{E_o}{E_\omega}\left(\frac{S(t)}{DC} - 1\right) = \sum_i \alpha_i M_i \cos(\omega_E t - \varphi_i) \tag{23}$$

With a simple trigonometric identity, equation (22) can be re-written in the form,

$$M \cos(\omega_E t - \varphi) = M \cos(\omega_E t)\cos(\varphi) + M \sin(\omega_E t)\sin(\varphi)\,. \tag{24}$$

In this representation, the term $\left(M \cos\left(\omega_E t\right)\cos\left(\varphi\right)\right)$ is in phase and the term $\left(M \sin\left(\omega_E t\right)\sin\left(\varphi\right)\right)$ is out of phase with intensity-modulated fluorescence emission. As a result, $M \cos\left(\omega_E t - \varphi\right)$ can be plotted as a polar coordinate on a Cartesian [x,y] plane. The amplitude of the vector formed by the polar coordinate is equal to the magnitude of the pre-factors on the in-phase and out-of-phase components of $M \cos\left(\omega_E t - \varphi\right)$

$$x = M \cos(\varphi) \tag{25}$$

$$y = M\sin(\varphi) \tag{26}$$

In a similar manner, any term from the summation described in equation (23) can be expressed with the same trigonometric identity discussed previously,

$$\alpha_i M_i \cos(\omega_E t - \varphi_i) = \alpha_i M_i (\cos(\omega_E t)\cos(\varphi_i) + \sin(\omega_E t)\sin(\varphi_i)) \tag{27}$$

Therefore, a polar coordinate can be written for each of the constituent lifetimes in a multi-component sample. However, the polar coordinate that is measured for a sample with a multi-component lifetime contains contributions from the polar coordinate of each constituent lifetime. In this case, the resulting vector describing a sample with a multi-component lifetime is the sum of the polar coordinates from each component lifetime weighted by that component's contribution to the steady-state intensity (a_i).

$$x = \sum_i a_i M_i \cos(\varphi_i) \tag{28}$$

$$y = \sum_i a_i M_i \sin(\varphi_i) \tag{29}$$

In the space of these transformations, any sample characterized by a single lifetime will reside on a semi-circle centered at $(0.5,0)$ with a radius of (0.5). Any polar coordinate of a sample describing a multi-component lifetime will be projected inside the semi-circle.

The polar coordinate calculated from (M) and (φ) uniquely characterizes any fluorescent sample from those with a single component lifetime to those described by complicated distributions of lifetimes. Hence, changes between different samples or among different fluorescent populations in the sample can be visualized simply by monitoring changes in polar coordinate. Without the need for iterative fitting or intensive computations, calculations of distance on the polar plot can also be used to quantitatively calculate both intensity and species fractions of contributing fluorescent components.

The graphical ease of the polar plot is demonstrated in Figure 1.3, where the polar coordinate $\left(\vec{R}\right)$ of sample containing a mixture of two fluorophores with single component lifetimes is shown (Fig. 1.3A). The polar coordinates of the two constituent fluorophores are $\left(\vec{R}_i\right)$ and $\left(\vec{R}_j\right)$ (Fig. 1.3B). The locations of the polar coordinates representing all linear combinations of fluorescing components (i) and (j) is projected as a dotted line between the coordinates of $\left(\vec{R}_i\right)$ and $\left(\vec{R}_j\right)$. The polar coordinate $\left(\vec{R}\right)$ is a weighted sum of $\left(\vec{R}_i\right)$ and $\left(\vec{R}_j\right)$ and therefore, the relative distance between $\left(\vec{R}\right)$ and $\left(\vec{R}_i\right)$ or $\left(\vec{R}_j\right)$ along the dotted line can be used to determine the corresponding intensity fractions. Experimentally, the modulation frequency must be selected carefully to sufficiently resolve and distinguish the variable contributions of fluorophores with different lifetimes

The application of polar plot to study the lifetimes of fluorescent molecules (fluorescent relaxations) began in the early 1980s [44]. At that time, measuring lifetimes with large sets of repetitive frequencies was beginning to be used in order to examine the contribution of multiple distinct decay components in a fluorescent sample. The polar plot was described as a means to verify the relationship between the decay constant derived from the amplitude of oscillation and phase delay for samples with multi-component decays. As measuring lifetimes in images became available, the computational ease of the polar plot shortened data acquisition times and made the analysis more widely accessible to people in a variety of research themes. In parallel, three labs introduced the polar plot for such applications naming it the AB plot [53], polar plot [55] and phasor plot [54]. Currently, this graphical representation of fluorescence lifetimes is standard in most of the software packages for the acquisition and analysis of lifetime measurements.

Phase Suppression

As discussed previously, when detecting lifetimes by homodyning every fluorescent sample is represented in the detector as a cosine curve constructed over the set of phases injected into the detector. When multiple independent samples containing different effective lifetimes (and therefore phase delays) are measured with homodyne detection, the result is a set of cosine curves with distinct phase delays. Throughout this research, the temporal resolution of lifetime imaging by homodyning was not optimal for imaging dynamic processes taking place in live cells. In fact, our lifetime imaging system requires twenty four individual images in order to generate a lifetime image in the frequency domain.

However, a technique called phase suppression which requires only two exposures of the sample collected a carefully chosen set of detector phases (φ_G) can improve the temporal resolution of a lifetime imaging system. By subtracting two intensity images collected while homodyning, the intensity of a specific fluorescent species in an image can be suppressed while ideally retaining the intensity of the other fluorophores with different phase delays in the images [3-5, 17-20, 57]. In other words, the results from phase suppression maps the location of different fluorescent species in an image based solely on the phase delay. For example, consider a fluorescent species (i) having a characteristic phase delay (φ_i) and separately, a fluorescent species (j) with another phase delay (φ_j) as shown in Figure 1.4. Two intensity images (phase images) taken at two different detector phases can be collected describing species (i) such that there is no intensity remaining in the resulting difference image when they are subtracted (images highlighted in yellow in Fig. 1.4A). These two images are then considered 180^o out of phase. Since species (j) has a different phase delay than species (i), the subtraction of two phase images describing species (j) collected at the same two detector phases used to suppress the intensity from species (i) will result in a difference image with a non-zero intensity (images highlighted in yellow in Fig. 1.4B). If both species (i) and species (j) were contained in a single sample being imaged, the subtraction of the two phase images taken at the detector phases highlighted in Figure 1.4 will both eliminate all intensity from species (i) in the resulting difference image. Intensity from species (j) however, will be retained in the difference image.

Phase suppression is advantageous for live cell imaging because the resulting difference images can distinguish different fluorescent species in an image with high contrast while requiring only two exposures of the sample. At the same time, phase suppression can be a physically relevant means to characterize fluorescent species in images because it uses the phase delay as the basis of the pixel classification. If each of the individual fluorescent species in the image have unique phase delays, phase suppression can be a very rapid and quantitative means to track different fluorophores in a given sample.

Instrument for Fluorescence Lifetime Imaging

The lifetime imaging system used throughout this thesis is described schematically in Figure 1.5 [58]. The intensity from light emitted by a variety of continuous lasers is initially modulated by a Pockels Cell [59]. This intensity modulated light is made diffuse by a beam expander prior to being incident on the microscopes dichroic mirror. The microscope itself, operates in full-field and contains several objectives that can image samples with different magnifications and numerical apertures (for changing spatial resolution). The photons emitted by the sample are then converted into photo-electrons by an image intensifier located at the output port of the microscope. The voltage applied across the cathode of the image intensifier is repetitively modulated in order to detect lifetimes by homodyning. A digital phase shifter continuously changes the phase of the signal that is repetitively modulating the voltage on the cathode. That phase shifter takes input directly from a waveform generator. The same waveform generator also produces the signal necessary to modulate the intensity of the excitation light. In this configuration, both the intensity modulation of the exciting light and the

modulation of the cathode's (intensifier's) are synchronized throughout the experiment. A multi-channel plate (MCP) then amplifies the photo-electrons produced by the cathode. In this amplification stage, a significant level of noise is introduced into the image. Prior to being incident on the CCD camera, the photo-electrons ejected from the MCP are converted back in photons by means of a phosphor screen located in the intensifier. On this system, images are acquired between the eight phase images to correct for variations in the intensity of the excitation source. As a result twenty four individual images are acquired to make one lifetime image on this system.

Historical Development of Frequency-Domain FLIM Systems

The development of lifetime imaging in the frequency domain has been motivated by the need to probe the complex environments of living systems such as cells and tissues. The earliest FLIM system reported in 1959 determined effective lifetimes in the frequency domain by comparing the phase delay of the intensity-modulated transmitted light to that of the sample's emitted fluorescence [60]. Without frequency mixing, specimens, including suspensions of stained tumor cells, were imaged at specific locations on a microscope-based imaging system. Interest in measuring the lifetimes of fluorophores in live cells continued throughout the 1970s with several instruments reported that detected lifetimes in images in the time domain [61-63]. In 1986, effective lifetimes were also recorded in the frequency domain at single points within images by taking the Fourier Transform of data collected by photon counting [64]. This system by Murray et. al. was one of the earliest descriptions of short pulses of light being used as an excitation source for FLIM in the frequency domain. Later improvements in detectors

led to two-dimensional lifetime imaging in 1989 with the incorporation of an image dissecting tube with heterodyning in the detection system [65].

In the early 1990s, FLIM systems in the frequency domain sampled more of the illuminated field offered by conventional microscopes. In 1991, a system was designed where the focused output of a pulsed laser could be moved across the field of view with a beam steering device [66]. Although not confocal, this system applied cross-correlation detection to determine the phase delay and modulation ratio of the sample at the locations where the focused laser was exciting the sample. Full-field FLIM systems were later reported in 1991 by Lakowicz et al. [4] and again in 1993 by Gadella et al. [3] Both systems detected the intensity-modulated emission of a microscope-based sample from every pixel simultaneously by homodyning using a gain-modulated intensifier and CCD camera.

Improvements in the available spatial resolution of frequency-domain FLIM systems have also been made throughout the 1990s and into the 2000s. Single photon [67, 68] and two photon [69, 70] scanning confocal techniques have made accurate optical sectioning and 3-dimensional imaging possible with frequency-domain FLIM. Full-field FLIM systems operating in the frequency domain have been recently equipped with spinning disk attachments in order to perform high speed confocal imaging [71, 72]. At this time, a variety of frequency-domain FLIM systems are commercially available and span many of the modalities of the previously developed systems. Alternatively, any of the FLIM systems that measure lifetimes in the time domain can be converted into the frequency domain by simply taking the Fourier Transform of the decay. However, care must be taken to insure that the discrete binning in time during the acquisition of the

fluorescence decay does not result in substantial artifacts in the phase delay and modulation ratio that is eventually computed [73].

Common Artifacts Encountered with Lifetime Imaging

Background Removal

Unwanted fluorescence (background) is common when imaging live cells with full-field microscopy systems. Examples include background from media in the case of live cell imaging, scattered light from the excitation source reaching the detector, fluorescence from mounting media in fixed samples and also the auto-fluorescence from organic compounds in biological samples. Un-modulated background from low levels of dark current can almost never be avoided.

When measuring lifetimes in the frequency domain, the polar plot graphically relates the relative contribution in intensity of different fluorophores and is therefore, very useful for identifying unwanted light or extraneous fluorescence. In most cases, these sources of background have themselves a polar coordinate indicative of their time-dependent fluorescence. However, complications arise when the polar coordinate of the sample or fluorophore of interest is not known (or could be changing) and therefore, the effects of background can't be accurately determined with vector addition. In the case of live cell imaging with full-field microscopes for example, the contribution of background will vary at different positions along the cell. When cells attached to surface, the cell body is stretched making the edges of the cell thinner than the central portions of the cell. Hence, more background light from the media will enter the objective along the edge of the cell than in the center. Precisely knowing the geometry of every cell imaged to

account for this sort of variable background is not feasible or accurate. In the literature, simple techniques to remove background such as averaging the intensity from a region of interest in a section of the image that does not include the cell and subtracting that value from all pixels in the image, invariably will leave artifacts in the image [74].

Likewise, any measured phase delay and modulation ratio (even that from a homogenous sample such as a solution) has an associated uncertainty stemming from the noise in the detection system. The signal acquired from any detector counting photons contains Possion noise simply as a result of the stochastic nature of fluorescence emission. On the polar plot for example, a measurement taken on a homogenous sample such as a solution of fluorescent dye, appears as a symmetric distribution centered at the actual lifetime of the sample [58]. As the noise in the signal increases, the width of the distribution progressively increases. Therefore, on a pixel-wise basis, vector addition cannot be performed accurately to remove background either.

Recently, a technique has been introduced to remove background that incorporates the analysis of spatial frequencies using wavelets to distinguish specific morphological features in images [72, 75]. Analyzing spatial frequencies solves the problem of not knowing precisely the extent of background in the system and addresses the complication of having noise present in the detected signal.

Wavelets are sets of basis function that can decompose both images and signals for the purposes of image compression, noise removal and generally to analyze spatial frequencies. Wavelets can be thought of in a manner similar to that of the sinusoidal functions applied in Fourier analysis. However, the problem with Fourier analysis is that it only yields the frequencies present in the signal without any spatial information. If, for

example, small portions (windows) of the signal are selected for Fourier analysis, problems exist because the frequency resolution will degrade as you select smaller windows along the signal to analyze.

Wavelets are sets of basis functions that typically resemble oscillatory and very localized waves that can be stretched (scaled) and translated throughout an image [76-78]. Each scaled (stretched) version of the wavelet can highlight a different set of spatial frequencies in the images. Therefore, the purpose of applying the wavelet basis functions to decompose a signal or image is to determine information about spatial frequencies (referred to as scales) at every position in the image. The Continuous Wavelet Transform (CWT), (as partially described above) that continuously shifts a wavelet basis function at various scales throughout an image is computationally intensive and can lead to redundant calculations. The Discrete Wavelet Transform (DWT) by contrast, provides an equivalently accurate but less computationally expensive means to decompose a signal by sampling the scales and positions on which the wavelet basis functions act discretely by powers of two.

The ongoing research examining the MT1-MMP biosensor applies the DWT to images collected on the FLIM instrument for the purposes of background removal. In the DWT, the scaling of the wavelet in discrete steps creates a series of bandpass filters through which the image can be analyzed. Primarily, the presence of the low scales (high frequencies) in the image is determined by the scaling function in the DWT [77, 78]. When applied to an image, the DWT converts the image using successive iterations through a set of low pass and bandpass filters, into a series of approximations and detail coefficient matrices.

The removal of background from the intensity images collected on the FLIM instrument will incorporate the approximations of the image that are given by the DWT into the multi-resolution analysis described by Mallat [75]. Each approximation of the image contains the bandpass of frequencies inherent to the analyzing wavelet that generated the approximation at the particular scale (resolution). If two approximations are taken at distinct scales (resolutions) and subtracted, the resulting difference image contains only the spatial frequencies in the region of frequencies between the two approximations. Although distinct from the process of purely re-constructing a signal from the entire set of approximation and detail coefficients derived from the DWT de-composition, multi-resolution analysis can specifically distinguish in the case of live samples, high frequency noise generated from background factors from meaningful low frequency (high scale) morphological features. As shown in the later chapters, multi-resolution analysis can substantially eliminate background when applied to FLIM [72]. Therefore, the optimization of removing background from the intensity images with the DWT and multi-resolution analysis requires both the selection of the appropriate wavelet and the scales to be studied.

Photobleaching

In this section, photobleaching refers to a loss of signal that occurs during the collection of a lifetime image. For example, a loss of signal taking place during the acquisition of the eight phase images collected while detecting lifetimes by homodyning would correspond to photobleaching in this context. A progressive loss of signal is apparent when the intensities taken at each detector phase are plotted against their corresponding angle (φ_G). However, the trajectories on the polar plot indicative of this

sort of photobleaching can vary significantly depending the phase of the exciting light's intensity modulation (φ_E) (simulation described in Figure 1.6). In some cases, the presence of photobleaching could be easily mistaken for simple multi-component lifetimes. As will be discussed in the next chapter, a polar coordinate outside of the universal semi-circle is not in all cases the result of photobleaching and may even be the result of FRET. As such, the most effective method to detect photobleaching is to examine the attenuation of the individual phase images collected during the experiment combined with some sort of before-hand knowledge about the lifetimes of the sample being studied.

Figures

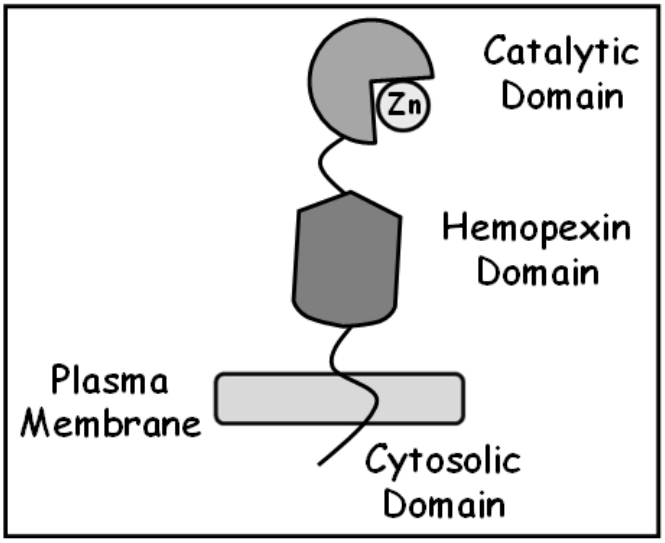

Figure 1.1: MT1-MMP Enzyme: The MT1-MMP enzyme attaches to the proteins located throughout the ECM using the central (hemopexin) domain. The proteolysis of ECM proteins takes place in the catalytic domain. The chemical GM6001 used in the experimental sections of the thesis forms a complex with the zinc in the active site to inhibit the activity of MT1-MMP. The cytosolic domain of MT1-MMP mediates communication with internal proteins and enzymes such as Src Kinase. Based on [29].

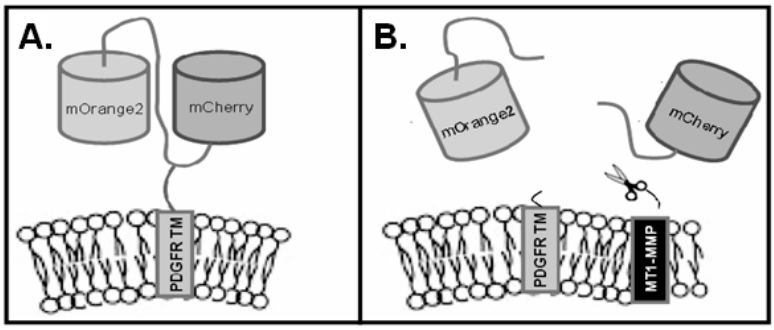

Figure 1.2: MT1-MMP Biosensor (A) The biosensor is initially tethered to the cell's membrane with trans-membrane (TM) domain of the platelet-derived growth factor (PDGF). Both the donor fluorescent protein (mOrange2) and the acceptor (mCherry) are in close proximity such that emission from the mCherry can take place when the mOrange2 is excited. (B) When an active MT1-MMP enzyme cleaves the substrate of the biosensor, the mOrange2 and mCherry are permanently separated. No emission from the mCherry can be observed when mOrange2 is excited. Modified from [2].

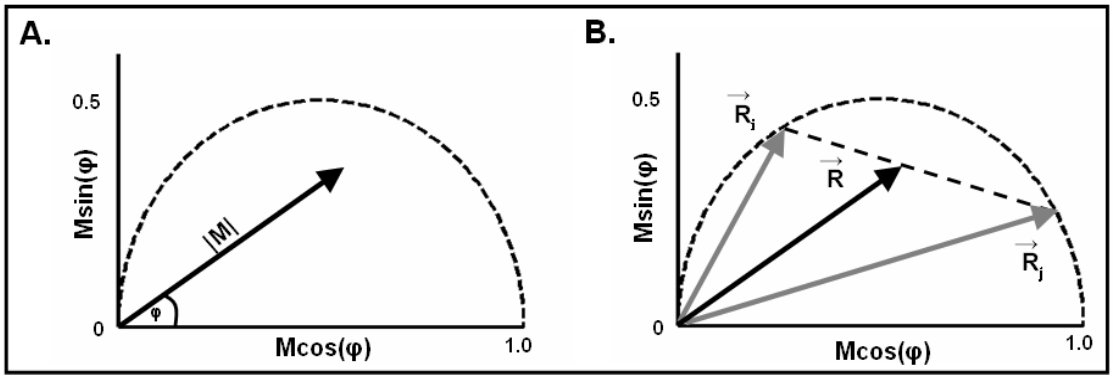

Figure 1.3: Basics of the Polar Plot. (A) The polar coordinate of any fluorophore can be equivalently described as a vector with a length equal to the modulation ratio making an angle relative to the x-axis equal to the phase delay. (B) Two different fluorophores defined by the vectors $\left(\vec{R}_i\right)$ and $\left(\vec{R}_j\right)$ contribute intensity to the measured polar coordinate $\left(\vec{R}\right)$. All possible measured combinations of the two fluorophores (i) and (j) lie on the dotted line projected within the semi-circle.

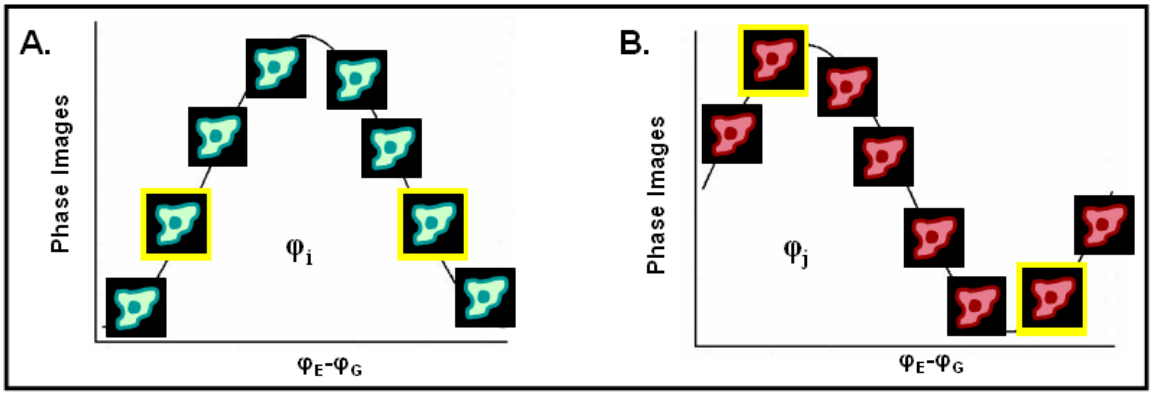

Figure 1.4: Schematic of Phase Suppression: (A) A set of images gathered using homodyne detection is shown with a given phase delay (φ_i) characteristic of the sample. When the two intensity images which are highlighted in yellow are subtracted, there will be no intensity remaining in the resulting difference image from the fluorescent species with phase delay (φ_i). (B) A separate set of images collected with homodyne detection is presented. The fluorescent species depicted in these images have a phase delay (φ_j) such that $(\varphi_i) \neq (\varphi_j)$. As a result, if two images are selected at the exact same detector phases that correspond to the highlighted images selected in (A), the subtraction of these images will result in a nonzero intensity in the final difference image.

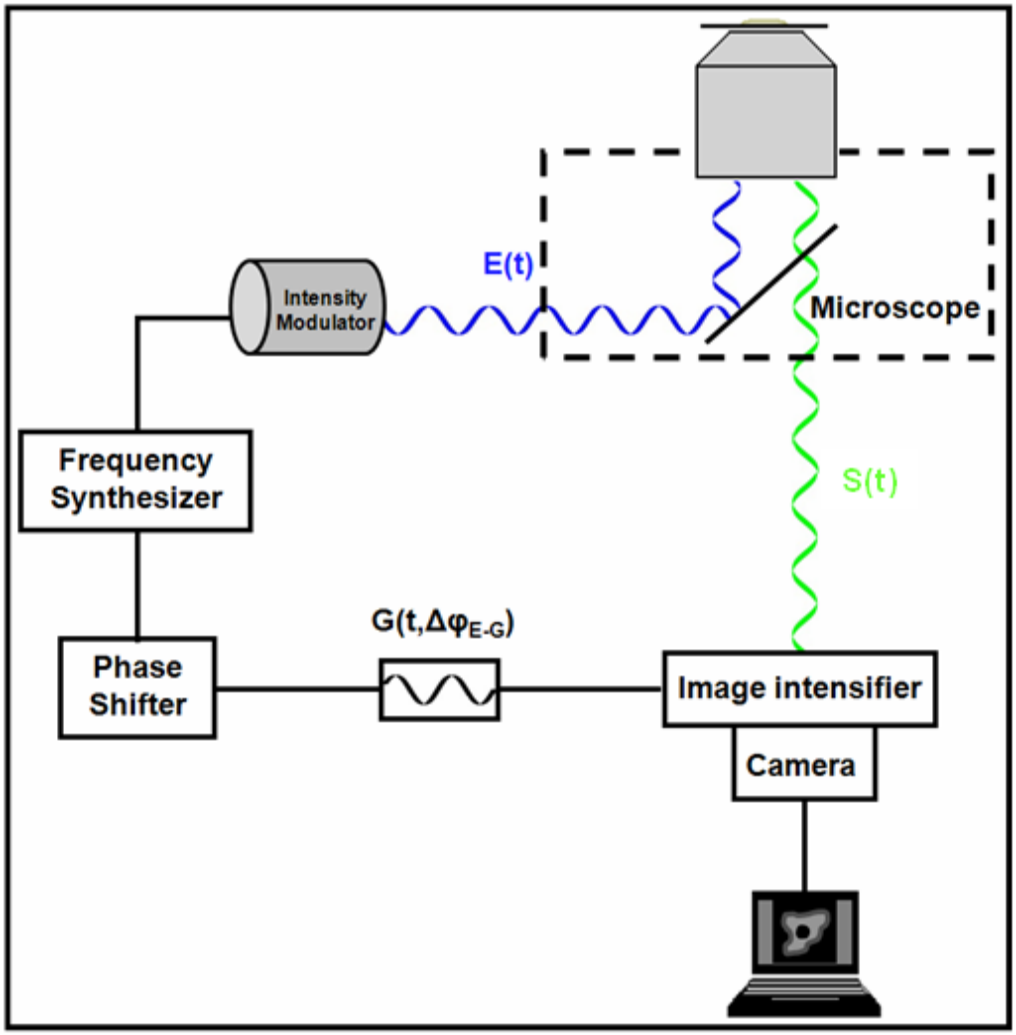

Figure 1.5: The Fluorescence Lifetime Imaging System: Light from a continuous laser is intensity-modulated by a Pockels Cell (labeled intensity modulator). The fluorescence from the sample is also intensity-modulated. Frequency mixing is accomplished by injected a radio frequency (oscillating voltage) gating the voltage on the cathode of the detector (an intensified CCD camera). As the phase of the signal injected into the cathode is incrementally shifted over a full period of cosine, images are collected at each phase shift. From these images, the modulation ratio and phase delay can be computed on a pixel-wise basis.

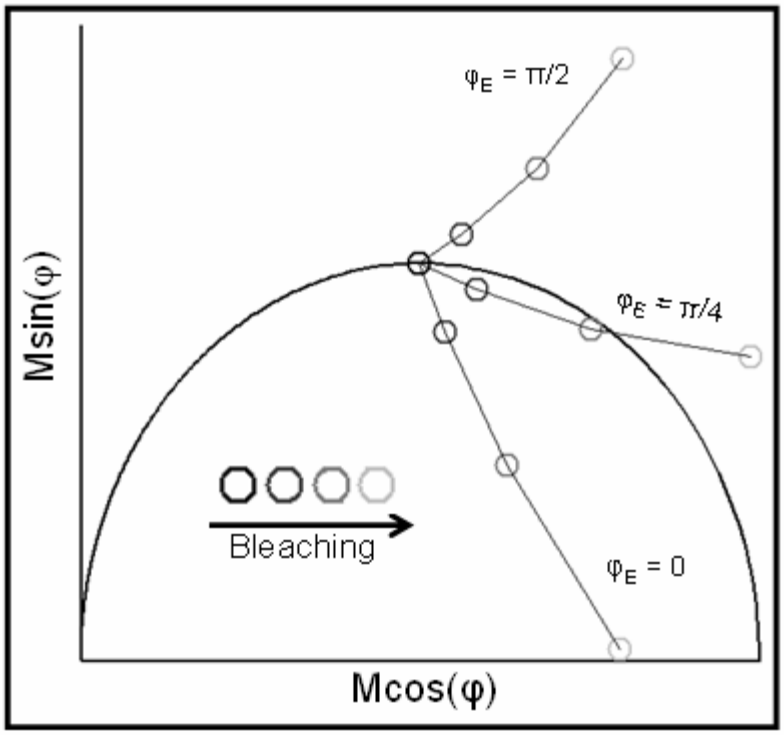

Figure 1.6: Photobleaching from the perspective of the polar plot: The detection of a sample with a lifetime of 4ns was simulated with a modulation frequency of 40MHz. An incremental dampening of intensity was introduced into the phase images collected by homodyning (gray circles). In this simulation the phase of the exciting light's intensity modulation (φ_E) was sampled at 0, $(\pi/4)$ and $(\pi/2)$.

References

1. Ouyang, M., et al., *Simultaneous visualization of protumorigenic Src and MT1-MMP activities with fluorescence resonance energy transfer.* Cancer Res. **70**(6): p. 2204-12.
2. Ouyang, M., et al., *Visualization of polarized membrane type 1 matrix metalloproteinase activity in live cells by fluorescence resonance energy transfer imaging.* J Biol Chem, 2008. **283**(25): p. 17740-8.
3. Gadella, T.W., Jr., T.M. Jovin, and R.M. Clegg, *Fluorescence lifetime imaging microscopy (FLIM): Spatial resolution of microstructures on the nanosecond time scale.* Biophysical Chemistry, 1993. **48**: p. 221-239.
4. Lakowicz, J.R. and K.W. Berndt, *Lifetime-selective fluorescence imaging using an rf phase-sensitive camera.* Reviews of Scientific Instrumentation, 1991. **62**(7): p. 1727-1734.
5. Schneider, P. and R.M. Clegg, *Rapid acquisition, analysis and display of fluorescence lifetime-resolved images for real-time applications.* Reviews of Scientific Instrumentation, 1997. **68**(11): p. 4107-4119.
6. Adams, S.R., et al., *Fluorescence ratio imaging of cyclic AMP in single cells.* Nature, 1991. **349**(6311): p. 694-7.
7. Jovin, T.a.A.-J., Donna, *FRET Microscopy: Digital Imaging of Fluorescence Resonance Energy Transfer. Application in Cell Biology*, in *Cell Structure and Function by Microspectrofluorometry*, E.a.H. Kohen, Joseph, Editor. 1989, Academic Press: San Diego, California. p. 99-115.

8. Szollosi, J., et al., *Flow cytometric resonance energy transfer measurements support the association of a 95-kDa peptide termed T27 with the 55-kDa Tac peptide.* Proc Natl Acad Sci U S A, 1987. **84**(20): p. 7246-50.

9. Szollosi, J., et al., *Fluorescence energy transfer measurements on cell surfaces: a critical comparison of steady-state fluorimetric and flow cytometric methods.* Cytometry, 1984. **5**(2): p. 210-6.

10. Tsien, R.Y., B.J. Bacskai, and S.R. Adams, *FRET for studying intracellular signalling.* Trends Cell Biol, 1993. **3**(7): p. 242-5.

11. Birks, J., *Photophysics of Aromatic Molecules*. 1970, Wiley-Interscience: New York.

12. Lakowicz, J., *Principles of Fluorescence Spectroscopy*. 2006, New York, NY: Springer. 954.

13. Noomnarm, U. and R.M. Clegg, *Fluorescence lifetimes: fundamentals and interpretations.* Photosynth Res, 2009. **101**(2-3): p. 181-94.

14. Valeur, B., *Molecular Fluorescence: Principles and Applications*. 2002, Weinheim, Germany: WILEY-VCH.

15. Clegg, R.M., *Fluorescence Lifetime-Resolved Imaging Microscopy (FLIM)*. Biomedical Optical Instrumentation and Laser-Assisted Biotechnology: Proceedings of the NATO Advanced Study Institute, Etice, Italy November 10-22, 1995, ed. A.M. Verga Scheggi. 1996, Dordrecht, Netherlands: Kluwer Academic Publishers. 143-156.

16. Eichorst, J.P., et al., *Phase differential enhancement of FLIM to distinguish FRET components of a biosensor for monitoring molecular activity of Membrane Type 1 Matrix Metalloproteinase in live cells.* J Fluoresc. **21**(4): p. 1763-77.

17. Lakowicz, J.R. and H. Cherek, *Phase-sensitive fluorescence spectroscopy: a new method to resolve fluorescence lifetimes or emission spectra of components in a mixture of fluorophores.* J Biochem Biophys Methods, 1981. **5**(1): p. 19-35.

18. Lakowicz, J.R., et al., *Fluorescence lifetime imaging of free and protein-bound NADH.* Proc Natl Acad Sci U S A, 1992. **89**(4): p. 1271-5.

19. Veselova, T.V., A.S. Cherkasov, and V.I. Shirokov, *Fluorometric method for individual recording of spectra in systems containing two types of luminiscent centers.* Optical Spectroscopy, 1970. **29**: p. 617-618.

20. Veselova, T.V. and V.I. Shirokov, *A spectral fluorometric study of the luminescence of exiplexes of 3-amino-AT-methylphthalimide with acetone, pyridine, and dimethylformamide.* Iz. Akad. Nauk SSSR Ser. Fiz, 1972. **36**: p. 1024.

21. Deryugina, E.I. and J.P. Quigley, *Matrix metalloproteinases and tumor metastasis.* Cancer Metastasis Rev, 2006. **25**(1): p. 9-34.

22. Klein, T. and R. Bischoff, *Physiology and pathophysiology of matrix metalloproteases.* Amino Acids, 2011. **41**: p. 271-290.

23. Seiki, M., *Membrane-type 1 matrix metalloproteinase: a key enzyme for tumor invasion.* Cancer Lett, 2003. **194**(1): p. 1-11.

24. Seiki, M., et al., *Membrane-type 1 matrix metalloproteinase and cell migration.* Biochem Soc Symp, 2003(70): p. 253-62.

25. Wolf, K. and P. Friedl, *Mapping proteolytic cancer cell-extracellular matrix interfaces.* Clin Exp Metastasis, 2009. **26**(4): p. 289-98.

26. Nakada, M., et al., *Expression and tissue localization of membrane-type 1, 2, and 3 matrix metalloproteinases in human astrocytic tumors.* Am J Pathol, 1999. **154**(2): p. 417-28.

27. Zhai, Y., et al., *Expression of membrane type 1 matrix metalloproteinase is associated with cervical carcinoma progression and invasion.* Cancer Res, 2005. **65**(15): p. 6543-50.

28. Hofmann, U.B., et al., *Expression of matrix metalloproteinases in the microenvironment of spontaneous and experimental melanoma metastases reflects the requirements for tumor formation.* Cancer Res, 2003. **63**(23): p. 8221-5.

29. Gingras, D. and R. Beliveau, *Emerging concepts in the regulation of membrane-type 1 matrix metalloproteinase activity.* Biochim Biophys Acta. **1803**(1): p. 142-50.

30. Nyalendo, C., et al., *Src-dependent phosphorylation of membrane type I matrix metalloproteinase on cytoplasmic tyrosine 573: role in endothelial and tumor cell migration.* J Biol Chem, 2007. **282**(21): p. 15690-9.

31. Uekita, T., et al., *Cytoplasmic tail-dependent internalization of membrane-type 1 matrix metalloproteinase is important for its invasion-promoting activity.* J Cell Biol, 2001. **155**(7): p. 1345-56.

32. Kajita, M., et al., *Membrane-type 1 matrix metalloproteinase cleaves CD44 and promotes cell migration.* J Cell Biol, 2001. **153**(5): p. 893-904.

33. Endo, K., et al., *Cleavage of syndecan-1 by membrane type matrix metalloproteinase-1 stimulates cell migration.* J Biol Chem, 2003. **278**(42): p. 40764-70.

34. Wolf, K., et al., *Multi-step pericellular proteolysis controls the transition from individual to collective cancer cell invasion.* Nat Cell Biol, 2007. **9**(8): p. 893-904.

35. Cukierman, E., et al., *Taking cell-matrix adhesions to the third dimension.* Science, 2001. **294**(5547): p. 1708-12.

36. Packard, B.Z., et al., *Direct visualization of protease activity on cells migrating in three-dimensions.* Matrix Biol, 2009. **28**(1): p. 3-10.

37. Yamada, K.M. and E. Cukierman, *Modeling tissue morphogenesis and cancer in 3D.* Cell, 2007. **130**(4): p. 601-10.

38. Rasheed, S., et al., *Characterization of a newly derived human sarcoma cell line (HT-1080).* Cancer, 1974. **33**: p. 1027-1033.

39. Tregidgo, C., J.A. Levitt, and K. Suhling, *Effect of refractive index on the fluorescence lifetime of green fluorescent protein.* J Biomed Opt, 2008. **13**(3): p. 031218.

40. Boens, N., et al., *Fluorescence lifetime standards for time and frequency domain fluorescence spectroscopy.* Anal Chem, 2007. **79**(5): p. 2137-49.

41. Duncan, R.R., et al., *Multi-dimensional time-correlated single photon counting (TCSPC) fluorescence lifetime imaging microscopy (FLIM) to detect FRET in cells.* J Microsc, 2004. **215**(Pt 1): p. 1-12.

42. Millington, M., et al., *High-precision FLIM-FRET in fixed and living cells reveals heterogeneity in a simple CFP-YFP fusion protein.* Biophys Chem, 2007. **127**(3): p. 155-64.

43. Tramier, M., et al., *Picosecond-hetero-FRET microscopy to probe protein-protein interactions in live cells.* Biophys J, 2002. **83**(6): p. 3570-7.

44. Jameson, D.M., E. Gratton, and R.D. Hall, *The Measurement and Analysis of Hetergeneous Emissions by Multifrrequency Phase and Modulation Fluorometry.* Applied Spectroscopy Reviews, 1984. **20**(1): p. 55-106.

45. Gratton, E. and M. Limkeman, *A Continuously Variable Frequency Cross-Correlation Phase Fluorometer with Picosecond Resolution.* Biophys J, 1983. **44**: p. 315-324.

46. Gratton, E., D.M. Jameson, and R.D. Hall, *Multifrequency phase and modulation fluorometry.* Annu Rev Biophys Bioeng, 1984. **13**: p. 105-24.

47. Brigham, E.O., *The Fast Fourier Transform and Its Application*. 1988, Englewood Cliffs, New Jersey: Prentice Hall.

48. Bracewell, R.A., *The Fourier Transformation and its Applications*. 1978, Hamburg: McGraw-Hill Kogakusha, Ltd.

49. Mitchell, A.C., et al., *Direct Modulation of the effective sensitivity of a CCD detector: a new approach to time-resolved fluorescence imaging.* Journal of Microscopy, 2002. **206**(3): p. 225-232.

50. Spencer, R.D. and G. Weber, *Measurements of subnanosecond fluorescence lifetimes with a cross-correlation phase fluorometer.* Annals of the New York Academy of Sciences, 1969. **158**: p. 361-376.

51. Hamming, R.W., *Numerical methods for scientists and engineers*. 2d ed. 1973, New York,: McGraw-Hill. ix, 721 p.

52. Colyer, R.A., C. Lee, and E. Gratton, *A novel fluorescence lifetime imaging system that optimizes photon efficiency.* Microsc Res Tech, 2008. **71**(3): p. 201-13.

53. Hanley, Q.S. and A.H. Clayton, *AB-plot assisted determination of fluorophore mixtures in a fluorescence lifetime microscope using spectra or quenchers.* J Microsc, 2005. **218**(Pt 1): p. 62-7.

54. Digman, M.A., et al., *The phasor approach to fluorescence lifetime imaging analysis.* Biophys J, 2008. **94**(2): p. L14-6.

55. Redford, G.I. and R.M. Clegg, *Polar plot representation for frequency-domain analysis of fluorescence lifetimes.* J Fluoresc, 2005. **15**(5): p. 805-15.

56. Chen, Y.-C., et al., *General Concerns of FLIM Data Representation and Analysis: Frequency-Domain Model-Free Analysis*. FLIM Microscopy in Biology and Medicine, ed. A. Periasamy and R.M. Clegg. 2010, New York: Chapman & Hall/CRC. 291-335.

57. Lakowicz, J.R. and H. Cherek, *Resolution of Heterogeneous Fluorescence by Phase-sensitive Fluorescence Spectroscopy.* Biophys J, 1982. **37**(1): p. 148-150.

58. Spring, B.Q. and R.M. Clegg, *Image analysis for denoising full-field frequency-domain fluorescence lifetime images.* J Microsc, 2009. **235**(2): p. 221-37.

59. Kaminow, I.P. and E.H. Turner, *Electrooptic Light Modulators.* Proceedings of the IEEE, 1966. **54**(10): p. 1374-1390.

60. Venetta, B., *Microscope Phase Fluorometer for Determining the Fluorescence Lifetime of Fluorochromes.* The Review of Scientific Instruments, 1959. **30**(6): p. 450-457.

61. Arndt-Jovin, D.J., et al., *Fluorescence decay analysis in solution and in a microscope of DNA and chromosomes stained with quinacrine.* J Histochem Cytochem, 1979. **27**(1): p. 87-95.

62. Loeser, C.N., et al., *Measurement of Fluorescence Decay Time in Living Cells.* Experimental Cell Research, 1972. **72**(1972): p. 480-484.

63. Loeser, C.N. and E. Clark, *Intracellular Fluorescence Decay Time of Anilinonaphthalene Sulfonate.* Experimental Cell Research, 1972. **72**: p. 485-488.

64. Murray, J.G., et al., *A single-photon-counting Fourier transform microfluorometer.* J. Phys. E: Sci. Instrum., 1986. **19**: p. 349-355.

65. Wang, X.F., T. Uchida, and S. Minami, *A Fluorescence Lifetime Distribution Measurement System Based on Phase-Resolved Detection Using an Image Dissector Tube.* Applied Spectroscopy, 1989. **43**(5): p. 840-845.

66. Verkman, A.S., M. Armijo, and K. Fushimi, *Construction and evaluation of a frequency-domain epifluorescence microscope for lifetime and anisotropy decay measurements in subcellular domains.* Biophys Chem, 1991. **40**(1): p. 117-25.

67. Buurman, E.P., et al., *Fluorescence lifetime imaging using a confocal laser scanning microscope.* Scanning, 1992. **14**: p. 155-159.

68. Morgan, C.G., A.C. Mitchell, and J.G. Murray, *Prospects for confocal imaging based on nanosecond fluorescence decay time.* Journal of Microscopy, 1992. **165**(1): p. 49-60.

69. So, P.T.C., et al., *Time-resolved fluorescence microscopy using two-photon excitation.* Bioimaging, 1995. **3**(2): p. 49-63.

70. Piston, D.W., D.R. Sandison, and W.W. Webb, *Time-resolved fluorescence imaging and background rejection by two-photon excitation in laser scanning microscopy.* Proc. SPIE, 1992. **1640**: p. 379-389.

71. van Munster, E.B., et al., *Combination of a spinning disc confocal unit with frequency-domain fluorescence lifetime imaging microscopy.* Cytometry A, 2007. **71**(4): p. 207-14.

72. Buranachai, C., et al., *Rapid frequency-domain FLIM spinning disk confocal microscope: lifetime resolution, image improvement and wavelet analysis.* J Fluoresc, 2008. **18**(5): p. 929-42.

73. Leray, A., et al., *Generalization of the polar representation in time domain fluorescence lifetime imaging microscopy for biological applications: practical implementation.* J Microsc. **248**(1): p. 66-76.

74. Palmer, A.E. and R.Y. Tsien, *Measuring calcium signaling using genetically targetable fluorescent indicators.* Nat Protoc, 2006. **1**(3): p. 1057-65.

75. Mallat, S.G., *A Theory fo Multiresolution Signal Decomposition: The Wavelet Representation.* IEEE Transactions on Pattern Analysis and Machine Intelligence, 1989. **11**(7): p. 674-692.

76. Farge, M., *Wavelet Transforms and Their Applications to Turbulence.* Annual Reviews of Fluid Mechanics, 1992. **24**: p. 395-457.

77. Hubbard, B.B., *The World According to Wavelets The Story of a Mathematical Technique in the Making*. Second ed. 1998, Natick,MA: A K Peters, Ltd.

78. Rao, R.M. and A.S. Bopardikar, *Wavelet Transforms Introduction to Theory and Applications*. 1998, Reading, MA: Addison-Wesley.

Chapter 2

An Apparent Discrepancy in Measurements of FRET with the Cyan Variant of the MT1-MMP Biosensor

Abstract

The project studying the MT1-MMP biosensor in live HT-1080 cells began with the Enhanced Cyan Fluorescent Protein (ECFP) and the Yellow Fluorescent Protein for FRET (YPet) that had been previously applied to examine the biosensor with steady-state fluorescence imaging. When the biosensor was examined in live cells, it was clear that the definite changes in FRET detected by the steady-state methods did not translate into robust changes in the time-dependent fluorescence (lifetimes) measured by lifetime imaging. In fact, there was no difference in lifetime recorded for the ECFP regardless of which configuration of the biosensor was measured (intact or cleaved) in live cells. To make this study even more confusing, a small change in the time-dependent fluorescence of the acceptor (YPet) was observed in the images of live cells taken on the lifetime imaging system when the donor (ECFP) was excited. Despite the significant time spent studying the cell's condition, applying a variety of drug treatments as well as extensive instrumental diagnostics, the observations about the extent of FRET taking place among the various methods used remained consistent. During this time, numerous questions about the sensitivity, relevance and accuracy of each method to detect FRET were continually raised. In this chapter, a critical comparison was carried out to compare the changes detected by various techniques for measuring FRET in order to explain this apparent discrepancy in the measurements. However, when these results were combined with theoretical calculations and models, the data from each method actually and

unanimously indicated that there was a likely high background of non-interacting donor throughout the cells analyzed.

Introduction

FRET is a unique parameter in science because quite a variety of methods and techniques exist simply to measure the same thing, the extent of FRET taking place in systems such as live cells. However, regardless of the technique applied, the extent or amount of FRET taking place in a given system is described by specific and definite physical parameters indicative of a distance-dependent and non-radiative transfer of energy between two oscillators. Hence, the results gathered from different types of measurements of FRET taken on sets of similar systems should reflect the same physical reality with respect to the oscillators, their concentration and their propensity to engage in FRET. Regardless of the type of measurement applied, it is this reality that is relevant to characterize the physical process of FRET taking place and that which ought to be quantified when any data is analyzed. Simply inventing indexes or techniques that conveniently exaggerate the size of changes in measurements of FRET taking place in systems does not side-step or make irrelevant the physical grounding required to interpret measurements of FRET. All measurements of FRET therefore, should be taken, analyzed and presented with attention paid to parameters specific to the physical process of FRET. Otherwise, processes such as convenient indexing or qualitative measurements will inherently be subject to substantial artifacts and uncertainties and will no doubt, lead to false conclusions.

In the community of scientists studying FRET-based biosensors in live cells, steady-state ratiometric techniques have become common because of both the ease at which they can be carried out and the large changes in FRET typically encountered in these measurements. In the simplest application, this ratiometric intensity imaging divides an image acquired from the donor's fluorescent emission and an image generated from the emission of the acceptor while exciting the sample at the donor's excitation wavelength. This ratio is mapped as a pixel-wise index indicating the extent of FRET taking place throughout the image. With this technique, coupling a very dim donor with a bright acceptor on the biosensor is ideal to create dramatic changes in intensity even when small changes FRET are taking place. However, the measured "FRET ratio" is highly dependent on the actual concentration of interacting (FRET) and non-interacting (No-FRET) donors and acceptors in an area of an image. It has been previously cited that false positives and uncertainties in the interpretation of the FRET ratio can be reduced if all observed biosensors are intact (each biosensor (molecule) containing a donor and acceptor) throughout the experiment [1].

Recently, Fluorescence Lifetime Imaging Microscopy (FLIM) has also been increasingly used as a more quantitative means to determine the configuration of biosensors in a given pixel [2-5]. A measured lifetime relates the average amount of time a fluorescent molecule remains in the excited state. When fluorescent molecule is excited and near an acceptor, the excited state will be depleted more rapidly shortening the lifetime. Measured lifetimes are absolute measurements and are particularly useful when characterizing systems containing both interacting and non-interacting donors and acceptors.

Although FLIM is a very direct and intensity-independent means to examine biosensors in images, the dynamic range of the changes in time-dependent fluorescence observed with FLIM are consistently smaller than that observed with steady-state methods such as the FRET ratio specifically when using variants of the cyan and yellow fluorescent proteins. Several papers have indicated that certain variants of the cyan and yellow fluorescent proteins simply are not suitable for FLIM while at the same time these pairs provide definite and robust changes in the FRET ratio when studying intracellular FRET-based biosensors. [6-12]. At this time, however, the reasons for these apparent discrepancies between measurements taken with FLIM and equivalent measurements taken with the FRET ratio have not been completely determined in the literature.

In order to address the apparent discrepancies between different methods for detecting FRET, multiple techniques of measuring FRET in images were compared; steady-state measurement of FRET efficiency, the FRET ratio and measurements taken with FLIM on both the donor and acceptor. In addition to the measurements of FRET, both drug treatments and imaging with the selective excitation of the cyan and yellow fluorescent proteins were used in order to study regions of the cells containing different configurations (intact or cleaved) of the biosensors. Experimentally, changes in the steady-state FRET efficiency and the FRET ratio were consistently observed throughout the various sections of the cells analyzed. However, no change in the time-dependent fluorescence of the donor was detected by FLIM regardless of the region of the cell analyzed or the drug treatment applied. At the same time, some variation in the time-dependent fluorescence of the acceptor was detected when exciting the donor (ECFP) within specific regions of the cells analyzed. The only theoretical model that accounts for

these experimental results implies that there is a high background of non-interacting donors when the ECFP-based biosensor is expressed in live cells.

Materials and Methods

FRET Efficiency: Steady-State

Detecting the FRET Efficiency with Steady-State Measurements

The FRET efficiency (E) relates the amount of energy transfer taking place to the distance between the donor and acceptor fluorophores [13-16]. Dependencies on other parameters such as the quantum yield of the donor, the extinction coefficient of the acceptor, the wavelength range being applied, and the orientation of the donor and acceptor fluorophores are also contained in the equation relating the FRET efficiency to the separation distance between the donor and acceptor. Within a cell expressing the biosensor, only two distances between the donor and acceptor fluorophores exist describing the intact and cleaved biosensor. In any specific region of the cell, there can only linear combinations of these two configurations. Therefore, measurements of the FRET efficiency taken on live cells are not related to the distance between the donor and acceptor (as in the case of single molecules) unless the region of the cell being examined is populated by only one configuration of the biosensor. In the case where there is a combination of intact and cleaved biosensors in a region of an image, the FRET efficiency measured is simply an effective number that can be related to the relative stoichiometry of the biosensors.

As described in the following references and supplemental derivations [17-20], measuring the FRET efficiency in an image in steady-state requires that a series of at

least three images of the cell be acquired. Images of calibrating solutions and cells singly labeled with either the donor or acceptor alone must also be acquired to complete the analysis. The images of the cell of interest are collected first with emission wavelengths describing the donor while exciting the donor $I\left(\lambda_{EX}^{D},\lambda_{EM}^{D}\right)$, followed by an image generated while collecting intensity from primarily the acceptor's wavelengths while exciting the donor $I\left(\lambda_{EX}^{D},\lambda_{EM}^{A}\right)$ and finally an image gathering at acceptor's emission while exciting only the acceptor $I\left(\lambda_{EX}^{A},\lambda_{EM}^{A}\right)$.

The FRET efficiency (E) can be written as follows where (b_1) and (b_2) are bleedthrough corrections and (ξ) is the ratio of the quantum yields of the donor and acceptor.

$$E=\frac{\xi\left(I\left(\lambda_{EX}^{D},\lambda_{EM}^{A}\right)-b_1 I\left(\lambda_{EX}^{D},\lambda_{EM}^{D}\right)-b_2 I\left(\lambda_{EX}^{A},\lambda_{EM}^{A}\right)\right)}{I\left(\lambda_{EX}^{D},\lambda_{EM}^{D}\right)+\xi\left(I\left(\lambda_{EX}^{D},\lambda_{EM}^{A}\right)-b_1 I\left(\lambda_{EX}^{D},\lambda_{EM}^{D}\right)-b_2 I\left(\lambda_{EX}^{A},\lambda_{EM}^{A}\right)\right)} \qquad (1)$$

The above equation is in the precise form that is used to experimentally determine the FRET efficiency throughout an image.

The bleedthrough coefficient (b_1) corrects for the fluorescence emission from the donor that can be detected in the channel (set of emission wavelengths) specific for the acceptor. More specifically, (b_1) is the ratio of the donor's emission collected through the donor's emission channel and separately, through the acceptor's emission channel using a single excitation wavelength. In an analogous way, the coefficient (b_2) accounts for the

fluorescence emission of the acceptor that can be directly excited at the donor's excitation wavelength $\left(\lambda_{EX}^{D}\right)$. This directly excited emission from the acceptor could be misinterpreted as FRET. Experimentally, the acceptor's fluorescence that results from direct excitation at the wavelength $\left(\lambda_{EX}^{D}\right)$ and the intensity of the acceptor's fluorescence that is emitted while being excited at $\left(\lambda_{EX}^{A}\right)$ are measured and a ratio is taken to determine the coefficient $\left(b_2\right)$. Both of these coefficients can be determined experimentally with samples containing only the donor fluorophores and separately containing only the acceptor fluorophores.

The ratio of the quantum yield of the donor $\left(QY_{Don}\right)$ and the quantum yield of the acceptor $\left(QY_{Acc}\right)$ is referred to as $\left(\xi\right)$ and can be determined experimentally using the same excitation and emission wavelengths as applied in the actual microscope-based FRET experiments. The detected fluorescence from solutions containing either only donor (referred to as $\left(I_{Sol}^{DD}\right)$) or only acceptor fluorophores (referred to as $\left(I_{Sol}^{AA}\right)$) are measured separately on the imaging system using the same excitation sources and emission filters as the live cell experiments. The optical density of the donor-only $\left(OD_{Sol}^{DD}\right)$ and acceptor-only $\left(OD_{Sol}^{AA}\right)$ solutions and the optical power of the exciting light then normalize the measured fluorescence intensities to extract the ratio of the quantum yields. The optical power of the excitation sources on the imaging system needs to be measured with a solution of Rhodamine B in ethylene glycol $\left(RhodB_{Sol}\right)$ often referred to as a quantum counter [21]. The definition of $\left(\xi\right)$ from these measured quantities can be written as,

$$\xi = \frac{\frac{I_{Sol}^{DD}}{OD_{Sol}^{DD} * RhodB_{Sol}^{DD}}}{\frac{I_{Sol}^{AA}}{OD_{Sol}^{AA} * RhodB_{Sol}^{AA}}} = \frac{QY_{Don}}{QY_{Acc}} \quad (2)$$

Specifically in the case when two different dichroic mirrors are used, care must be taken to account for differences in the transmission of the two mirrors in the wavelength span being used when determining (ξ).

Several methods have been reported to find (ξ) experimentally including techniques based on photobleaching [22], using tandem constructs of donor and acceptor protein pairs of different linker lengths [23, 24], assuming a tandem construct of fixed linker length is expressed a 1:1 stochiometry in live cells [25], and fitting techniques applied to spectral data [26]. In this paper, we have combined multi-frequency lifetime measurements of the purified biosensor and measurements of both the cleaved and intact biosensor on the microscope in order to determine (ξ).

Simulating Spectra

The measured FRET efficiency (or FRET ratio) can be related to normalized concentration of the biosensor by simulating the spectra that would result from having different combinations of cleaved and intact biosensor in the cell. In order to simulate the spectral distribution $I(\lambda_{Exc}, \lambda_{Em})$ of the emitted intensity from a fluorophore at an excitation wavelength (λ_{Exc}) and emission wavelength (λ_{Em}), several quantities must be known including the excitation light's intensity $P(\lambda_{Exc})$, the extinction coefficients $\varepsilon(\lambda_{Exc})$ at a specific excitation wavelength (λ_{Exc}), the quantum yields (QY), the

concentration of the fluorophore $[C]$, the instrument's efficiencies to detect different wavelengths of light and the reference spectra of the fluorophore whose area is normalized to unity $S_{REF}(\lambda_{Em})$. If FRET is taking place, the FRET efficiency (E) will then be a factor as well to reduce the intensity of the donor's emission and increase the fluorescence emitted from the acceptor. The efficiencies of the detectors are assumed to be uniform over the range of simulated wavelengths. In the analysis and results presented in this paper, correction factors are computed based on the measurement of standards and applied to account for the dependence on this factor.

If the sample contains purely intact biosensor (each donor attached to an acceptor) with a concentration $[C_{Bios}]$, the equation describing the emitted intensity from the donor undergoing FRET can be written as,

$$I_{don}^{FRET}(\lambda_{Exc},\lambda_{Em}) = S_{REF}^{don}(\lambda_{Em})P(\lambda_{Exc})\varepsilon_{don}(\lambda_{Exc})QY_{don}[C_{Bios}](1-E) \quad (3)$$

In parallel, the emitted intensity from an acceptor excited by FRET is as follows,

$$I_{Acc}^{FRET}(\lambda_{Exc},\lambda_{Em}) = S_{REF}^{Acc}(\lambda_{Em})P(\lambda_{Exc})\varepsilon_{don}(\lambda_{Exc})QY_{Acc}[C_{Bios}](E) \quad (4)$$

In order to determine the intensities expected from various combinations of intact biosensors and free (non-interacting) donors and acceptors, the simulations assumed a single fixed concentration of the biosensor. The contribution of cleaved biosensor to this fixed concentration was increased from the case of having purely intact biosensor to the

case of having purely cleaved biosensor. The fractional contribution that each configuration of the biosensor (cleaved or intact) has to the fixed concentration of biosensor is referred to as the species fraction. Therefore, for the intact biosensor and separately for the cleaved biosensor, the species fraction can have values from 0 to 1.

The intensities from the non-interacting donors and acceptors need to be included along with the emission from the intact biosensor to determine the emitted intensity from the set of conditions simulated. With a known concentration of cleaved biosensors referred to as $[C_{Cleave}]$, the spectral contributions from the non-interacting donors and acceptors can be written as

$$I_{don}^{NoFRET}(\lambda_{Exc},\lambda_{Em}) = S_{REF}^{don}(\lambda_{Em})P(\lambda_{Exc})\varepsilon_{don}(\lambda_{Exc})QY_{don}[C_{Cleave}] \quad (5)$$

$$I_{Acc}^{NoFRET}(\lambda_{Exc},\lambda_{Em}) = S_{REF}^{Acc}(\lambda_{Em})P(\lambda_{Exc})\varepsilon_{Acc}(\lambda_{Exc})QY_{Acc}[C_{Cleave}] \quad (6)$$

The spectra of the donor (ECFP) and acceptor (YPet) can then be simulated separately as a function of the species fraction of the intact or cleaved biosensor. The individual emission spectrum from the ECFP and YPet can later be combined to find the intensities in the filter passes used in the live cell experiments.

FRET Efficiency: Lifetimes

Donor's Lifetime

When a fluorescent molecule becomes excited, the molecule can de-excite by a variety of processes including releasing a lower energy photon, inter-system crossing to a triplet state or even non-radiative de-excitation [13, 21, 27]. The measured lifetime of a fluorescent sample is equal to the inverse of the sum of all the rates associated with each

de-excitation pathway available to the excited molecule. In the presence of a nearby acceptor, the excited state of a donor fluorophore will be depleted more rapidly resulting in a shortened lifetime. The FRET efficiency (E) therefore, can be written in terms of the lifetime of the free donor (τ_D) and the lifetime of the donor quenched by FRET (τ_{DA}).

$$E = 1 - \frac{\tau_{DA}}{\tau_D} \tag{7}$$

Please see Derivation 3 at the end of this chapter describing the origins of equation (7). If the donor fluorophore has a multi-component the lifetime, the average lifetime equal to the sum of the constituent lifetimes each weighted by the corresponding species fraction must be used in the calculation of the FRET efficiency.

In the case of the biosensor, there are two configurations of the biosensor and therefore, two discrete FRET efficiencies. When examined on the polar plot, these two FRET efficiencies correspond to two different polar coordinates. The polar coordinate of any linear combinations of the intact or cleaved biosensor will lie on a straight line between the extrema polar coordinates indicative of the purely intact or purely cleaved biosensor.

Acceptor's Time-Dependent Fluorescence

FRET efficiencies can also be determined by observing the time-dependent fluorescence emission of the acceptor. Although the acceptor's lifetime does not vary as a result of FRET, the measured phase delay and modulation ratio of the acceptor will be substantially changed. The measured phase delay of an acceptor undergoing FRET (φ_{AD})

will be the sum of the phase delay of the donor undergoing FRET (φ_{DA}) and the phase delay of the unpaired acceptor (φ_A). In addition, the measured modulation ratio of an acceptor emitting as a result of FRET (M_{AD}) will be the product of the modulation ratio of the donor during FRET (M_{DA}) and the modulation ratio of the directly excited acceptor (M_A).

$$\varphi_{AD} = \varphi_{DA} + \varphi_A \tag{8}$$

$$M_{AD} = M_{DA} M_A \tag{9}$$

The lifetimes that can be calculated from the phase delays and modulation ratios in the above equations are not particularly useful. However, when the polar coordinate indicative of an acceptor undergoing FRET can in some cases, be projected far outside of the universal semi-circle. In certain cases, measuring the time–dependent emission of the acceptor undergoing FRET can generate changes in polar coordinate that are larger than those that would be recorded when collecting emission only from the donor.

The above equations have been derived previously both by convoluting the acceptor's fundamental fluorescence response over the intensity-modulated emission of a donor fluorophore [28]. In this approach, every infinitesimally small part of the donor's fluorescence emission produces a fluorescent decay with a lifetime and spectral distribution which are characteristic of the acceptor. The measured phase delay and modulation ratio of the acceptor undergoing FRET can also be derived by examining measured rate of de-excitation of the acceptor in the presence of the donor with kinetic models [29, 30].

Imaging Systems

All steady-state images of the cells were collected on a Zeiss LSM 710 inverted microscope using a 63x 1.4 NA Plan-Apochromat oil immersion objective (Zeiss, Germany). The excitation sources used were a 405nm laser diode and the 514nm line from an Argon ion laser. The emission wavelengths selected for the experiment were 458nm – 501nm and 528nm – 570nm. The samples containing solutions of purified biosensors and Rhodamine B were imaged using a 20x 0.8 NA Plan-Apochromat air objective (Zeiss, Germany) and the 63x 1.4NA oil immersion objective (Zeiss, Germany).

The lifetimes of the biosensors contained in live cells were detected with a custom-built full-field lifetime imaging system operating in the frequency domain [5, 31, 32]. In this system, the intensity from a continuous 440nm laser (Crystal Laser, Reno NV) is modulated at a frequency of 40MHz by a Pockels cell (Conoptics, Danbury, CT). In order to image only the acceptor, the 488nm line of an Agon ion laser (Uniphase, CA) was used in parallel with the 440nm laser. The intensity-modulated emission from the sample was then detected by an image intensifier (Kentech, England) before being imaged on a CCD camera (Retiga). The dichroic mirror and emission filter selected wavelengths between 460nm and 500nm for imaging the donor (Omega Optical, Brattleboro VT). An additional dichroic mirror and filter passed wavelengths from 500nm to 560nm in order to collect intensity primarily from the acceptor (Omega Optical Brattleboro VT). The live cells were imaged with a 100x 1.3NA oil immersion objective (Lecia, Germany). The reference for the lifetime measurements in the frequency domain was Fluorescein in 0.1N NaOH (lifetime = 4.3ns [31]).

Image Analysis: Steady-State Imaging

The cells imaged on the steady-state microscope were only exposed to light (40% of the power of the 405nm diode) for the actual imaging to avoid photobleaching. Cells were aligned and focused using an external Mercury Halide lamp. Three channels were configured for imaging which are referred to throughout the text as IDD (Excitation: 405nm, Emission: 458nm - 501nm), IDA (Excitation: 405nm, Emission: 528nm – 570nm) and IAA (Excitation: 514nm, Emission: 528nm – 570nm). Two consecutive sets of images were collected to account for bleaching specifically in the channel IDA. Images were also acquired without any sample present for background removal specific to each channel used. Following the correction for photobleaching and removal of background a 3x3 median filter was applied to the images analyzed. The images of the solutions containing the biosensors and separately the Rhodamine B were equivalently median filtered and underwent an analogous background removal. Errors in the measured steady-state FRET efficiencies and FRET ratios were computed with calculations based on the propagation of errors. The details of these calculations can be found in the supplemental derivation.

Image Analysis: Lifetime Imaging

Each of the phase images used to generate a modulation and phase image of the lives were denoised with a custom algorithm specific for the noise characteristic of this intensifier and camera [31]. Background was removed with multi-resolution analysis applying the *Sym8* wavelet [33, 34]. The intensity images presented are the average of the eight phase images collected while homodyning.

Cell Culture

HT-1080 cells (ATCC, Manassas VA) were cultured in DMEM supplemented by 10% FBS. These cells were transfected with Lipofectamine 2000 (Invitrogen, Carlsbad CA) according the manufacturer's instructions and then starved at 0.5% FBS for 36-48 hours prior to imaging. The DNA plasmids transfected into the cells were the ECFP-CL plasmid, which was a generous gift from the Gaskins Lab and the AHLR-variant of the ECFP/YPet biosensor described previously [7]. For imaging, cells were grown on glass-bottomed culture dishes (Cell E&G, Houston, TX). In order to inhibit MT1-MMP activity, a portion of the cells imaged were incubated with 20μM of GM6001 (Merck, Germany) for 12-18 hours prior to imaging.

Fluorometer-based Measurements

The multi-frequency lifetime measurements were carried out using a multi-frequency lifetime fluorometer model K2 (ISS Inc., Champaign IL). An exciting laser emitting a 440nm (Crystal Laser, Reno NV) was intensity modulated and emission was collected through a filter passing 488nm ± 10nm (Chroma, Bellows Falls VT). Quartz polarizers were oriented in the magic angle configuration through the fluorometer-based lifetime measurements. Steady-state spectra were collected on a PC1 fluorometer (ISS Inc., Champaign, IL). Absorbance spectra were taken on an Agilent 8453 Spectrophotometer (Agilent, Santa Clara, CA).

Results

Determining the FRET Efficiency with Time-Dependent Fluorescence

The FRET efficiency of the intact biosensor was calculated from multi-frequency lifetime measurements taken before and after the substrate of the biosensor was cleaved by trypsin. The polyacrylamide gel shown in Supplemental Figure 2.1 demonstrates that trypsin can effectively cleave the substrate of the biosensor. Prior to the addition of trypsin, the band indicates that proteins with masses near 50kD are present. However, trypsin readily cleaved the substrate of the biosensor leaving only proteins with masses near 25kD in the gel. The modulation ratio and phase delay was measured on both configurations of the biosensor at a set of twenty modulation frequencies (Figs. 2.1A and 2.1B). The results from iterative fitting carried out on this data set indicated that each configuration of the biosensor was characterized by a two component lifetime (Table 2.1). On the intact biosensor, the lifetime distribution was dominated by a short lifetime component near 0.92ns resulting in an average lifetime of 0.71ns. After the substrate of the biosensor was cleaved, the average lifetime increased to 2.83ns with the lifetime distribution split between a component at 1.24ns and a component at 4.08ns. Consequently, the FRET efficiency of the intact biosensor was equal to 0.75.

The change in FRET following the cleavage of the biosensor's substrate was also assessed by examining the polar coordinate of each configuration of the biosensor at a modulation frequency of 40MHz (Figs. 2.1C and 2.1D). As suggested by the measurements taken with multiple modulation frequencies, the polar coordinate of the ECFP move from a position near 1ns (gray circle in Fig. 2.1C) to a position between 2ns and 3ns (filled black circle in Fig. 2.1C) as the substrate of the biosensor was cleaved by

trypsin. The sample was imaged on the homodyne FLIM instrument by placing a droplet of solution on a 1.5 coverglass.

When projected on the polar plot, changes in the measured time-dependent fluorescence of the acceptor can also indicate the configuration of the biosensor. In order to characterize the acceptor, the lifetime of a solution of purified biosensor was measured with an excitation wavelength of 488nm (filled black circle in Fig. 2.1D). When projected on the polar plot, YPet, itself, has a single component lifetime near 3.4ns. Without the contribution of bleedthrough and the direct excitation of the YPet, the theoretical polar coordinate of YPet undergoing FRET on this biosensor would be outside of the semi-circle (open gray circle in Fig. 2.1D). The polar coordinate of YPet undergoing FRET has a phase delay equal to the sum of the phase delay of the donor (ECFP) undergoing FRET and the phase delay of the YPet (directly excited). The modulation ratio (length of the vector on the polar plot) describing YPet excited by FRET is also reduced in size with respect to the modulation ratio of the donor (ECFP) undergoing FRET.

However, the emission spectrum of the YPet and that of the ECFP significantly overlap. As a result, finding a set of emission that solely reports on the emission of YPet is not feasible. In addition, the absorbance spectrum of YPet extends into the blue and therefore, it can be directly excited by the 440nm laser. The polar coordinates corresponding to the phase delay and modulation ratio of the intact and cleaved biosensor excited at a wavelength of 440nm and detected through the filter for YPet are shown in Figure 2.1C. Unlike the polar coordinates describing the acceptor in Figure 2.1D, the locations of these polar coordinates reflect the both the overlap in emission between the ECFP and the direct excitation of the YPet. In short the polar coordinates shown in

Figure 2.1C define the trajectory measured experimentally with the samples of purified biosensor.

Steady-State Spectra

The spectral characteristics of the ECFP/YPet variant of the MT1-MMP biosensor were examined with both the excitation wavelength used during the steady-state microscopy (405nm) and during the lifetime imaging experiments (440nm). In Figure 2.2, the spectra of both the intact and cleaved biosensor are presented along the individual contributions of ECFP and YPet computed by spectral unmixing. When excited by either the 405nm or 440nm wavelength, the emission spectra of the intact biosensor are dominated by the spectral contribution of the YPet. In these spectra (Fig. 2.2A and Fig. 2.2C), the amplitude of ECFP's peak is approximately one tenth of the amplitude of the corresponding peak from the YPet.

The spectrum of the ECFP however, became prominent after the substrate of the biosensor was cleaved by trypsin (Fig. 2.2B and Fig. 2.2D. No apparent peak from the YPet was observed in the emission spectrum of the cleaved biosensor at an excitation wavelength of 405nm (Fig. 2.2B). However, there is a small contribution from YPet apparent when the cleaved biosensor was excited at a wavelength of 440nm (Fig. 2.2D). In this case, the YPet is likely being directly excited.

Simulations: Steady-State

Simulations were conducted in order to determine the measured FRET efficiency (steady-state) and the measured FRET ratio as a function of the species fraction of the intact biosensor. The previously discussed in-vitro measurements taken on the biosensor (and published in [6]), the reported extinction coefficients and quantum yields of the

ECFP [35] and YPet proteins [36] and reference spectra from the Tsien Lab [37] supplied the physical constants for the simulations. All possible combinations of intact and cleaved biosensors were sampled from the case where all of the biosensors were entirely cleaved to the case where all of the biosensors were completely intact. These simulations assumed an excitation wavelength of 405nm and that the fluorescence emission was detected through the two sets of emission wavelengths used during the steady-state live cell imaging (Fig. 2.3D).

As shown in Figure 2.3A, the FRET ratio (YPet/ECFP) for this biosensor increases exponentially with increasing species fraction of the intact biosensor. The rate of change in FRET ratio (YPet/ECFP) with respect to the species fraction of the intact biosensor increases dramatically with increasing species fraction. Therefore, a given change in the FRET ratio (YPet/ECFP) could correspond to either a large or small change in the actual species of the biosensor (intact or cleaved) depending on the initial species of the biosensor present. If the opposite FRET ratio (ECFP/YPet) is considered, the rate of change in the FRET ratio is also not constant with an increasing species fraction of the intact biosensor (Fig. 2.3B). The largest rate of change in the FRET ratio (ECFP/YPet) occurs when the species fraction of the intact biosensor is less than one half (Fig. 2.3B). Even in the case when the two configurations of the biosensors are defined as folded versions of a donor and acceptor tandem construct, the relationship between the species fraction of a particular configuration of the biosensor and the measured FRET ratio will still be exponential in character.

However for the cyan variant of the MT1-MMP biosensor, the FRET efficiency measured by steady-state methods, increases linearly with the increasing species fraction

of the intact biosensor (Fig. 2.3C). Therefore, unlike either of the FRET ratios, the rate of change in the measured FRET efficiency is constant with changing species fraction of the intact biosensor.

Simulations: Time-Dependent

In parallel, the polar coordinates calculated from the phase delay and modulation ratio describing the biosensor were also simulated as a function of increasing species fraction of the intact biosensor (Fig. 2.4). In other words, the sample in this simulation was a solution of biosensors with a fixed concentration. Relative to that fixed concentration, the amount of cleaved and intact biosensors was changed from the condition of having purely intact biosensors to the condition of having purely cleaved biosensors. In order to parallel the conditions of the lifetime imaging experiments, these simulations assumed an excitation wavelength of 440nm and an emission filter specific only for the fluorescence emission of the ECFP (<500nm). As discussed previously, a polar coordinate of a system containing two populations of fluorophores will be sum of the polar coordinates of the constituent fluorophore's polar coordinate where each is weighted by its specific fractional contribution to the steady-state intensity. The trajectory of points on the polar plot (dotted gray line in Figs. 2.4A, 2.4B and 2.4C) describing all linear combinations of the intact (near 1ns) and cleaved biosensor (near 2.5ns) was based on the previously described in-vitro measurements [6] (and was also discussed in the previous section of this chapter).

In the simulations on the polar plot, the species fraction of the intact biosensor was incrementally lowered and the resulting polar coordinates are shown in Figures 2.4A, 2.4B and 2.4C. The simulations indicate that even a very small amount of cleaved

biosensors (species fraction of intact biosensor = 0.75) can significantly move the polar coordinate from the intact position (near 1ns) toward the polar coordinate of the cleaved biosensor (near 2.5ns) (Fig 2.4B). Therefore, even a twenty five percent reduction in the species fraction (normalized concentration) of the intact biosensor results in the detected intensity from the cleaved biosensor being greater than that of the intact biosensor. When the species fractions of the intact and cleaved biosensor were equal (Fig. 2.4C), only twenty percent of the resulting intensity was from the intact biosensor.

By further increasing the amount of cleaved biosensor in the simulation from a state where species fraction of the intact biosensor is one half to state where the species fraction of the intact biosensor is zero, only small changes in polar coordinate (approximately 4^{o} in phase delay or 0.06 in Cartesian distance) remain that can be used to quantify these changes in the configuration of the biosensor. However, despite the small change in polar coordinate between the condition of having a species fraction of the intact biosensor at one half and that of having purely cleaved biosensor, the simulated FRET ratio (YPet/ECFP) would change from 1.73 to 0.37. In parallel, the simulated FRET ratio (ECFP/YPet) would change from 0.58 to 2.7. Hence, if the species fraction (normalized concentration) of the intact biosensor changes from one half to zero, there is only a small change in the time-dependent fluorescence emission detected by FLIM but at the same time, there can be more than a four-fold change in the FRET ratio.

Steady-State Measurements of FRET

Measurements of solutions

A solution of intact biosensors was measured using the 20x Plan-Apochromat air objective. This solution of intact biosensor has a known FRET efficiency and FRET ratio

and therefore, can be used to find the corrections necessary for accurate measurements on live cells. The 20x air objective had a large excitation volume and hence provided much better signal-to-noise ratio for measuring the fluorescence from quenched donor (ECFP) in this solution sample than the 63x Plan-Apochromat oil immersion objective. The wavelength-dependent transmission of this objective was compared to that of the 63x oil immersion objective using a sample of cleaved biosensor. No significant differences were noted. The wavelengths selected for these experiments are shown along with the emission spectra of ECFP and YPet in Figure 2.3D. The collected intensities (IDD, IDA and IAA) describing the intact biosensor (Table 2.2), do indicate that the fluorescence emission of the donor (ECFP) was quenched. The calculated FRET ratio (ECFP/YPet) from the measurements taken on the microscope was 0.2 ± 0.05.

A separate measurement of the cleaved biosensor and separately a solution of Rhodamine B with the 20x air objective resulted in a value of (ξ) equal to 0.84 ± 0.23. By cleaving the biosensor with trypsin, the emission of the non-interacting (no FRET) YPet and ECFP could be measured. The fluorescence emission of each protein could be independently measured by cleaving the biosensor because the absorbance of the YPet protein is negligible at an excitation wavelength of 405nm as is the absorbance of ECFP at an excitation wavelength of 514nm. When combined with the previous intensity measurements taken on the FRET standard, this value of (ξ) yielded a value for the steady-state FRET efficiency of the solution of intact biosensors equal to 0.79 ± 0.0427. The factor (ξ) was also determined by measuring solutions of cleaved biosensor and separately solutions of Rhodamine B with the same 63x Plan-Apochromat oil immersion objective used to image the live cells. Measurements of four sets of solutions were made

independently. The average value and standard deviation of (ξ) determined from this set of measurements was 0.86 ± 0.29.

Correction Factors for Live Cell Imaging

The measurements of solutions on the steady-state microscope were then applied to determine correction factors accounting for transmission efficiencies of the microscope's dichroics and emission optics. Comparisons were made to equivalent samples of solutions measured on both a time-resolved and a corrected steady-state fluorometer (Figs. 2.1 and 2.2). The FRET efficiency of the intact ECFP/YPet version of the MT1-MMP has been previously determined using multi-frequency lifetime measurements as 0.75. Using a fully corrected steady-state fluorometer, we have determined the FRET ratio (ECFP/YPet) of the intact MT1-MMP biosensor excited at 405nm to be 0.17.

Correcting for the FRET ratio can be done simply by comparing the FRET ratios collected from the microscope and fluorometer in order to determine a correction factor. Correcting the microscope's measurement of FRET Efficiency primarily stems from using two different dichroic mirrors to measure the sample of Rhodamine B at excitation wavelengths of 405nm and separately 514nm when determining (ξ). All other wavelength-dependent artifacts are considered in the bleedthrough coefficients applied when calculating the FRET efficiency. Therefore, the factor (ξ) was corrected by simulating the FRET efficiency as a function of (ξ) (Supp. Fig. 2.2). Intensity values measured from the FRET standard on the steady-state microscope were entered into this simulation to compute the FRET efficiency at each value of (ξ). A reduced value of (ξ)

equal to 0.66 corresponding to the known FRET efficiency of 0.75 was the corrected value used in this study.

Live Cells: Steady-State Imaging

Bleedthrough Coefficients

HT-1080 cells transfected with DNA encoding ECFP only were imaged on the steady-state microscope through the filters described in Figure 2.3D. In order to find the coefficient (b_1), ten cells were imaged. The cells in each image (IDD and IDA) were segmented and the intensities from each image were averaged separately to calculate (b_1). An example of one of the HT-1080 cells examined is shown in Supplemental Figures 2.3A and 2.3B. The emitted fluorescence was distributed uniformly throughout the cells transfected with the ECFP-only plasmid. The resulting values and corresponding uncertainties for (b_1) are shown in Table 2.3. In order to asses the quality of ECFP's expression, spectral images of several HT-1080 cells were also collected (Supp. Fig. 2.3C). Intensities from these spectral images are plotted at their corresponding set of wavelengths and are compared to the know reference spectrum of ECFP in Supplemental Figure 2.3D. When compared to the reference emission spectrum of ECFP, both the position of the emission maximum and the overall shape of the spectrum measured in the live cells indicated that the ECFP was properly expressed.

The bleedthrough coefficient (b_2) which is the ratio of YPet's fluorescence directly excited at 405nm and the fluorescence directly excited at 514nm was assumed to be zero.

HT-1080 Cells

A series of HT-1080 cells transfected with the ECFP/YPet MT1-MMP biosensor were examined in order to determine the FRET efficiency and FRET ratio with steady-state imaging (Fig. 2.5). As mentioned previously, HT-1080 cells endogenously express MT1-MMP. Consequently, these cells will contain a mixture of intact and cleaved biosensors.

In the first cell examined shown in Figures 2.5A, 2.5B and 2.5C, images were collected with all three excitation and emission filter settings (IDD, IDA and IAA). By comparing the image collected only from the donor's fluorescence (IDD) and that from only the acceptor's fluorescence (IAA), there is a definite region along the perimeter of the cell where there is no staining (fluorescence) from the acceptor (YPet) indicating that the biosensor is likely cleaved. In the central portion of the cell, both the donor and the acceptor are present.

Regions of interest were selected in both the periphery and center of the cell for analysis (white boxes in Fig. 2.5A). On a pixel-wise basis, the FRET ratio and FRET efficiency were calculated in each region and the resulting distributions are shown as histograms in Figures 2.5D and 2.5F. Graphically, the distributions from each region of interest describing the FRET efficiency and separately the FRET ratio have definite peaks and do indicate that there is a low FRET state along the perimeter of the cell (regions 3 and 4) and a higher FRET state in the cell's center (regions 1 and 2).

The average intensities from each region collected through the donor's channels IDD and IDA were also used to quantitatively determine the FRET efficiency and FRET ratio (Table 2.4). The calculation of the uncertainty in the FRET efficiency and FRET

ratio is described in derivation 2. The low FRET efficiency (0.02 in region 3 and 0.03 in region 4) and high FRET ratio (2.17 in region 3 and 2.07 in region 4) indicate that the majority of the biosensors are cleaved. However, in the central part of the cell where some of the biosensor is expected to be intact, the FRET efficiencies (0.178 in region 1 and 0.177 in region 2) are lower than the FRET efficiency of the intact biosensor measured in vitro. The FRET ratio calculated in the central part of the cell (1.24 in region 1 and 1.24 in region 2) is also higher than the FRET ratio describing the purely intact biosensor in vitro.

In order to look for higher extents of FRET in the cells, the FRET efficiency and FRET ratio were also examined globally in a pixel-wise manner (color images in Figs. 2.5E and 2.5G). However, as indicated in the color renderings, the values for the FRET efficiency and FRET ratio throughout the cell do not show that a higher FRET state exists. Furthermore, the FRET efficiencies and FRET ratios examined in the entire set of cells (data not shown) analyzed did also indicate that the maximum FRET efficiency detected was near 0.3.

In the course of the steady-state measurements, the spectral characteristics of various regions of the transfected HT-1080 cells were also studied to see if the recorded spectra reflect these low FRET measurements (Supp. Figs. 2.4 and 2.5). In both of the presented cases, regions of interest were selected in regions along the edge of the cell (regions 1 and 3) and in the center of the cell near the nucleus (region 2). As before, these regions were selected to highlight areas of the cell containing cleaved biosensor and separately, the intact biosensor. An excitation wavelength of 405nm was used in this experiment.

In the regions along the perimeter of the cell (Supp. Figs. 2.4B, 2.4D, 2.5B and 2.5D), the dominant feature each of the spectra was the emission spectrum of the ECFP. There were no deviations in the intensity near 530nm (YPet's) emission peak indicating FRET. Furthermore, in these regions along the edge of the cell (Supp. Figs. 2.4B, 2.4D, 2.5B and 2.5D, both the relative peak intensity and the shape of the reference emission spectrum of ECFP overlapped well with the data collected from the cell's images. However, the emission spectrum collected in the center of the cell (Supp. Figs. 2.4C and 2.5C) did indicate a deviation in intensity from the spectrum of pure ECFP near the emission peak of the YPet (~530nm). In these plots, the measured spectrum is accompanied by a simulated spectrum containing a mixture of intact and cleaved biosensor as a reference (gray line). In both cases (Supp. Figs. 2.4C and 2.5C), the measured and reference spectra matched the data well and reflects qualitatively the low amount of FRET detected with the steady-state FRET efficiency and FRET ratio.

HT-1080 Cells Treated with Inhibitor

A set of HT-1080 cells containing the ECFP/YPet version of the MT1-MMP biosensor were pre-incubated with the MMP inhibitor GM6001 prior to imaging (Fig. 2.6). The incubation with GM6001 will therefore, prevent the biosensor from being cleaved leaving it intact in the cell.

Intensity images of the GM6001-treated cells were also acquired through the channels IDD, IDA and IAA (Figs. 2.6A, 2.6B and 2.6C). In these cells, the staining pattern from the images collected with only the donor's fluorescence (IDD) matched (co-localized) well with the images collected using only the acceptor's fluorescence (IAA).

There was no discernable edge or peripheral region in this cell that lacked staining by the acceptor YPet.

A set of regions (white boxes in Fig. 2.6A) were selected to analyze the FRET efficiency and FRET ratio. The corresponding distributions of the FRET efficiencies (Fig. 2.6D) and FRET ratios (Fig. 2.6F) determined in a pixel-wise manner were fairly uniform in both shape and position of the peak throughout the four regions selected within the cell. As before, the average intensities from the four regions of interest were used to compute the FRET efficiency and FRET ratio (Table 2.5). The calculated FRET efficiencies spanned the range from 0.21 to 0.27 while the calculated FRET ratios ranged from 1.13 to 0.92. Although these FRET efficiencies are higher (and the FRET ratios are lower) than those found in the cell not treated with GM6001, they do not parallel the in-vitro measurements and therefore possibly indicate that the majority of the biosensors are cleaved in these cells.

In order to look for areas in the cells with higher amounts of FRET, the FRET efficiency and FRET ratio was mapped on a pixel-wise basis throughout the intensity image of the cell (Figs. 2.6E and 2.6G). In these images, there were no discernible regions that indicated higher FRET efficiencies (lower FRET ratios) than those analyzed in the previously described analysis.

HT-1080 cells transfected with the ECFP/YPet variant of the MT1-MMP and pre-treated with the GM6001 inhibitor were also imaged on a spectral imaging system with a 405nm excitation wavelength (Supp. Fig. 2.6). The purpose of these experiments was to confirm the observations noted in the previous steady-state measurements of low FRET specifically under the conditions when the biosensor was intact (MMP inhibitor

treatment). Individual images were collected from a wavelength of 429nm to 625nm with steps of approximately 9.8nm. The intensities analyzed from the three regions of interest (white boxes in Supp. Fig. 2.6A) are plotted versus wavelength in Supplemental Figures 2.6B 2.6C and 2.6D. Even without applying linear unmixing, the dominant feature occupying most of the intensity in the plotted spectra is the emission spectrum of the ECFP (peak at 480nm). Only a small peak from YPet's emission spectrum is visible as well near 530nm. Even though the regions selected in this analysis spanned the majority of the cell's body, no significant differences were apparent in the relative amplitudes of ECFP's and YPet's emission peaks or in the overall shape in the recorded spectra in the various regions. Furthermore, the relative amplitudes of ECFP's emission peak and YPet's emission peak do not resemble those in the previously measured or simulated emission spectrum of the purely intact biosensor.

Live Cells: Lifetime Imaging Using the Donor (ECFP)

HT-1080 Cells

Images of the HT-1080 cells were collected on the homodyne FLIM instrument at a modulation frequency of 40MHz. A 440nm and separately a 488nm laser line were used to excite each sample. The fluorescence emission was collected through the filter pass specific to each laser line shown in Figure 2.7C. The 440nm laser and the corresponding filter observed emission from the donor ECFP while exciting primarily the donor (ECFP) while the 488nm laser and filter selectively excited and collected the emitted fluorescence from the acceptor YPet.

In the cell images shown in Figure 2.7, there are areas on the periphery of the cell clearly visible in the channel specific for ECFP (Fig. 2.7A) which are not apparent in the

image collected with the 488nm laser (Fig. 2.7B). However, the staining in the central regions of the cell was similar when collected using the 440nm and 488nm lasers with their corresponding filters. Therefore, in these peripheral regions of this cell, there is a lack of YPet which does indicate that the biosensor is likely cleaved.

The phase delay and modulation ratio were gathered from four regions of interest in the cell (white boxes in Fig. 2.7A) which included areas in the center (regions 2 and 3) as well as areas along the perimeter of the cell lacking YPet (regions 1 and 4). The polar coordinates describing the pixels in these regions are shown in the scatter plots in Figure 2.7D. Despite the differences in staining of the ECFP and YPet in the various regions of the cell, the polar coordinates gathered from all of the four regions were all projected at a position just above 2ns. Even in the central regions of the cell, the polar coordinates did not indicate a strongly quenched lifetime of the donor (ECFP) corresponding to the intact biosensor. The wide distribution of points on the polar plot associated with each region of interest is the result of noise in the detection system [31]. Consequently, the center of each distribution shown in the polar plots (Fig. 2.7D) is indicative of the fluorescent species in that region. The extrema points specifically in the larger distributions of polar coordinates taken from the areas of the cell with low signal are not representative of unique fluorescent species but likely a part of a larger distribution.

In addition to examining specific regions within the cell, the two intensity images of the cells were also segmented (red borders in Figs 2.7A and 2.7B) to examine the entire edge and center of the cell on the polar plot. The edge is defined as the area between the boundary plotted as a red line in Figure 2.7A and the boundary plotted in Figure 2.7B. The center is simply the area contained in the boundary plotted in Figure

2.7B. The mean polar coordinates of the edge and central sections of the cell along with standard deviations in both the x- and y-dimensions are presented on the polar plot in Figure 2.7E. The polar coordinate describing the edge shows a likely contribution from residual background in this area of low signal but this polar coordinate does not differ significantly from the polar coordinate calculated from the pixels in the center of the cell. The polar coordinate of the background resides in the lower left corner of the polar plot representing un-modulated signals entering the detector.

HT-1080 Cells Treated with Inhibitor

The polar coordinate of the intact biosensor was further examined by pre-incubating the HT-1080 cells with GM6001 to prevent the cleavage of the biosensor. Imaging was also carried out with the lasers and filters described in Figure 2.7C in order to examine to the emission from the donor (ECFP) at an excitation wavelength of 440nm and separately the emission from the acceptor (YPet) by directly exciting the sample with a 488nm laser. The images gathered from the ECFP's emission (Fig. 2.8A) and YPet's emission (Fig. 2.8B) show a high degree of co-localization. In other words, the features in Figure 2.8A such as the nucleus, bright region around the nucleus and the edge of the cell are clearly visible in the images shown in both Figures 2.8A and 2.8B.

In this analysis, pixels from various regions of interest in the cell (white boxes in Fig. 2.8A) were projected as polar coordinates on the scatter plots shown in Figure 2.8C. In all cases, the polar coordinates collected from the cell remained in a position just above 2ns. None of the polar coordinates indicated a strongly quenched lifetime of the donor (ECFP) as detected for the intact biosensor in the in-vitro measurements but

instead, closely paralleled the positions of the polar coordinates describing the untreated HT-1080 cell.

Live Cells: Lifetime Imaging using the Acceptor (YPet)

HT-1080 Cells

HT-1080 cells transfected with the ECFP/YPet-variant of the MT1-MMP biosensor were imaged in order to examine the acceptor's time-dependent fluorescence on the homodyne lifetime imaging system (Fig. 2.9). Each cell was imaged with three separate excitation sources and emission filter combinations specific for either the donor, the acceptor while being excited at the donor's excitation wavelength (440nm) or the acceptor being directly excited (488nm) (Figs. 2.9A, 2.9B and 2.9C).

Without an MMP inhibitor present, the initial set of cells examined contained a mixture of intact and cleaved biosensors. In the first cell imaged, the average intensity image of the cell (gathered from the eight phase images), using the excitation source (440nm) and emission filter specific for ECFP is shown in Figure 2.9A. The intensity image collected with the same excitation laser but through a filter for YPet contains the same morphological features of the cell shown in Figure 2.9A. For example, the bright region surrounding the nucleus as well as the dimmer edge (peripheral regions) are consistent in the images of the cells presented in Figure 2.9A and Figure 2.9B. However, when the cell was imaged by selectively exciting the YPet, the edges of the cell (near regions of interest #2 and #4 in Fig. 2.9B) were not visible in the resulting intensity image (Fig. 2.9C). The polar coordinates from the pixels in the ROIs shown in Figure 2.9B were taken from the images acquired with the 440nm exciting laser and the filter specific for YPet and projected on the polar plot (Fig. 2.9D). In regions #2 and #4 located

at the bottom of the cell lacking staining from YPet, the polar coordinates moved toward shorter lifetimes (near 2ns) indicating that the biosensor was possibly cleaved. As discussed previously, this position on the polar plot also corresponds to the location of non-interacting ECFP measured in a solution of purified biosensor. In the regions containing intensity from both the ECFP and YPet, the polar coordinates remained longer lifetimes (near 3ns) possibly indicating that the biosensor was possibly intact.

Image segmentation was applied to the images of the HT-1080 cells collected in this acceptor-based FLIM experiment in order to study the entire edge and center of the cell. As before, the center of the cell is simply the area contained within the boundary depicted in Figure 2.9C. The edge of the cell is essentially the area of the cell lacking staining from YPet and is therefore, defined as the part of the cell located between the red boundaries drawn in Figures 2.9B and 2.9C. In general, the average polar coordinate calculated from the center of the cell was closer to longer lifetimes (near 3ns) than the average polar coordinate computed from the pixels along the edge of cell (Fig. 2.9E). Given the low signal along the edge of the cell, the average polar coordinate calculated from the pixels along the edge of the cell appears to be being slightly pulled toward the area on the polar plot indicative of un-modulated background. However, the separation in polar coordinate between the edge and center of the cell (between approximately 2ns and 3ns) are consistent with the analysis of the specific regions throughout the cells.

HT-1080 Cells Treated with Inhibitor

HT-1080 cells were also pre-treated with the MMP inhibitor GM6001 and imaged with emphasis on the polar coordinates of the YPet. The intensity images were collected with the three excitation laser and filters used previously. These are labeled as ECFP

(Fig. 2.10A), YPet undergoing FRET (Fig. 2.10B) and YPet directly excited (Fig. 2.10C). Although the intensities vary in each of the three images, the primary features of the cell such as the nucleus, edge and bright region surrounding the nucleus were apparent in each of the images. In other words, there was apparent staining by both ECFP and YPet throughout the entirety of the cell itself. The polar coordinates from the pixels within the four regions of interest shown in Figure 2.10B are projected on the scatter plots in Figure 2.10D. Regardless of whether the region was selected near the edge or center of the cell, the polar coordinates consistently remained near 3ns on the polar plot.

Discussion

The presented measurements taken on the MT1-MMP biosensor transfected into HT-1080 cells using the FRET ratio, steady-state FRET efficiency and FLIM verified that changes in FRET detected by the steady-state methods did not correspond to significant changes in the measured time-dependent fluorescence of the donor ECFP. Throughout, the images of the HT-1080 cells collected with FLIM, there was very minimal quenching of the donor's (ECFP's) lifetime with nearly all polar coordinates remaining in a region of the polar plot slightly above 2ns. However, some variation in the polar coordinate of the acceptor (YPet) was recorded spanning an area on the polar plot between 3ns and 2ns. In parallel, the measured steady-state FRET efficiency in the cell images had a range of nearly zero to maximum of approximately 0.3 throughout the different organelles of the cells examined. Despite the small variations in the time-dependent fluorescence of the donor measured by FLIM, the FRET ratio (ECFP/YPet)

still had the largest change in value ranging from nearly one to two when different regions of the cells were compared.

The presented simulations imply that the results gathered from the different methods for detecting FRET may be indicative of a high background of non-interacting donor (ECFP) in the cells analyzed. In the simulation examining the measured FRET ratio (ECFP/YPet) as function of the species fraction (normalized concentration) of the intact biosensor, the largest changes in FRET ratio are observed when the species fraction is less than 0.4. In this range of species fraction of the intact biosensor (0 to 0.4), the simulated changes in the measured steady-state FRET efficiency would be on the order of 0.3 to 0.5. At the same time, further simulations predict that there would be no detectable change in the polar coordinate of the donor if the species fraction of the intact biosensor was changed from zero to 0.4. Although a precise comparison between the measurements taken on live cells and the data collected in vitro cannot be done without extensive analysis of the expression of the biosensor and environmental perturbations on the protein's photophysics, the most likely explanation of the experimental observations is that there is a high background of non-interacting ECFP. In other words, the measurements examining the biosensor in the live HT-1080 cells strongly imply that the biosensor is expressed in a manner closely paralleling its expression for the in-vitro analysis, but that a large majority of the donors are not undergoing FRET in the live HT-1080 cells.

Other interpretations of data such as the possibility that the FRET efficiency of the intact biosensor is smaller in the live HT-1080 cells than in the bacterial cells used to extract the biosensor in-vitro are simply not supported by the measurements. Examples of

such variable expressions between the solution of biosensors examined in vitro and those examined in live cell HT-1080 cells would include a different mutual orientation of the donor and acceptor. If the intact biosensor itself, had a smaller FRET efficiency when expressed in the live HT-1080 cells when compared to the solution of biosensors studied from the in-vitro purification, two populations of polar coordinates would be clearly observed from the lifetime images of the live cells indicative of the measured steady-state FRET efficiency which spanned values from zero to 0.3. In this case, a change in the lifetime of the ECFP as a result of FRET would be on the order of 0.5ns to 0.8ns (assuming the lifetime of ECFP is near 2ns) and easily resolvable on the lifetime imaging system. However, in the presented data, the position of the polar coordinates examined from regions of the cell with no staining by YPet were not clearly distinguishable from the polar coordinate examined in areas of the cells stained by both YPet and ECFP. The lifetime of pure ECFP has been previously shown to vary as a function of both ion concentration and pH [38]. Therefore, it is expected that lifetime of the pure ECFP as indicated by the in-vitro measurements or by values taken from the literature, may not perfectly match the polar coordinate in the measured HT-1080 cells. However, the lack of variation in the polar coordinates likely describing the intact and cleaved biosensor suggests that there is a high background of non-interacting ECFP.

The fluorescence emission of several variants of the cyan and yellow fluorescent proteins can be perturbed by factors in their local environment. For example, certain ranges of intracellular pH have been previously shown to diminish the absorbance of the yellow fluorescent proteins, making them poor acceptors for FRET in cells [39]. In a recent paper, it was reported that even the normal levels of ATP in a cell can significantly

reduce the amount of FRET taking place between the yellow and cyan fluorescent proteins expressed as a tandem protein [40]. The ATP-dependent effects however were shown to be specific to ECFP and were not apparent in parallel studies of the cyan variant Cerulean. It is also quite possible that the maturation times of the ECFP and YPet may be different and therefore contribute to a background of unpaired ECFP.

However, even with environmental perturbations, definite changes in the polar coordinate were observed when the YPet's emission was imaged with FLIM while exciting the donor ECFP. In these experiments, polar coordinates moved between two pools of lifetimes on the polar plot (between 2ns and 3ns), which were possibly indicative of the cleaved and intact biosensor. Although the trajectory of the polar coordinates recorded during the live cell experiments paralleled the trend observed during the in-vitro experiments, there was a definite bias in the live cell experiments toward the polar coordinate of the non-interacting ECFP. Throughout the regions analyzed during the experiments examining the acceptor with FLIM, none of the polar coordinates were in the range of 3ns to 4ns that were predicted in the in-vitro measurements. At this time, there is no reported environmental perturbation that has been shown to vary the lifetime of YPet by more than one nanosecond. Despite the apparent change in polar coordinate observed in these experiments, the variation in polar coordinate may simply arise from the presence or lack of YPet in the regions analyzed. YPet itself, can be directly excited at 440nm and contribute intensity comparable to that from ECFP in the wavelength range used to observe YPet in this chapter. As a result, even in the case where there is no FRET taking place, the change in emission from non-(or weakly) interacting ECFP to that of directly excited YPet and non-(or weakly) interacting ECFP would lead to a change in

polar coordinate similar to that observed in the live cell experiments. The results presented studying YPet's emission with FLIM therefore, also imply a low state of FRET. If the polar coordinates were observed in areas on the polar plot near longer lifetimes (>3ns), there would be evidence for significant energy transfer taking place.

Conclusions

In general, several photophysical characteristics of the fluorescent proteins selected for ratiometric biosensors may not suitable for detection with FLIM and analysis on the polar plot. The design of many popular ratiometric biosensors has been centered on having extremely bright and well absorbing acceptors paired with very dim donors. As a result of energy transfer, the donors are highly quenched making them much more difficult to detect. On the polar plot, the polar coordinate generated by multiple fluorescing species in the same portion of the cell is the sum of the polar coordinates of the constituent fluorescent species, each weighted by their respective contribution to the measured intensity. Consequently, if there is a substantial difference in intensity between the donor's emission on the intact and separately on the cleaved biosensor, even small amounts of the cleaved biosensor can strongly obscure the polar coordinate with a high background of unpaired donor.

Regardless of the type of measurement applied to study the biosensor in cells, the measurements and proposed models possibly suggest that the true physical dynamic range of this biosensor is small and therefore, making conclusions about the configuration of this biosensor in cells remains difficult. The exponential relationship between the measured FRET ratio and the species fraction of the intact biosensor can also

lead to false positives if large changes in FRET ratio such as those observed in the chapter, are interpreted as comparable changes in the actual species of the biosensor present. However, at the same time, the measurements taken on biosensors expressed in the live cells with FLIM readily indicated that there is likely a high background on non-interacting donor simply with a graphical inspection of the data on the polar plot. When analyzed on the polar plot, the data collected with FLIM have the unique advantage that the species of the biosensor can be extracted directly from the measured data without the need for extensive modeling, fitting or corrections.

Newly developed fluorescent proteins including those which absorb and emit light at longer wavelengths (>550nm) can improve the reliability in the detection of the configuration of intracellular FRET-based biosensors in live cells [41, 42]. Already, the mOrange2/mCherry variant of the MT1-MMP biosensor has been shown to accurately report the sub-cellular activity of the MT1-MMP enzyme with high contrast in live HT-1080 cells [43].

Derivation 1: Calculation of the FRET Efficiency from Steady-State Measurements

The equations relating measured various steady-state intensities to the FRET efficiency can be derived analytically by first considering the emission from the donors and acceptors in the image without FRET referred to as (I_D) and (I_A). In other words, the intensities (I_D) and (I_A), are that which would have been emitted by the actual concentration of donors and acceptors in an area of the image as if they were all non-interacting.

Next, it is assumed that you have a solution containing a uniform volume of molecules (donors conjugated to acceptors) undergoing FRET. Each of the spectra discussed previously in the derivation of FRET efficiency with steady-state measurements can then be written in terms of (I_D) and (I_A).

$$I\left(\lambda_{EX}^{D},\lambda_{EM}^{D}\right)=I_D\left(1-E\right) \tag{A1.1}$$

$$I\left(\lambda_{EX}^{D},\lambda_{EM}^{A}\right)=I_D\left(1-E\right)b_1+I_A b_2+I_D E\left(\frac{1}{\xi}\right) \tag{A1.2}$$

$$I\left(\lambda_{EX}^{A},\lambda_{EM}^{A}\right)=I_A \tag{A1.3}$$

The FRET efficiency (E) can then be solved for simply in terms of the measured intensities and correction factors defined previously.

$$E=\frac{\xi\left(I\left(\lambda_{EX}^{D},\lambda_{EM}^{A}\right)-b_1 I\left(\lambda_{EX}^{D},\lambda_{EM}^{D}\right)-b_2 I\left(\lambda_{EX}^{A},\lambda_{EM}^{A}\right)\right)}{I\left(\lambda_{EX}^{D},\lambda_{EM}^{D}\right)+\xi\left(I\left(\lambda_{EX}^{D},\lambda_{EM}^{A}\right)-b_1 I\left(\lambda_{EX}^{D},\lambda_{EM}^{D}\right)-b_2 I\left(\lambda_{EX}^{A},\lambda_{EM}^{A}\right)\right)} \tag{A1.4}$$

In the simulations examining the FRET efficiency (E) as a function of the species of the intact biosensor, the concentration of cleaved biosensor was increased relative to the concentration of intact biosensors by adding terms to the above equations accounting for non-interacting (No FRET) constituents.

Derivation 2: Calculations of Uncertainty for Steady-State Measurements of the FRET Efficiency and FRET Ratio

When the FRET efficiency from the steady-state measurements and corrections were calculated, the uncertainty in the FRET efficiency was based solely on the uncertainty in the intensity measurements referred to as (δIDD) and (δIDA). The bleedthrough coefficients ((b_1) and (b_2)) and the ratio of the quantum yields of the donor and acceptor (ξ) were assumed to be fixed. A propagation of errors calculation then determined the uncertainty in the FRET efficiency (δE) shown below,

$$\delta E = \sqrt{\left(\frac{\partial E}{\partial IDD}\delta IDD\right)^2 + \left(\frac{\partial E}{\partial IDA}\delta IDA\right)^2} \qquad \text{A2.1}$$

In equation A2.1, the terms $\left(\frac{\partial E}{\partial IDD}\right)$ and $\left(\frac{\partial E}{\partial IDA}\right)$ are the partial derivatives of the FRET efficiency with respect to the intensities collected from the channels (IDD) and (IDA).

$$\frac{\partial E}{\partial IDD} = \frac{-\xi IDA}{\left(IDD + \xi IDA - \xi b_1 IDD\right)^2} \qquad \text{A2.2}$$

$$\frac{\partial E}{\partial IDA} = \frac{\xi IDD}{\left(IDD + \xi IDA - \xi b_1 IDD\right)^2} \qquad \text{A2.3}$$

Determining the FRET ratio in the cell images required only one correction accounting for differences in the wavelength sensitivity of the detection system. Therefore, in order to find the uncertainty in the FRET ratio (referred to as (δR)), the wavelength-dependent correction was assumed fixed and only the uncertainty in the measured intensities (IDD) and (IDA) contributed in the propagation of error calculation shown below,

$$\delta R = \sqrt{\left(\frac{\partial R}{\partial IDD}\delta IDD\right)^2 + \left(\frac{\partial R}{\partial IDA}\delta IDA\right)^2} \qquad \text{A2.4}$$

In this case, the derivatives of the FRET ratio with respect to the measured intensities (IDD) and (IDA) take the following form,

$$\frac{\partial R}{\partial IDD} = \frac{1}{IDA} \qquad \text{A2.5}$$

$$\frac{\partial R}{\partial IDA} = \frac{-IDD}{(IDA)^2} \qquad \text{A2.6}$$

Derivation 3: The Mathematics Relating the FRET Efficiency to Measured Lifetimes of the Donor

The excited state of a donor is depleted more rapidly in the presence of an acceptor. The depletion of the excited state of a fluorescent molecule can be modeled as a first order kinetic process where the system as equilibrated to as a quasi-state before returning to the ground state energy. In other words, once the excited molecule has reached the lowest vibrational level in the excited state, the pathway by which it returns to the ground state is random. However, each pathway has an associated rate constant

(referred to as (k)) indicating its average frequency of occurrence. While, undergoing FRET, the lifetime of the donor therefore shortens as a result of a new de-excitation pathway opened by the presence of the acceptor. In short, the lifetime of the donor undergoing FRET (τ_{DA}) and the lifetime of donor without an acceptor (τ_D) can be related to FRET efficiency (E) by the following equation.

$$E = 1 - \frac{\tau_{DA}}{\tau_D} \qquad \text{A3.1}$$

In order to derive equation (A3.1), the FRET efficiency has to be related to the various rates of the deactivation as shown,

$$E = \frac{k_T}{k_T + \sum_{i \neq T} k_i} \qquad \text{A3.2}$$

In this representation, the FRET efficiency compares the rate of energy transfer to the rates of all available de-excitation pathways in the system and is therefore, analogous to the quantum yield of energy transfer. In order to use equation (A3.2) to derive equation (A3.1), the lifetimes of the donor (τ_{DA}) and (τ_D) can also be written in terms of the rates of the de-excitation pathways present in the system.

$$\tau_{DA} = \frac{1}{k_T + \sum_{i \neq T} k_i} \qquad \text{A3.3}$$

$$\tau_D = \frac{1}{\sum_{i \neq T} k_i} \qquad \text{A3.4}$$

With simple algebra, the FRET efficiency can then be expressed in the form of equation A3.1.

Tables

Table 2.1: Fitting results from multi-frequency lifetime measurements taken on the purified biosensor

	a_1	τ_1 (ns)	a_2	τ_2 (ns)	$\langle\tau\rangle$ (ns)
ECFP-FRET	0.92	0.42	0.08	3.99	0.71
ECFP	0.44	1.24	0.56	4.08	2.83

Supp. Table 2.2: Measurement of the FRET standard on the steady-state microscope

	Intensity
IDD	298.4 ± 61.1
IDA	1460.3 ± 186.4
IAA	1367.6 ± 158.1

Table 2.3: Bleedthrough Coefficient (b_1)

	b_1
Cell 1	0.3721
Cell 2	0.3448
Cell 3	0.3848
Cell 4	0.3401
Cell 5	0.3522
Cell 6	0.3468
Cell 7	0.3406
Cell 8	0.3608
Cell 9	0.3579
Cell 10	0.3505
Mean	0.35506
Std. Dev.	0.014341 87

Table 2.4 Analysis of the steady-state FRET efficiency and FRET ratio in the regions of interest in an HT-1080 cell transfected with the MT1-MMP biosensor

	Avg. FRET Eff.	**Uncert. in FRET Efficiency**	**Avg. FRET Ratio**	**Uncert. in FRET Ratio**
ROI 1	0.1784	0.1049	1.238	0.5034
ROI 2	0.1769	0.1218	1.244	0.5883
ROI 3	0.0231	0.2376	2.169	2.4753
ROI 4	0.0346	0.1688	2.071	1.6414

Table 2.5: The steady-state FRET efficiency and FRET ratio calculated in each of the regions of interest selected in an HT-1080 cell transfected with the MT1-MMP biosensor and treated with the MMP inhibitor GM6001.

	Avg. FRET Eff.	**Uncert. In FRET Efficiency**	**Avg. FRET Ratio**	**Uncert. In FRET Ratio**
ROI 1	0.2057	0.3393	1.1326	1.4584
ROI 2	0.2363	0.1065	1.0275	0.4076
ROI 3	0.2563	0.1191	0.9649	0.424
ROI 4	0.2729	0.2193	0.9162	0.7362

Figures

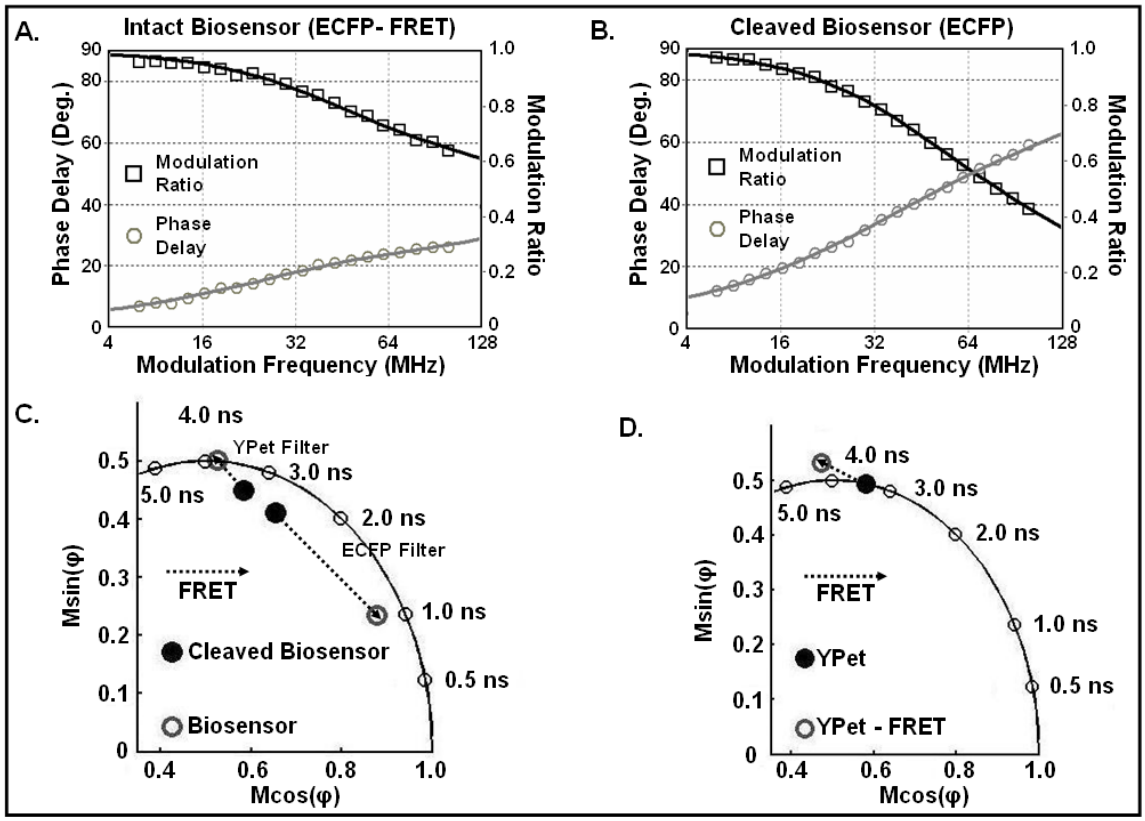

Figure 2.1: Measurements of the time-dependent fluorescence of purified biosensor: (A) The modulation ratio (black squares) and phase delay (gray circles) were collected from a sample of purified biosensor at a set of modulation frequencies sampled from 10MHz to 100MHz. The lines connecting the individual data points represent the results of iterative fitting required to extract information about the individual lifetime components in the sample (B) Following cleavage by trypsin, the phase delay (gray circles) and modulation ratio (black squares) were measured at the same modulation frequencies applied in (A). The rates of de-modulation and the shifts in phase delay observed as a function of frequency indicate a longer lifetime than the sample measured in (A). (C) The trajectories of the phase delay and modulation ratio of the MT1-MMP biosensor are presented before and after cleavage, visualized through the channels specific for ECFP and YPet as indicated. (D) The phase delay and modulation ratio of YPet on the MT1-MMP biosensor before (measured) and after (simulated assuming that only the fluorescence of the acceptor excited by FRET is observed – see text)) cleavage, detected through the YPet channel are projected on the polar plot.

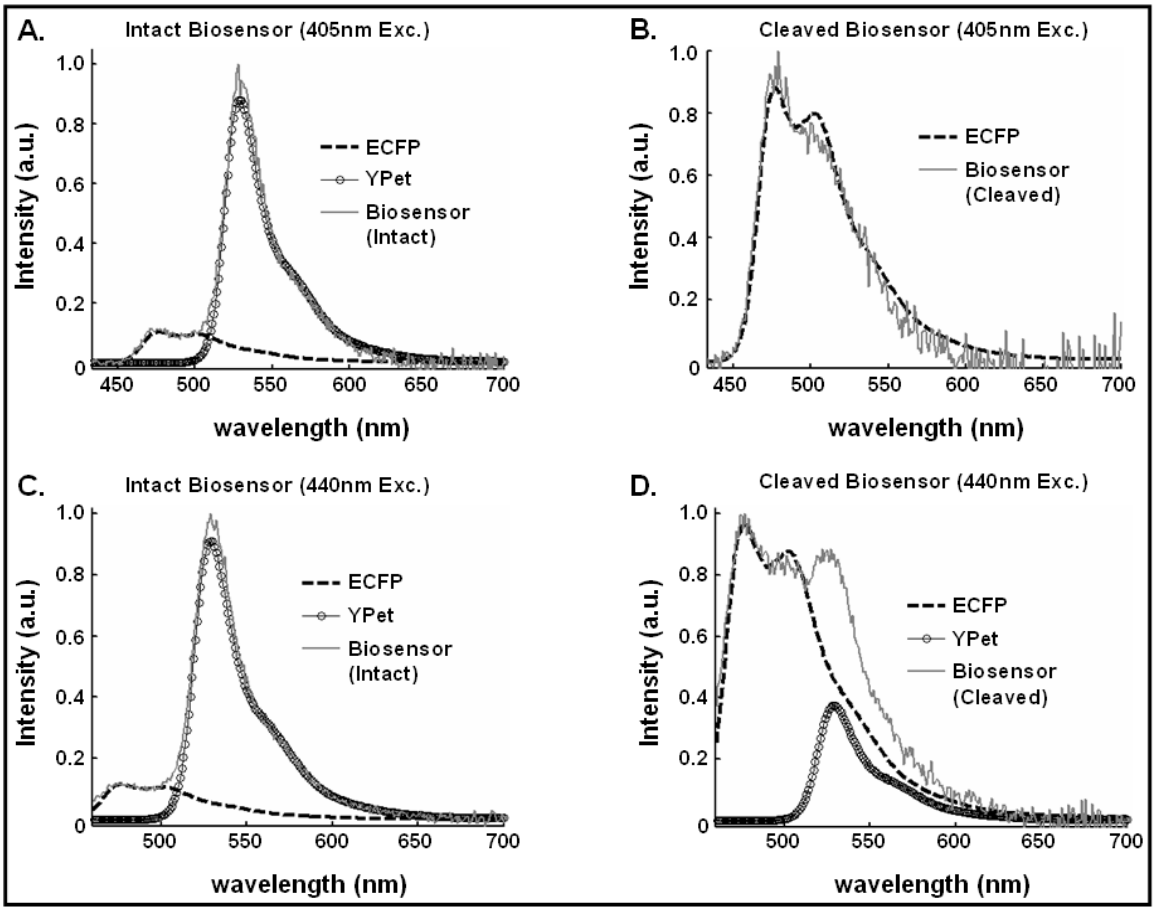

Figure 2.2: Steady-state emission spectra of a purified solution of MT1-MMP biosensors: (A) The fluorescence emission of the intact biosensor was recorded at an excitation wavelength of 405nm. The contributions of both ECFP and YPet were identified with spectral unmixing. (B) The emitted fluorescence from the cleaved biosensor excited at 405nm consists only of intensity from ECFP. (C) This emission spectrum of the intact MT1-MMP biosensor was collected at an excitation wavelength of 440nm which was also used in the lifetime imaging experiments. (D) With an excitation wavelength of 440nm, emission from the directly excited acceptor (YPet) is clearly visible following the spectral unmixing.

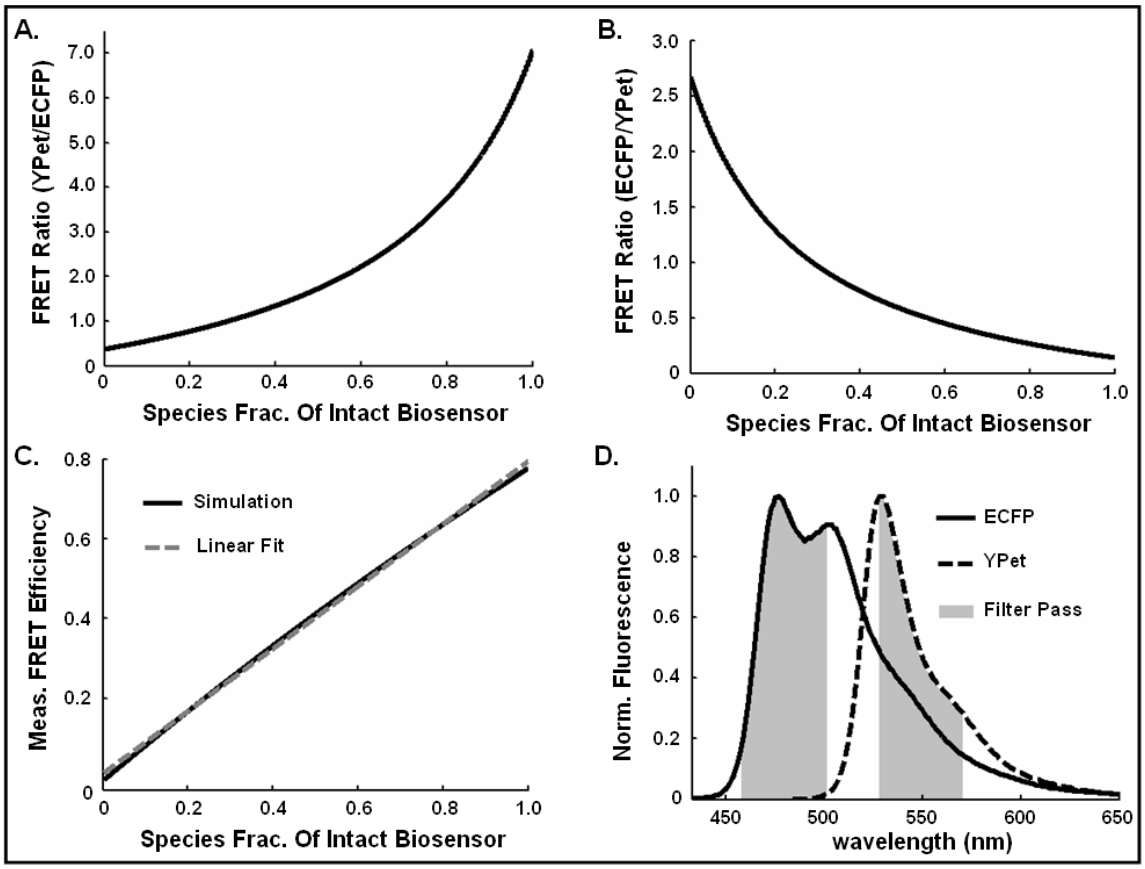

Figure 2.3: Simulations of the FRET ratio and FRET efficiency: (A) The FRET ratio (YPet/ECFP) was simulated using the emission wavelengths shown in (D) as a function of the normalized concentration of the intact biosensor. (B) The results of the simulation determining the FRET ratio (ECFP/YPet) for a large set of normalized concentrations of the intact biosensor are plotted. (C) The steady-state FRET efficiency was calculated also as a function of the normalized concentration of the intact biosensor (black line). The simulated points were fitted to a straight line (dashed gray line). (D) The two sets of emission wavelengths (gray areas in plot) used both in these simulations and later in the steady-state measurements taken on live cells are shown along with the normalized emission spectra of ECFP and YPet.

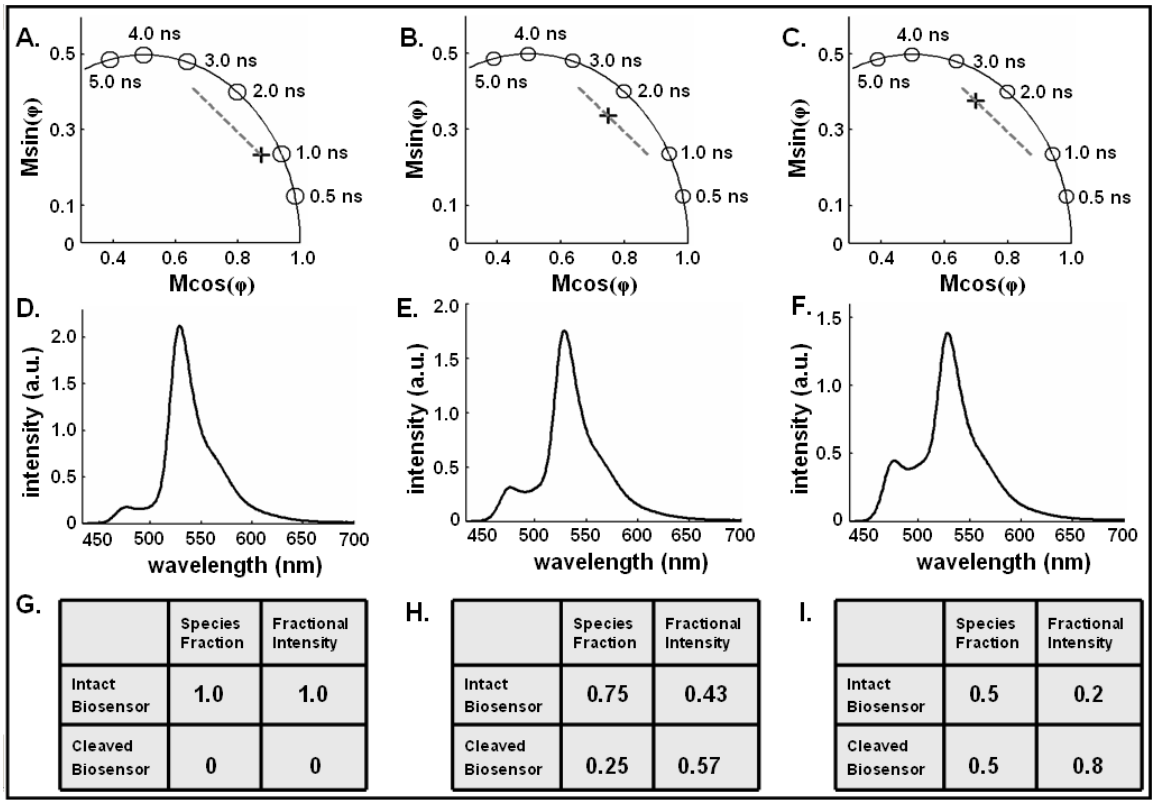

	Species Fraction	Fractional Intensity
Intact Biosensor	1.0	1.0
Cleaved Biosensor	0	0

	Species Fraction	Fractional Intensity
Intact Biosensor	0.75	0.43
Cleaved Biosensor	0.25	0.57

	Species Fraction	Fractional Intensity
Intact Biosensor	0.5	0.2
Cleaved Biosensor	0.5	0.8

Figure 2.4: Time–dependent simulations of the biosensor in-vitro: (A-C) At a modulation frequency of 40MHz, three polar plots were simulated with a filter specific for ECFP's emission at three species fractions of the intact biosensor (1.0 (A), 0.75 (B) and 0.5 (C)). The simulated point plotted as a black cross is shown along with a dotted gray line that indicates the set of locations on the polar plot where all linear combinations of the intact and cleaved biosensors exist. (D-F) The emission spectra of the biosensor corresponding to the species fractions of the intact biosensor of 1.0 (D), 0.75 (E) and 0.5 (F) are shown. When the spectra in (E) and (F) are compared, there is a significant change in the FRET ratio that corresponds to a very slight change in polar coordinate as shown on the corresponding plot plots. (G-I) Tables are presented indicating the normalized concentration of the intact biosensor (species fraction) and the fractional contribution to the steady-state intensity for each state of the biosensor examined in these simulations.

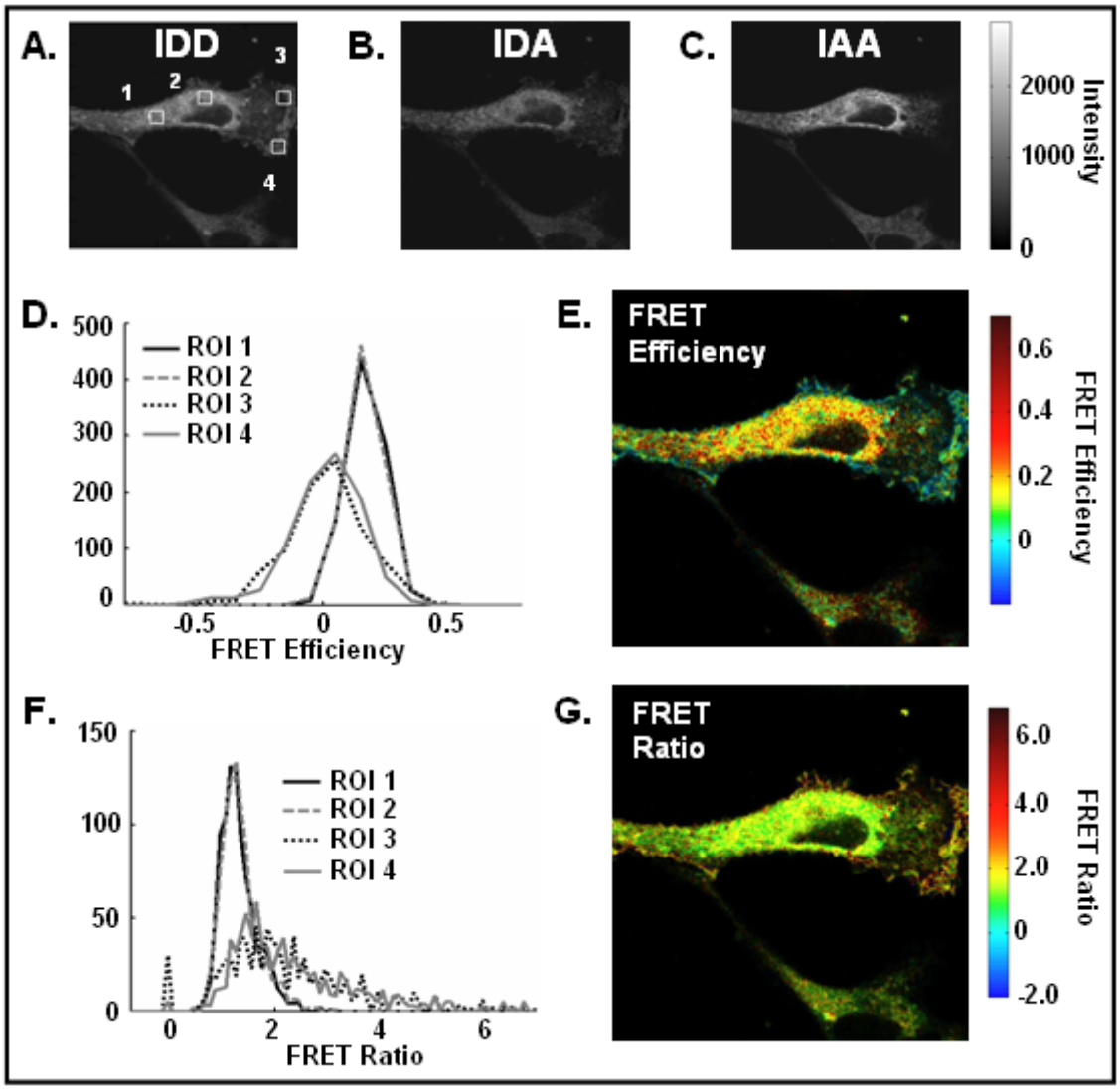

Figure 2.5: Steady-state FRET measurement of an HT-1080 cell transfected with the MT1-MMP biosensor: (A) An intensity image collected through the channel IDD (Exc. 405nm, Em. {458nm – 501nm}) of an HT-1080 cell transfected with the MT1-MMP biosensor is shown. (B) An intensity image of the same cell from (A) is displayed having been imaged with the channel IDA (Exc. 405nm, Em. {528nm – 570nm}). (C) This intensity image of the HT-1080 cell was collected while exciting only the YPet in the cell through the channel IAA (Exc. 514nm, Em. {528nm – 570nm}). There is a definite area of the cell on the right edge where there is no YPet present indicating that the biosensor is cleaved. (D). On a pixel-wise basis, the FRET efficiency in the four regions of interest shown in (A) are plotted in this histogram. (E) A color rendering displaying the steady-state FRET efficiency computed at each pixel of the cell's image is shown. (F) This histogram displayed the values of the FRET ratio (ECFP/YPet) determined at each pixel within the four regions of interest in (A). (G) This image displays the FRET ratio (ECFP/YPet) determined throughout the entire image of the cell.

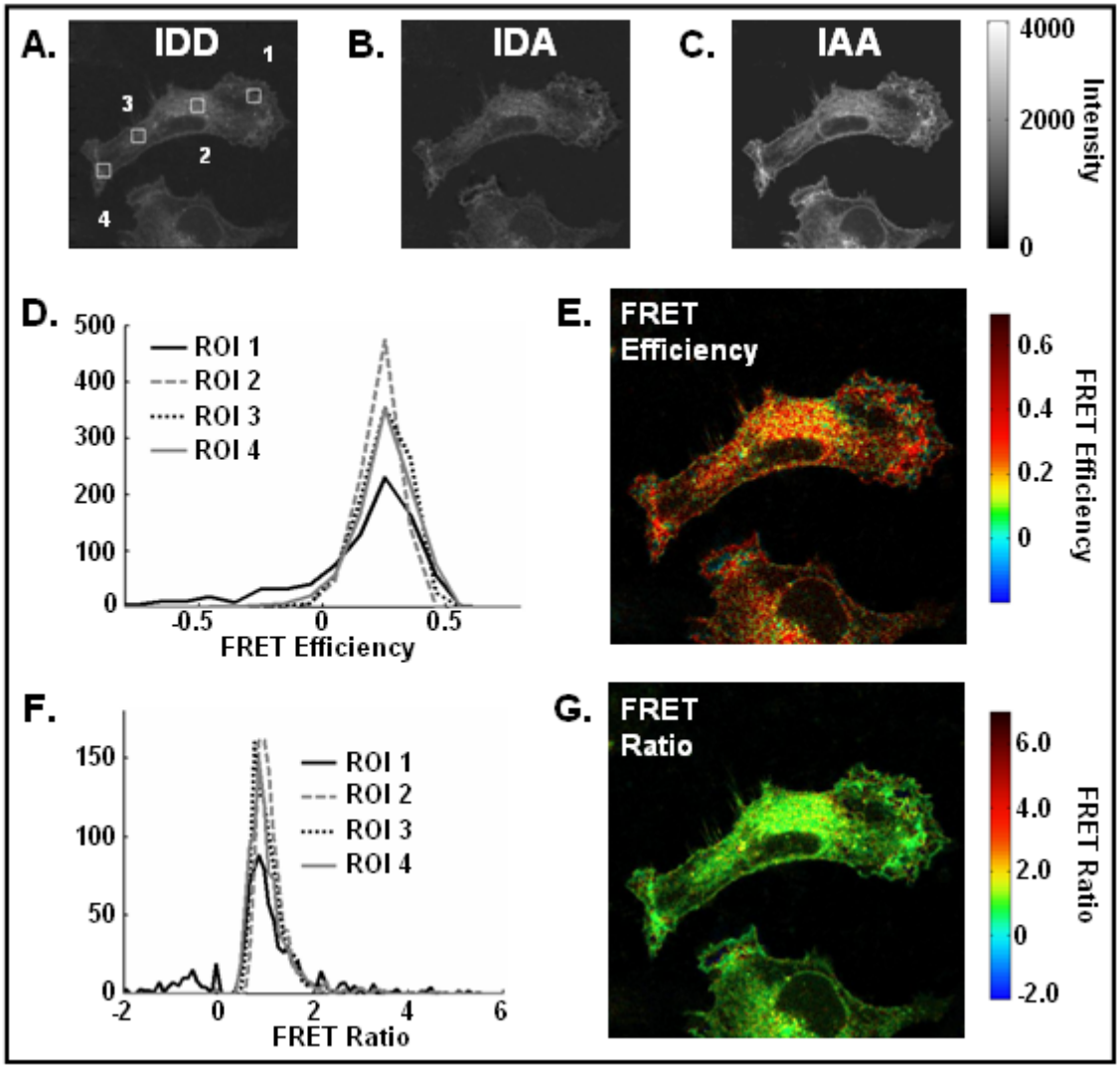

Figure 2.6: Steady-state measurement of FRET taken on transfected HT-1080 cells pre-treated with the MMP inhibitor GM6001. (A) This steady-state intensity image of an HT-1080 cell transfected with the MT1-MMP biosensor and pre-treated with the MMP inhibitor GM6001 was collected through the channel IDD (Exc. 405nm, Em. {458nm – 501nm}). (B) An intensity of the same cell in (A) is presented collected using the channel IDA (Exc. 405nm, Em. {528nm – 570nm}) (C) This intensity image of the HT-1080 cell was generated with only the fluorescence emission of the YPet by imaging the cell with the channel IAA (Exc. 514nm, Em. {528nm – 570nm}). (D) In every pixel of the four regions of interest highlighted in (A), the steady-state FRET efficiency was computed and the resulting values are presented in the histogram. (E) The steady-state FRET efficiency determined in a pixel-wise manner is mapped in color throughout the cell's image. (F) In each of the pixels in the regions of interest shown in (A), the FRET ratio (ECFP/YPet) was calculated and is plotted as a histogram. (G) A color mapping of the FRET ratio (ECFP/YPet) is shown

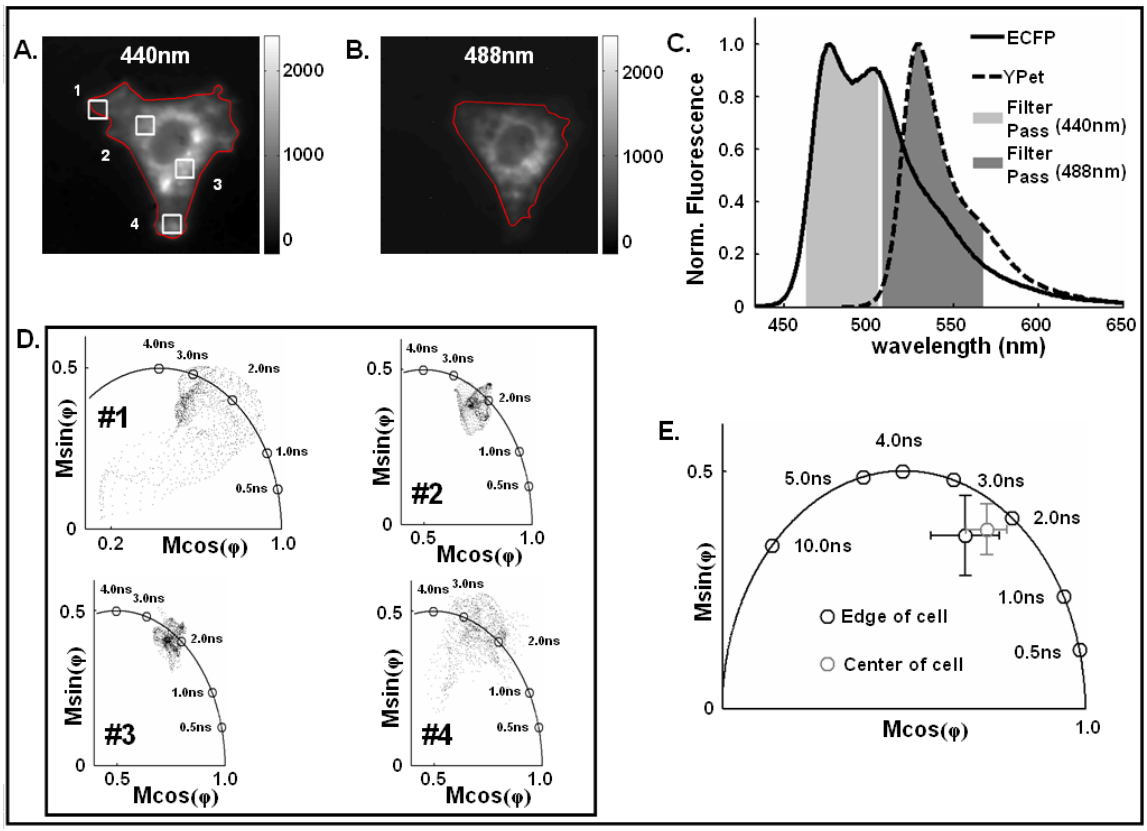

Figure 2.7: Images collected with FLIM of HT-1080 cells transfected with the MT1-MMP biosensor. (A) This intensity image was collected at an excitation wavelength of 440nm through the filter shown in (C) specific for ECFP. (B) This image of the HT-1080 was collected with the fluorescence of YPet by exciting the sample with a 488nm laser. The images shown in (A) and (B) represent the average intensity of the eight phase images collected to generate the FLIM image. (C) The two sets of emission wavelengths (gray shading) used to image the cell with the 440nm and 488nm laser are presented with the normalized emission spectra of ECFP and YPet. (D) The polar coordinates of the pixels within the regions of interest highlighted in (A) are projected on the presented polar plots. (E) The average polar coordinate of the central portion of the cell (area highlighted in red in (B)) and the edge of the cell (difference in area between the two areas highlighted in red in (A) and (B)) are plotted with their corresponding standard deviations in x and y.

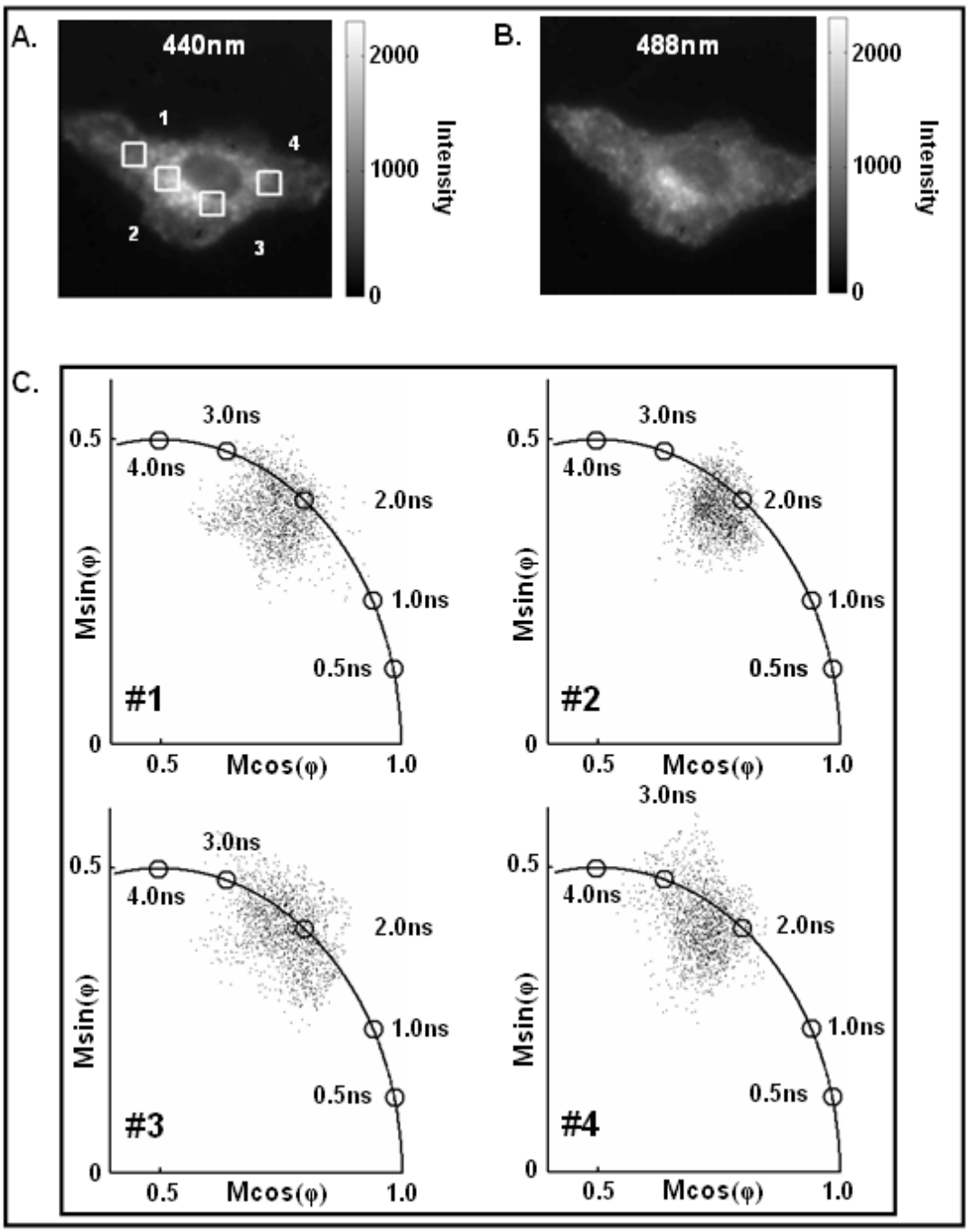

Figure 2.8: HT-1080 cell transfected with the MT1-MMP biosensor, treated with GM6001 and imaged with FLIM: (A) An intensity image of the HT-1080 cell is shown having been excited by the 440nm laser and imaged through a filter specific for ECFP's fluorescence. (B) The same cell from (A) was imaged while being excited with a 488nm laser through the emission filter specific for YPet shown in the darker gray area in Fig. 5C. (C) The polar coordinates from each pixel within the regions of interest highlighted in (A) are projected on the polar plots #1-4.

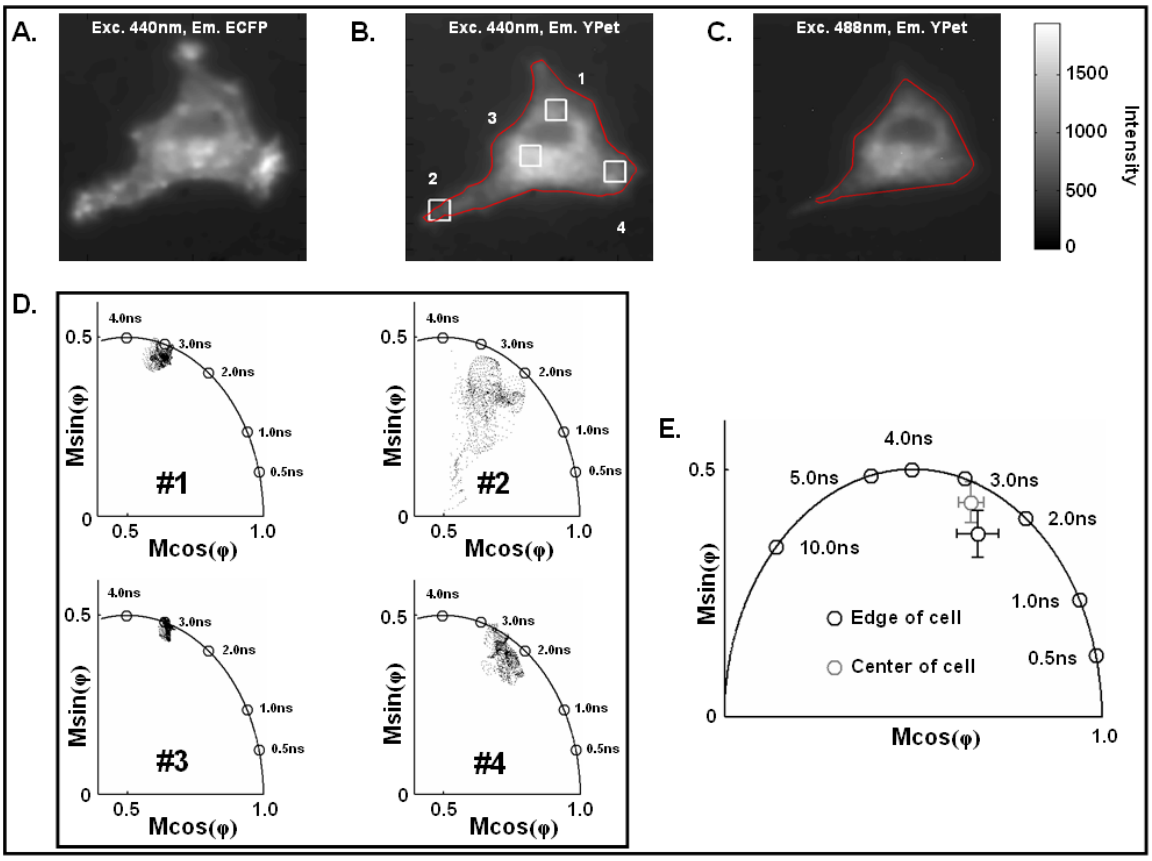

Figure 2.9: Time-dependent fluorescence of the acceptor detected in a live HT-1080 cell transfected with the MT1-MMP biosensor: (A) This intensity image was collected with the emission of the ECFP by averaging the eight phase images collected during the FLIM experiment. (B) By exciting with the 440nm laser and collecting the fluorescence through a filter near the emission peak of YPet, this intensity image likely contains contributions from ECFP's emission, emission from directly excited YPet and the sensitized emission of YPet. (C) The spatial distribution of YPet is indicated in this intensity image which was collected by exciting the cell with a 488nm laser. (D) The pixels from the four regions on interests in (B) are projected as polar coordinates on these scatter plots. (E) The average polar coordinate calculated from the pixels in the center and edge of the cell are shown on this plot along with the corresponding uncertainties in x and y. The center of the cell is the area within the red boundary plotted in (C). The edge of the cell is defined as the area located between the red boundaries plotted in (B) and (C).

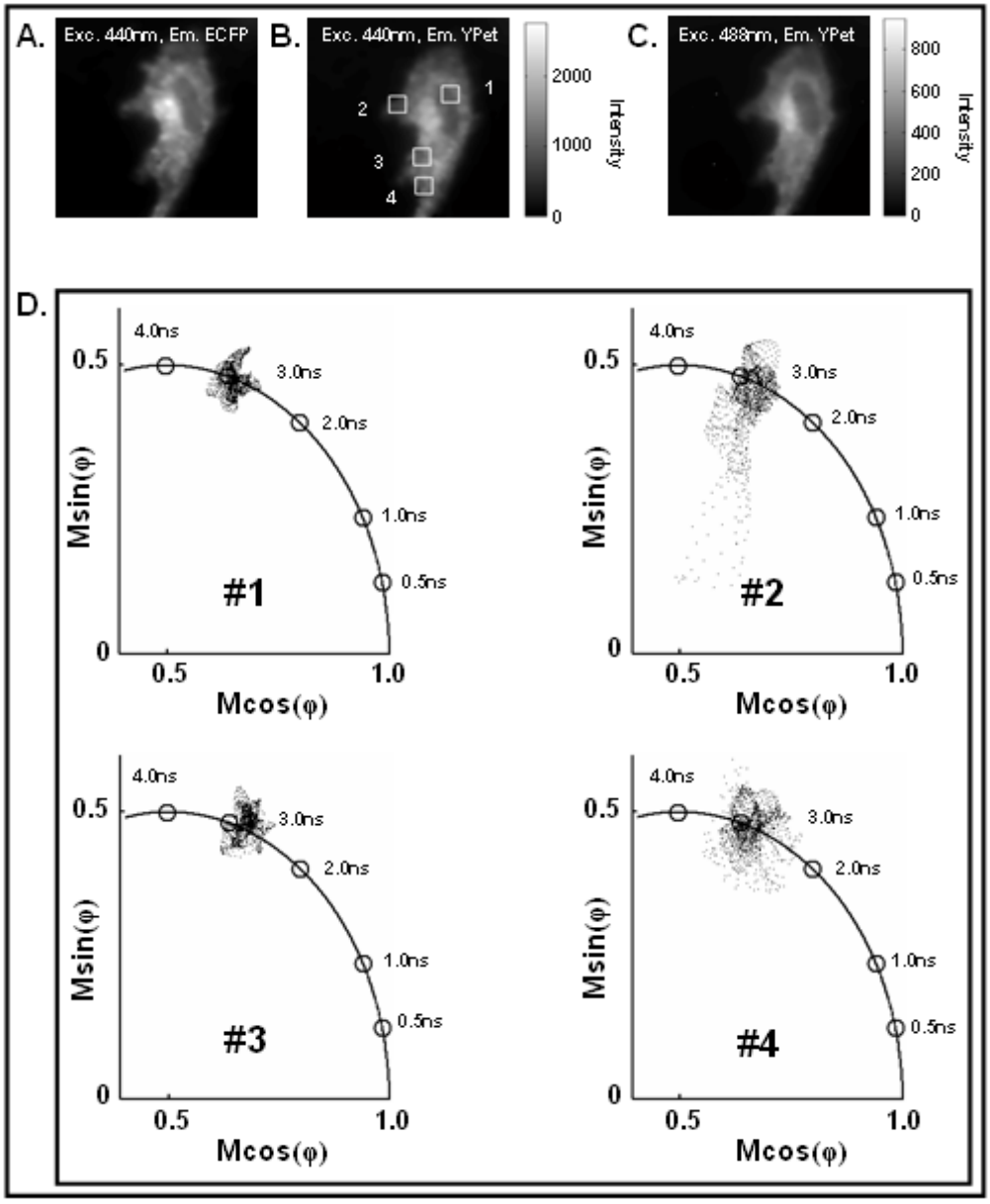

Figure 2.10: A live HT-1080 cell transfected with the MT1-MMP biosensor, pre-treated with the MMP inhibitor GM6001 and imaged with FLIM using the fluorescence of the acceptor: (A) The emitted fluorescence of the ECFP was collected after averaging the eight phase images acquired during the acquisition of the lifetime image. (B) This image was taken by exciting the sample at 440nm and recording the fluorescence near the emission peak of YPet. (C) By exciting and collecting fluorescence only from the YPet, this image indicates that there is good co-localization between the YPet and ECFP in this cell. (D) The polar coordinates corresponding to the pixels in the regions of interest highlight in (B) are projected on these polar plots.

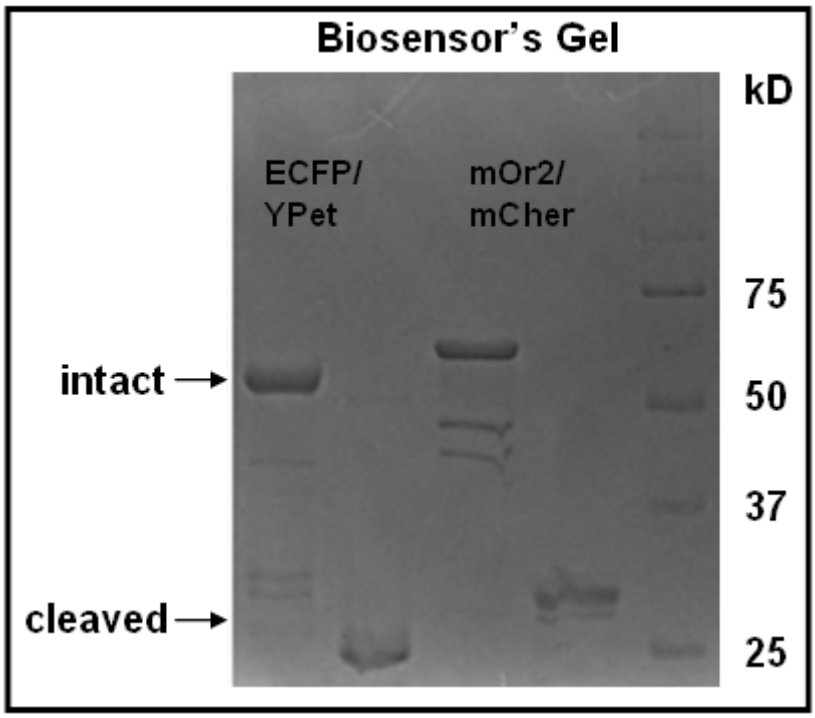

Supplemental Figure 2.1: Polyacrylamide gel: Both the ECFP/YPet and mOrange2/mCherry variant of the MT1-MMP biosensor were analyzed before and after the biosensor's substrate was cleaved by trypsin. In both cases, the mass of the biosensor were reduced by approximately a factor of one half following the addition of trypsin. The initial masses of the intact biosensor were however both near 60kD with no unpaired constituents apparent in the gel.

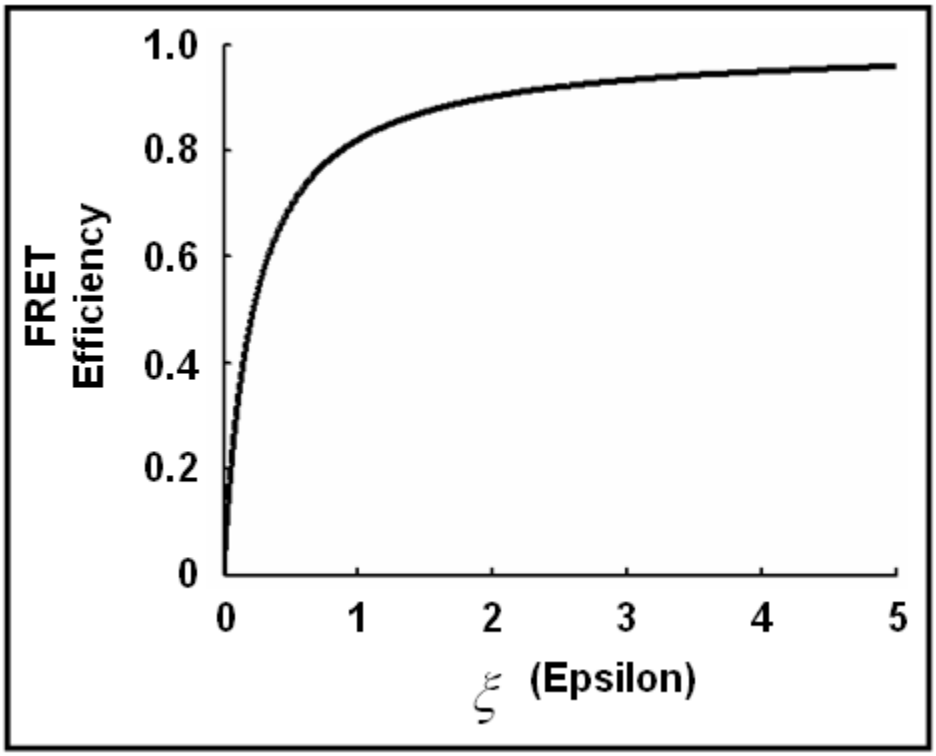

Supplemental Figure 2.2: Correcting the measured (ξ): The measured intensities from the FRET standard (solution) were used to plot the FRET efficiency as a function of (ξ). By knowing the actual FRET efficiency of the sample, a corrected value of (ξ) can be determined.

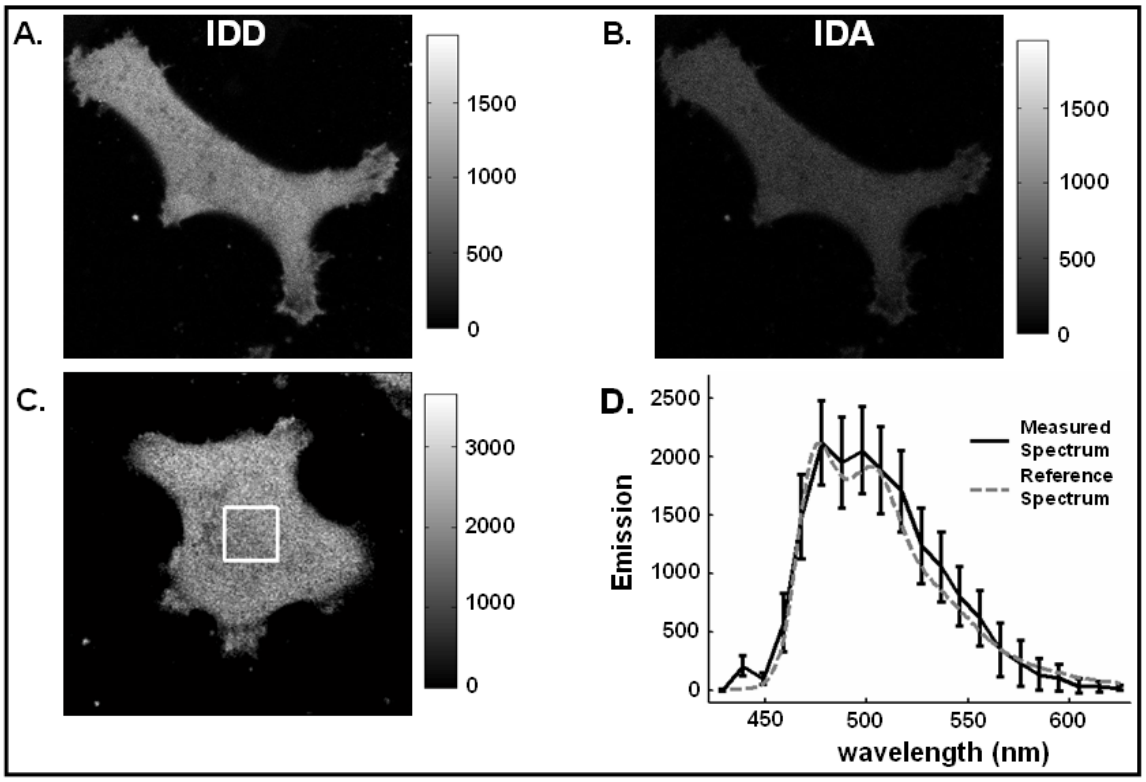

Supplemental Figure 2.3: Determining the bleedthrough coefficient (b_1): (A) A steady-state intensity image of an HT-1080 cell transfected with a ECFP-only plasmid was collected through the channel IDD (Exc. 405nm, Em. {458nm – 501nm}). Unlike the staining of the MT1-MMP biosensor, the staining from this plasmid does not reveal any apparent organelles in the cell. (B) An intensity image of the same HT-1080 cell from (A) is shown having been imaged through the channel IDA (Exc. 405nm, Em. {528nm – 570nm}). (C) This intensity image of the HT-1080 cell was taken from a set of spectral images examining the transfection of the ECFP-only plasmid with an excitation wavelength of 405nm. (D) The intensities and corresponding standard deviations collected from the region of interest highlighted in (C) are plotted as a function of wavelength (dark black line). The reference spectrum of pure ECFP (Tsien Lab [37]) is also shown (dashed gray line).

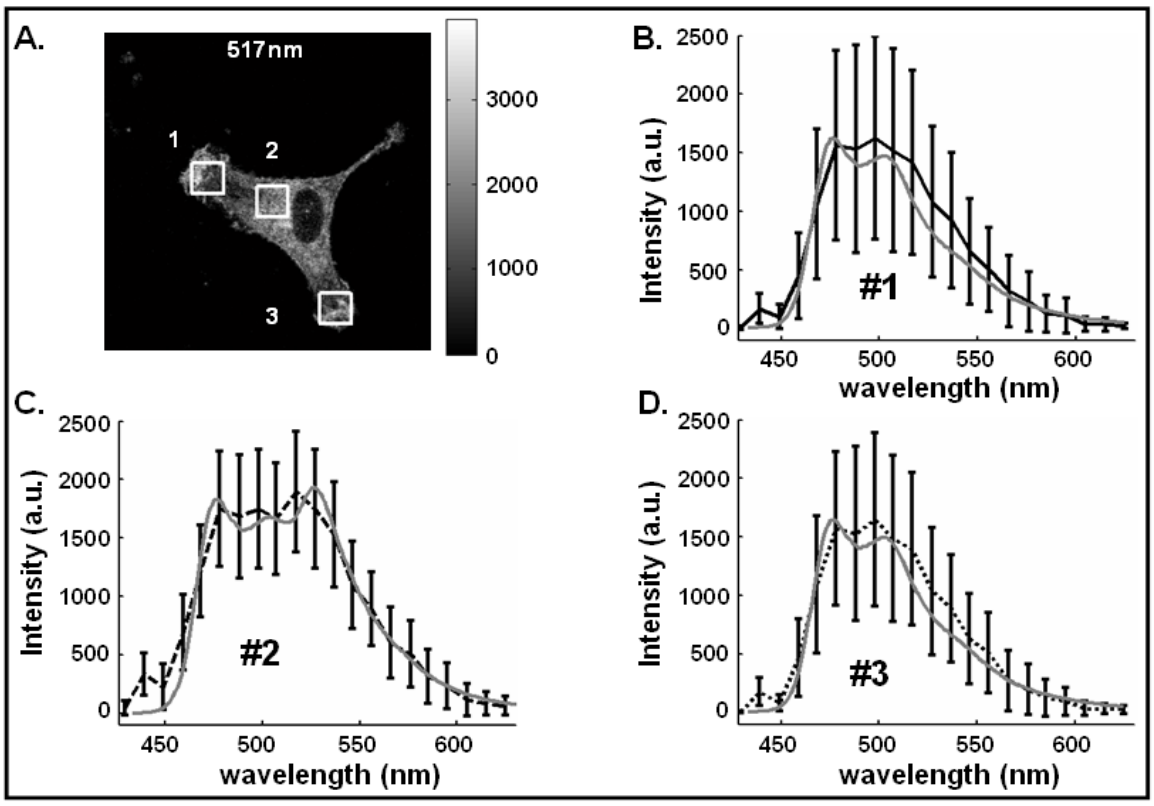

Supplemental Figure 2.4: Steady-state spectra collected from an HT-1080 cell transfected with the MT1-MMP biosensor (1): (A) An intensity image taken with an excitation wavelength of 405nm and an emission wavelength of 517nm ±9.8nm is displayed with three regions of interest highlighted. (B) The intensities from the first region of interest are plotted as a function of wavelength. A reference spectrum of pure ECFP is plotted in light gray. (C) In region #2 located near the nucleus of the cell, the emission spectrum plotted as a dashed black line contained a contribution from YPet near 530nm. The emission spectrum derived from a simulated combination of cleaved and intact biosensors is presented in light gray. (D) The emission spectrum from region #3 is plotted as a dotted black line accompanied by a reference spectrum of pure ECFP (gray line).

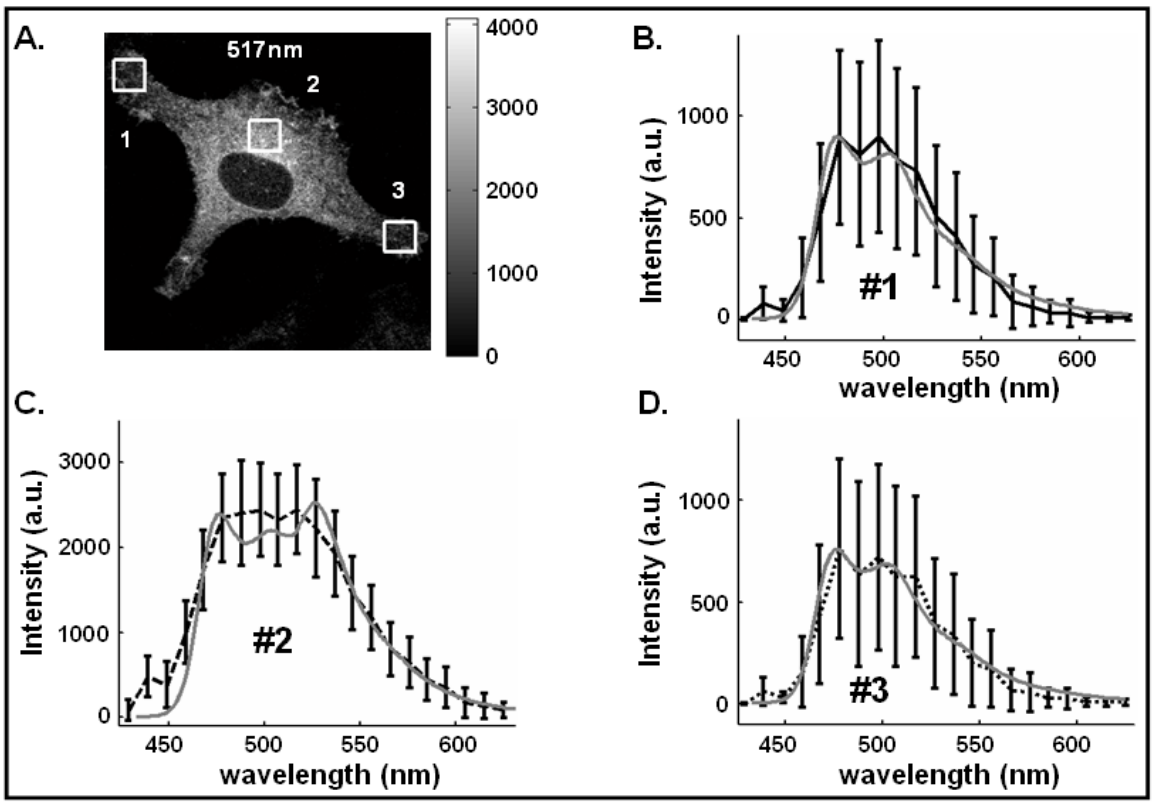

Supplemental Figure 2.5: Spectral imaging of an HT-1080 cell transfected with the MT1-MMP biosensor (2): (A) This intensity image describing an HT-1080 cell transfected with the MT1-MMP biosensor was collected with a 405nm exciting laser and a bandpass of emission wavelengths equal to 517nm ± 9.8nm. (B) In region #1, the recorded spectrum (black line) closely followed the intensity profile of the pure ECFP (gray line). (C) Some fluorescence from YPet is apparent near 530nm in the emission spectrum from region #2 (dashed black line). As a reference, a simulated spectrum corresponding to a combination of cleaved and intact biosensor is presented (gray line). (D) The emission spectrum taken from region #3 (dotted black line) matched the reference spectrum of pure ECFP (gray line) very closely.

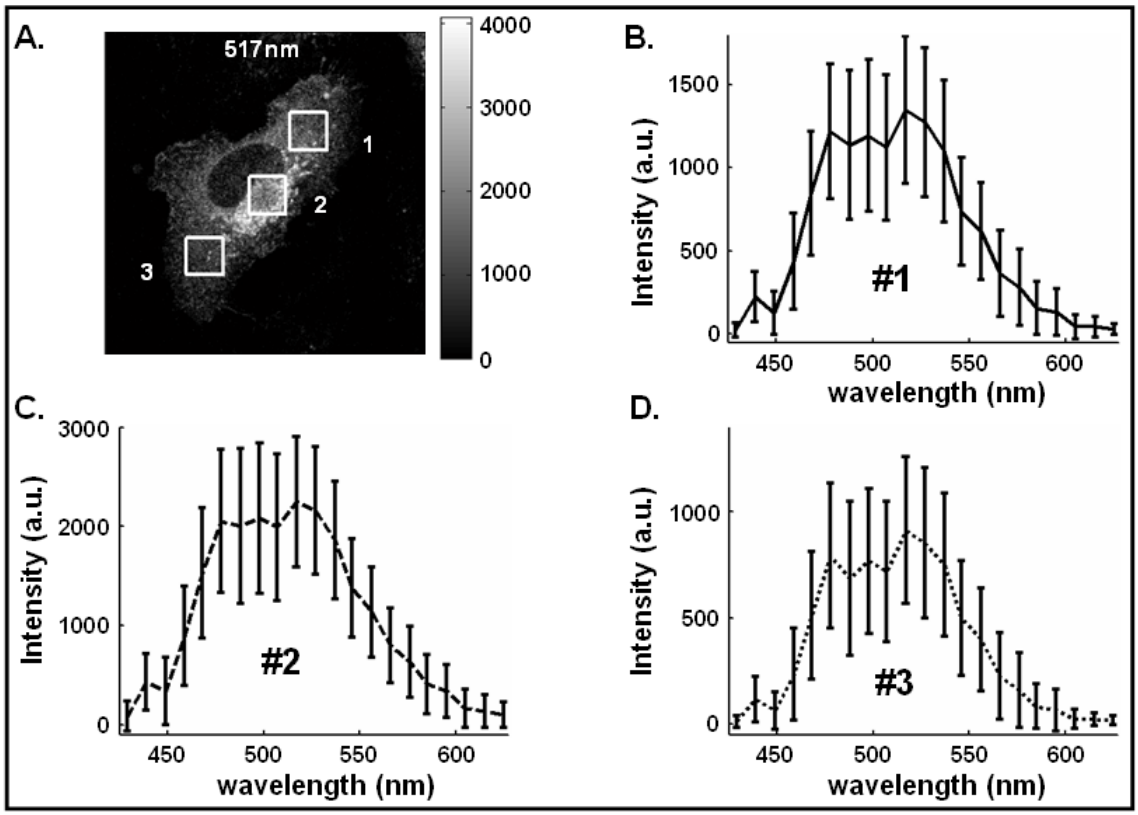

Supplemental Figure 2.6: Spectral measurements of HT-1080 cells pre-treated with GM6001: (A) An intensity image an HT-1080 cell imaged with a spectral detector at an emission wavelength of 517nm ± 9.8nm is displayed with several regions of interest shown in white. (B-D) The average intensities and corresponding standard deviations (error bars) from each of the regions #1-3 shown in (A) are plotted as a function of wavelength. The first emission peak from the emission spectrum of ECFP is approximately at 478nm and the emission peak from YPet is at 530nm.

References

1. A. Miyawaki and R.Y. Tsien, (2000), Monitoring protein conformations and interactions by fluorescence resonance energy transfer between mutants of green fluorescent protein. Methods Enzymol. **327**. 472-500.
2. R.M. Clegg, T.W.J. Gadella Jr., and T.M. Jovin, (1994), Lifetime-Resolved Fluorescence Imaging. SPIE. **2137**. 105-118.
3. T.W.J. Gadella Jr., T.M. Jovin, and R.M. Clegg, (1993), Fluorescence lifetime imaging micorscopy (FLIM): Spatial resolution of microstructures on the nanosecond time scale. Biophysical Chemistry. **48**. 221-239.
4. J.R. Lakowicz and K.W. Berndt, (1991), Lifetime-selective fluorescence imaging using an rf phase-sensitive camera. Reviews of Scientific Instrumentation. **62**(7). 1727-1734.
5. P. Schneider and R.M. Clegg, (1997), Rapid acquisition, analysis and display of fluorescence lifetime-resolved images for real-time applications. Reviews of Scientific Instrumentation. **68**(11). 4107-4119.
6. J.P. Eichorst, et al., Phase differential enhancement of FLIM to distinguish FRET components of a biosensor for monitoring molecular activity of Membrane Type 1 Matrix Metalloproteinase in live cells. J Fluoresc. **21**(4). 1763-77.
7. M. Ouyang, et al., Simultaneous Visualization of Protumorigenic Src and MT1-MMP Activities with Fluorescence Resonance Energy Transfer. Cancer Res. **70**(6). 2204-2212.

8. F.J. van Kuppeveld, et al., (2002), Homomultimerization of the coxsackievirus 2B protein in living cells visualized by fluorescence resonance energy transfer microscopy. J Virol. **76**(18). 9446-56.

9. S. Kwok, et al., (2008), Genetically encoded probe for fluorescence lifetime imaging of CaMKII activity. Biochem Biophys Res Commun. **369**(2). 519-25.

10. P. Kalab and A. Pralle, (2008), Chapter 21: Quantitative fluorescence lifetime imaging in cells as a tool to design computational models of ran-regulated reaction networks. Methods Cell Biol. **89**. 541-68.

11. A. Miyawaki, Development of probes for cellular functions using fluorescent proteins and fluorescence resonance energy transfer. Annu Rev Biochem. **80**. 357-73.

12. R. Laine, et al., Fluorescence lifetime readouts of Troponin-C-based calcium FRET sensors: a quantitative comparison of CFP and mTFP1 as donor fluorophores. PLoS One. **7**(11). e49200.

13. R.M. Clegg, (1992), Fluorescence resonance energy transfer and nucleic acids. Methods Enzymol. **211**. 353-88.

14. T. Förster (1951) *Fluoreszenz Organischer Verbindungen*, Vandenhoek & Ruprecht, Göttingen, Germany.

15. T. Förster, (1948), Zwischenmolekulare Energiewanderung und Fluoreszenz. Annalen der Physik. **437**(2). 55-75.

16. T. Förster, (1948), Intermolecular energy migration and fluroescence. Ann. Phys.. **2**. 55-75.

17. J. Szollosi, et al., (1984), Fluorescence energy transfer measurements on cell surfaces: a critical comparison of steady-state fluorimetric and flow cytometric methods. Cytometry. **5**(2). 210-6.

18. L. Tron, et al., (1984), Flow cytometric measurement of fluorescence resonance energy transfer on cell surfaces. Quantitative evaluation of the transfer efficiency on a cell-by-cell basis. Biophys J. **45**(5). 939-46.

19. T.a.A.-J. Jovin, Donna, *FRET Microscopy: Digital Imaging of Fluorescence Resonance Energy Transfer. Application in Cell Biology*, in *Cell Structure and Function by Microspectrofluorometry*, E.a.H. Kohen, Joseph, Editor. 1989, Academic Press: San Diego, California. p. 99-115.

20. J. Szollosi, et al., (1987), Flow cytometric resonance energy transfer measurements support the association of a 95-kDa peptide termed T27 with the 55-kDa Tac peptide. Proc Natl Acad Sci U S A. **84**(20). 7246-50.

21. J. Lakowicz (2006) *Principles of Fluorescence Spectroscopy*, Springer, New York, NY. 954.

22. T. Zal and N.R. Gascoigne, (2004), Photobleaching-corrected FRET efficiency imaging of live cells. Biophys J. **86**(6). 3923-39.

23. H. Chen, et al., (2006), Measurement of FRET efficiency and ratio of donor to acceptor concentration in living cells. Biophys J. **91**(5). L39-41.

24. P. Nagy, et al., (2005), Novel calibration method for flow cytometric fluorescence resonance energy transfer measurements between visible fluorescent proteins. Cytometry A. **67**(2). 86-96.

25. A. Hoppe, K. Christensen, and J.A. Swanson, (2002), Fluorescence resonance energy transfer-based stoichiometry in living cells. Biophys J. **83**(6). 3652-64.

26. J. Wlodarczyk, et al., (2008), Analysis of FRET signals in the presence of free donors and acceptors. Biophys J. **94**(3). 986-1000.

27. B. Valeur (2002) *Molecular Fluorescence: Principles and Applications*, WILEY-VCH, Weinheim, Germany.

28. Y.-C. Chen, et al. (2010) *General Concerns of FLIM Data Representation and Analysis: Frequency-Domain Model-Free Analysis*, FLIM Microscopy in Biology and Medicine, ed. A. Periasamy and R.M. Clegg, Chapman & Hall/CRC, New York. 291-335.

29. J.R. Lakowicz and A. Balter, (1982), Theory of phase-modulation fluorescence spectroscopy for excited-state processes. Biophys Chem. **16**(2). 99-115.

30. J.R. Lakowicz and A. Balter, (1982), Analysis of excited-state processes by phase-modulation fluorescence spectroscopy. Biophys Chem. **16**(2). 117-32.

31. B.Q. Spring and R.M. Clegg, (2009), Image analysis for denoising full-field frequency-domain fluorescence lifetime images. J Microsc. **235**(2). 221-37.

32. B.Q. Spring and R.M. Clegg (2010) *Frequency-Domain FLIM*, FLIM Microscopy in Biology and Medicine, Chapman & Hall/CRC, New York. 115-142.

33. S.G. Mallat, (1989), A Theory fo Multiresolution Signal Decomposition: The Wavelet Representation. IEEE Transactions on Pattern Analysis and Machine Intelligence. **11**(7). 674-692.

34. C. Buranachai, et al., (2008), Rapid frequency-domain FLIM spinning disk confocal microscope: lifetime resolution, image improvement and wavelet analysis. J Fluoresc. **18**(5). 929-42.

35. G. Patterson, R.N. Day, and D. Piston, (2001), Fluorescent protein spectra. J Cell Sci. **114**(Pt 5). 837-8.

36. A.W. Nguyen and P.S. Daugherty, (2005), Evolutionary optimization of fluorescent proteins for intracellular FRET. Nat Biotechnol. **23**(3). 355-60.

37. http://www.tsienlab.ucsd.edu/Documents.htm.

38. M. Jose, et al., (2007), Photophysics of Clomeleon by FLIM: discriminating excited state reactions along neuronal development. Biophys J. **92**(6). 2237-54.

39. M.A. Elsliger, et al., (1999), Structural and spectral response of green fluorescent protein variants to changes in pH. Biochemistry. **38**(17). 5296-301.

40. J.W. Borst, et al., ATP changes the fluorescence lifetime of cyan fluorescent protein via an interaction with His148. PLoS One. **5**(11). e13862.

41. M.A. Rizzo, et al., (2004), An improved cyan fluorescent protein variant useful for FRET. Nat Biotechnol. **22**(4). 445-9.

42. N.C. Shaner, et al., (2008), Improving the photostability of bright monomeric orange and red fluorescent proteins. Nat Methods. **5**(6). 545-51.

43. J.P. Eichorst, R.M. Clegg, and Y. Wang, (2012), Red-Shifted Fluorescent Proteins to Monitor Enzymatic Activity in Live HT-1080 Cells with Fluorescence Lifetime Imaging Microscopy (FLIM). Journal of Microscopy. **Submitted**.

44. V. Kolossov, et al., (2008), Engineering redox-sensitive linkers for genetically encoded FRET-based biosensors. Experimental Biology and Medicine. **233**(2). 238-248.

Chapter 3

The Long Wavelength Variant of the MT1-MMP Biosensor

Abstract

In this chapter, the MT1-MMP biosensor was modified to contain the mOrange2 and mCherry fluorescent proteins. These fluorescent proteins are monomeric variants of the red fluorescent protein found in the luminescent choral Discosoma sp. The change in the FRET ratio (amplitude of the donor's emitted intensity divided by the emission of the acceptor) between the intact and cleaved configuration of the biosensor is significantly smaller than the corresponding change observed with the cyan and yellow fluorescent proteins discussed in the previous chapter. The apparent difference in FRET is primarily the result of the low quantum yield of the mCherry which is nearly one third of the quantum yield of YPet. However, only the extinction coefficient of the acceptor and the set of wavelengths that it can absorb principally dictate the FRET efficiency with respect to the acceptor. Experimentally, the lifetime measured on the intact biosensor and separately on the cleaved biosensor with the mOrange2 and mCherry proteins translated into two polar coordinates, sufficiently separated for classifying the biosensor's configuration in images. As a result, with these fluorescent proteins which absorb and emit at wavelengths longer than 550nm, the activity of MT1-MMP was observed with lifetime imaging in live cancer cells undergoing dynamics in matrices of collagen-I. As stated previously, the matrices of collagen-I were intended to simulate the extra-cellular matrix (ECM) that metastatic cancer cells initially confront after leaving a tumor. The presented results indicate that MT1-MMP's role in the formation of protrusions that emerge from the cell's body to explore the local environment is quite complex. In some

cases, MT1-MMP is not required in the formation of protrusions while in other cases, the activation of MT1-MMP is not precisely correlated with the extension of protrusive structures from the cell. The protrusions formed during these experiments in matrices of collagen are the ideal places from which to study how metastatic cancer cells examine and translate information about the local environment into cues directing their behavior.

Introduction

When applied to study the MT1-MMP biosensor in live cells with FLIM, the contrast provided by the cyan and yellow fluorescent proteins was too poor to accurately monitor the activity of MT1-MMP [1]. Even though the steady-state techniques were able to resolve different extents of FRET in live cells, the susceptibility of the cyan and yellow proteins to environmental perturbations that can significantly change the FRET efficiency make them a completely unreliable system to study the activity of MT1-MMP [2-5].

The incorporation of the mOrange2 and mCherry fluorescent proteins into the MT1-MMP biosensor improved the contrast and the reliability in the detection of the biosensor in live cells [6-8]. Unlike the previous study of the MT1-MMP biosensor containing the ECFP/YPet fluorescent proteins with FLIM, both configurations of the biosensor were clearly resolvable in the same cell. The locations on the polar plot indicative of each configuration of the biosensor were stable, far apart and not substantially perturbed by changes in local environment. Furthermore, configurational changes in the mOrange2/mCherry MT1-MMP biosensor could be accurately followed in time following the removal of the MMP inhibitor GM6001.

The newly developed long wavelength fluorescent proteins which can be excited and emit light at wavelengths greater than 550nm, offer advantages for live cell imaging. For example, longer wavelengths mean that images of cells can be collected without the contribution of auto-fluorescence typically encountered with the cyan and yellow fluorescent proteins. In addition, live cells and tissues are also not as readily damaged by these longer excitation wavelengths. From the perspective of FRET, the overlap integral that partly determines efficiency of energy transfer has a dependency on the wavelength range being applied. This increase in overlap inherent to the longer wavelengths results typically, in higher Förster distances [9-13]. Hence, longer wavelengths intrinsically can improve the sensitivity in the detection of the biosensor by providing larger changes in FRET efficiency at greater separation distances between the donor and acceptor.

With the mOrange2/mCherry MT1-MMP biosensor, considerable work was undertaken to improve the temporal resolution of the FLIM system. Ultimately, the goal of these efforts was to more carefully visualize the configurational changes in the biosensor following the removal of MMP inhibitors. As discussed previously, lifetime images can be acquired at high speed (near video rates) but only with sufficient signal-to-noise, which is not often available when studying live cells. Furthermore, regardless of the brightness of the sample or the sensitivity of the imaging system, the temporal resolution of FLIM is also degraded because multiple exposures of the sample are necessary to generate a single lifetime image. On our FLIM system for example, more than twenty individual image acquisitions are required to generate a single lifetime image [14-16]. With laser excitation, only a few lifetime images can be acquired of the transfected HT-1080 cells before the cell's health rapidly degrades. As a result, a variant

of FLIM called phase suppression was incorporated into both the instrument control as well as in the image analysis software during this work. Phase suppression lowered the time necessary to acquire a lifetime-resolved image to less than one tenth of that of the original FLIM system [14, 17-22]. When combined with the optimized analysis of spatial frequencies in the images with wavelets, the results in this chapter present the most quantitative approach to visualizing the activity of MT1-MMP in live cells. In addition, quantitative analysis is also presented demonstrating equivalence between the identification of the configuration of the biosensor derived from the polar plot and that derived from phase suppression.

In this chapter, the condition of the live cells was optimized so that the kinetics of the biosensor could be monitored for more than an hour following the removal of MMP inhibitors. Factors such as the osmotic stress endured by the cells during the removal of inhibitors, level of nutrients contained in the media during all stages of the culture and precise environmental controls were all optimized during the course of this research. In the initial proof-of-concept experiments performed on glass surfaces, the activation of the MT1-MMP biosensor was present around the entire perimeter of the HT-1080 cells without a bias for specific extensions or protrusions. However, in order to simulate the conditions encountered in vivo when a metastatic cancer cell is moving through the extra-cellular matrix in tissues, live HT-1080 were also cultured and imaged within 3-dimensional matrices of collagen-I. When compared to the cells imaged on glass surfaces, far more extensive morphological changes in the cells were observed in the 3D matrix following the removal of GM6001. In addition, the cleavage of the biosensor was specifically observed and followed at protrusive structures formed around the cell's

perimeter. However, the presented data also confirms that the correlation between the activation of MT1-MMP and the formation of protrusions along the edge of the cells cultured in collagen is complicated.

Materials/Methods

FLIM System

The excitation light from a 532 nm laser (World Star Tech, Toronto, Canada) was intensity modulated by a Pockels Cell (Conoptics Inc., Danbury, CT). The modulation frequency for the lifetime measurements was 40 MHz. All samples were imaged on a Leica DMIRB microscope (Leica, Germany). The emission was collected through a dichroic and emission filter combination passing 560 nm-640 nm (Omega Optical, Brattleboro, VT). The detection system consisted of an intensifier (Kentech, England) modulated at high frequency and CCD camera (QImaging, Surrey, BC) positioned at the output port of the microscope. The CCD camera collected images by performing a 2x2 binning resulting in images of 678x518 pixels. The live cells were imaged using a 100x/1.3NA oil immersion objective (Leica, Germany). All *in-vitro* measurements on the FLIM system were performed with a 40x/0.75NA air objective (Leica, Germany). The lifetime reference for all lifetime measurements was 1 μM Rhodamine 6G (Aldrich, Milwaukee, WI) in water (lifetime = 4.11ns [23]) .

Cell Culture

HT-1080 cells (ATCC, Manassas, VA) were cultured in Dulbecco's Modified Eagles Medium (DMEM) (Invitrogen, Carlsbad, CA) and transfected with Lipofectamine 2000 (Invitrogen, Carlsbad, CA). The AHLR-variant of the mOrange/mCherry MT1-

MMP biosensor [24] was contained in the pDisplay plasmid (Invitrogen, Carlsbad, CA). Following transfection, the cells were starved in 0.5% Fetal Bovine Serum (Atlanta Biologicals, Lawrenceville, GA) for 36-54 hours prior to imaging. The cells were incubated with 20 μM GM6001 (Merck, Germany) for 12-18 hours prior to imaging. During imaging, the GM6001 was washed out 5-6 times using CO_2 independent media (Invitrogen, Carlsbad, CA).

Protein Purification and Characterization

The mOrange2/mCherry MT1-MMP biosensor was purified by Nickel chelation after being expressed with an N-terminal His_6 tag in *Escherichia coli* [25]. Steady-state spectra were collected on a PC1 fluorometer (ISS Inc., Champaign, IL) in a solution at approximately 1 μM of the purified biosensor. The excitation wavelength was 532 nm and the emission was collected at 1nm increments from 555 nm to 750 nm. The recorded spectra were corrected for lamp fluctuations, background, the volume of trypsin (Invitrogen, Carlsbad, CA) added to cleave the biosensor and for emission-side corrections. Magic angle polarizer conditions were applied. The spectra were de-composed with linear spectral unmixing [26] with reference spectra provided by Roger Tsien's Lab. Lifetime measurements were carried with a solution of 1 μM of purified biosensor placed on a glass-bottomed Petri dish (Cell E&G, Houston, TX). Lifetime data was collected both before and after the biosensor was cleaved by trypsin using the filters described previously as well as with an additional 570 nm (±10 nm) bandpass filter (Omega Optical, Brattleboro, VT).

Collagen Matrix

The collagen matrices were prepared following the procedure modified from the protocols in [27, 28]. Initially, a solution containing 25µl of 0.1M PBS (pH = 7.1) and 102µl of 0.025M NaOH was mixed with 125µl of Collagen-I (BD Biosciences San Jose, CA). This solution was then sterilized by being subjected to UV illumination in a cell culture hood for 6 minutes. A suspension of HT-1080 cells transfected with the mOrange2/mCherry MT1-MMP biosensor and suspended in 5% FBS DMEM media was then added to the collagen solution prior to plating on a glass bottomed dish. The matrix containing the cells was then incubated for 5 minutes at 37C. Following the incubation, approximately 150 µl of 5% FBS DMEM containing 20mM GM6001 was added over the attached matrix. The cells were then imaged 12-18 hours after being plated within the collagen matrix.

LSM 710

Images of the collagen matrix were collected with second harmonic generation (SHG) on an LSM 710 (Zeiss, Germany). The excitation source used was a multi-photon Titanium Sapphire laser (Spectra Physics) emitting 70fs pulses at a wavelength of 780nm. A quarter-wave plate was inserted into the excitation path to circularly polarize the exciting light prior to being incident on the sample. The HT-1080 cells transfected with the biosensor were imaged with a 63x/1.4NA Apochromat objective (Zeiss, Germany). The resulting backwards SHG signal was collected through a dichroic mirror passing wavelengths less than 760nm to the non de-scanned detector on the system. In parallel, steady-state fluorescence images were collected by exciting the sample with a 561nm laser and detecting the emitted fluorescence between 581nm and 701nm.

Fractional Intensity Mapping

Many images of the HT-1080 cells in this chapter are presented with a color code. The color in each pixel was determined by the positions of each pixel on the polar plot relative to the centers of the intact and cleaved biosensors. More specifically, the color of each pixel depends on the contribution of each configuration (intact or cleaved) of biosensor to the steady-state intensity measured in that pixel. The configuration which contributes the largest fractional contribution to the total measured steady-state intensity determines the color in the pixel (red = intact biosensor, green = cleaved biosensor). However, the steady-state intensities of both configurations of the biosensor are similar because our emission filter accepts emission from both the donor and acceptor. Therefore, the fractional intensities are also estimates of the normalized concentration of each configuration of the biosensor (species fraction). With this analysis, spatial features of the biosensor's activity were observed and validated by analysis directly on the polar plot.

The fractional contributions to the steady-state intensity of the cleaved and intact biosensor at each pixel are determined from the polar plot coordinates according to the following matrix calculation.

$$\begin{bmatrix} x_{meas} \\ y_{meas} \end{bmatrix} = \begin{bmatrix} x_{mOr2} & x_{Bios} \\ y_{mOr2} & y_{Bios} \end{bmatrix} \begin{bmatrix} \alpha_{mOr2} \\ \alpha_{Bios} \end{bmatrix} \quad (1)$$

In Eq. 1, the terms $(x_{mOr2}),(y_{mOr2}),(x_{Bios})$ and (y_{Bios}) are the coordinates of the cleaved (mOrange2) and intact biosensor (Bios) on the polar plot. The corresponding measured data points are (x_{Meas}) and (y_{Meas}). The calculated contributions of each configuration (cleaved = mOrange2, intact = Bios) of the biosensor to the measured steady-state intensity at a pixel are (α_{mOr2}) and (α_{Bios}).

The polar coordinates of the two configurations of the MT1-MMP biosensor ($(x_{mOr2}),(y_{mOr2}),(x_{Bios})$ and (y_{Bios})) were determined by measuring a series of HT-1080 cells transfected with the biosensor. The positions on the polar plot assigned to each configuration of the biosensor were computed from bivariate Gaussian fits applied to the FLIM data from live cells Before representing the distribution of FLIM data on the polar plot by two dimensional Gaussian functions, the pixels belonging only to the cells were selected segmented after the suppression of background and noise by wavelets. The threshold was adjusted so that the majority of the cell body from each image was selected for the set of cells examined during this analysis. Following the segmentation, the pixels were binned to form a 3-dimensional histogram on the polar plot.

The data from the HT-1080 cells, which were not treated with the GM6001 inhibitor, were fitted with a double Gaussian bivariate fit (Supp. Fig. 3.1 and Table 3.1). The centers of the two Gaussian functions representing the cleaved and intact biosensor were found and are shown with their respective uncertainties in Table 3.1.

A single bivariate Gaussian fit applied to the images of live cells containing the MT1-MMP biosensor but pre-treated with the GM6001 inhibitor. GM6001 prevents the cleavage of the biosensor. After nine cells were analyzed, the fitting of these polar coordinates resulted in a single Gaussian distribution centered at a polar coordinate of

[0.764±0.0774,0.380±0.0566]. The above polar coordinates derived from the control HT-1080 cells (not pre-treated with GM6001) were used to represent the positions of the two configurations of the biosensor on the polar plot applied in this chapter.

Results

In-vitro Measurements of the mOrange2/mCherry MT1-MMP Biosensor

The MT1-MMP biosensor containing the mOrange2 and mCherry fluorescent proteins was examined in vitro with both steady-state and time-resolved fluorescence measurements. The solutions of biosensors measured in this section were expressed, extracted and purified from competent bacterial cells. Trypsin was used to cleave the biosensor for this characterization. The ability of trypsin to cleave the substrate of the biosensor can be seen clearly in the polyacrylamide gel (Fig. 3.1D). Only the cleaved components with masses between 25kD and 37kD remain in the center band. The left-most band contained proteins with masses between 50kD and 75kD (intact biosensor).

The time-resolved fluorescence of the biosensor was measured on the homodyne FLIM instrument at a modulation frequency of 40MHz while exciting the sample with a 532nm laser. Three fluorescent species (mOrange2, mCherry undergoing FRET and directly excited mCherry) were detected through a dichroic and emission filter combination passing 560nm to 640nm to the detector (Fig. 3.1C). When both configurations of the biosensor were measured (intact and cleaved) through this dichroic/filter combination, the polar coordinate of the biosensor upon cleavage moved toward longer lifetimes (Fig. 3.1A). The movement of the polar coordinate after cleavage toward longer lifetimes (Fig. 3.1A) suggests a loss of FRET.

In order to measure the mOrange2 protein in both the intact and cleaved biosensor, a bandpass filter passing only the emission of mOrange2 (570 nm ± 10 nm) was inserted before the detector. In both configurations of the biosensor, the mOrange2 had a multi-component lifetime distribution (Fig. 3.1B). However, the cleavage of the biosensor resulted in the polar coordinate for mOrange2 emission moving from near 2ns toward a region on the polar plot between 3ns and 4ns (Fig. 3.1B). This movement of the polar coordinate to a region of longer lifetimes after the cleavage of the biosensor also confirms the presence of FRET prior to the cleavage.

Steady-state measurements were performed at an excitation wavelength of 532nm to monitor changes in mOrange2's and mCherry's emission spectra before and after cleavage of the biosensor's substrate. In these experiments, a solution of purified biosensor was measured in a fluorometer both before and after the substrate of the biosensor was cleaved by trypsin. Spectral unmixing was applied using reference spectra from Roger Tsien's Lab to isolate the spectral contributions from mOrange2 and mCherry (Fig. 3.2). There was a clear increase in the fluorescence emission from mOrange2 following the cleavage of the biosensor (Figs. 3.2A and 3.2B). In parallel, the emission from mCherry decreased indicating the absence of FRET in the system (Figs 3.2A and 3.2B). The change in the spectrum of mCherry is only discernable after spectral unmixing because of bleed-through from mOrange2's emission. Although the variation in the FRET ratio (the donor's emitted intensity divided by the acceptor's emitted intensity) is small when compared to the difference in FRET ratio between the two configurations of the ECFP/YPet variant of the MT1-MMP biosensor, there is a significant change in the amount of energy transfer validated by both time-resolved and in-vitro measurements.

Background and Noise Removal

Images of the HT-1080 cells transfected with the mOrange2/mCherry biosensor contain significant noise from the intensified CCD camera and unwanted background light being emitted mainly from the cell's media. In most cases, the intensity of the unwanted (background) fluorescence is un-modulated with a very small phase delay. Throughout an image (frame) of a cell, the contribution of intensity from the background is not constant. For example, when a cell attaches and spreads on a slide, the edges of the cell are physically thinner than the central portions of the cell. Therefore, when using full-field microscopy, more background fluorescence will enter the image along the edge than in the center of the cell. Previous techniques that simply average the intensity in a region of interest not containing the cell and subtract that value from the image will not provide an accurate means to remove background. Likewise, the use of simple median filters or Gaussian mean filters to remove noise can degrade the spatial resolution in images. During this project, images were decomposed with basis functions called wavelets in order to reduce the unwanted fluorescence and noise in images [15, 29-31]. By analyzing the images according to spatial frequencies, uneven background and signal-dependent noise can be substantially reduced without losing spatial resolution (Please see introductory chapter on wavelets for detailed discussion).

An example of the variable background encountered in experiments using live cells is presented in Figure 3.3. The lifetime measurements taken in vitro indicate that the polar coordinates of the two configurations of the MT1-MMP biosensor are near the semi-circle (Fig. 3.1). Three regions of interest are examined spanning both the edge and interior parts of the cell (colored boxes in Figure 3.3A). The polar coordinates projected

from the pixels in the red region (edge of cell) are being pulled into the semi-circle (towards the origin) and likely contain an intensity contribution from background (Fig. 3.3C). The polar coordinates generated from the yellow region are located inside the semi-circle as well further indicating that intensity from the background may be present (Fig. 3.3D). However, in the central portion of the cell (green region of interest), the resulting polar coordinates are approximately at the semi-circle (Fig. 3.3E). Unlike the regions sampled near the edge of the cell, the relative contribution from background in the central portions of the cell is difficult to distinguish simply by looking at the polar plot. This could likely be the result of the increased thickness of the cell which also contributes to the increased signal measured in this region. In other words, there are more fluorophores in the center of the cell being imaged by the objective in the axial direction than along the thinner edges.

In all of the regions of interest, the removal of noise decreased the size of the distribution of polar coordinates (middle panel in Figs. 3.3C, 3.3D and 3.3E). However, the locations of the polar coordinates from each of the distributions still remained at positions indicative of the before-mentioned contributions from background. Following the removal of background, each of the distributions moved toward the semi-circle along a line connecting the original center of the distribution and the polar coordinate of the background. For example, the polar coordinates colored in red, moved toward 3ns on the polar plot after the background was removed from the image. If a line is drawn connecting the center of distribution of polar coordinates in red before the background was removed and the center of the same distribution after the background was removed, the line would pass through the area on the polar plot indicative of un-modulated

background. As expected, the relative contribution of the background was the most significant near the edge of the cell. The center of the distribution of polar coordinates located in the central region of the cell remained constant before and after the background was removed.

Spatial Features of the MT1-MMP Biosensor in HT-1080 Cells

HT-1080 cells transfected with MT1-MMP biosensor were imaged with FLIM, using the emission filter shown in Figure 3.1C and a 532nm laser for excitation. In order to examine the intact biosensor, the HT-1080 cell in Fig. 3.4 was imaged after incubation with the GM6001 inhibitor for 12-18 hours. The measured polar coordinates in the regions of interest selected within the cell (white squares in Fig. 3.4A and the polar plots in Fig. 3.4E) remained near 2 ns, indicating that the biosensor was mostly intact. Likewise, the fractional intensities, depicted by the color-coding in Figs. 3.4B, 3.4C and 3.4D, indicated that the biosensors within the cell were intact (red shading – intact biosensor, green shading – cleaved biosensor).

When cells were not incubated with the GM6001 inhibitor, the locations of the polar coordinates (Figs. 3.5A and 3.5E) and the mapping of fractional intensities (Fig 3.5B-3.5D) indicated that both configurations of the biosensor were present in the cell. Pixels from the regions of interest in Figure 3.5A are projected on the polar plots in Figure 3.5E; two separate lifetime pools near 2 ns and 3 ns are observed. The fractional intensities within the HT-1080 cells not treated with the GM6001 inhibitor (Fig. 3.5B-3.5D) showed that the intact biosensor was contained primarily in the brighter region near the nucleus (red shading in Fig. 3.5B and Fig. 3.5D), while the cleaved biosensor appeared mostly around the cell's periphery (green shading in Fig. 3.5C and Fig. 3.5D).

Phase Suppression Applied to Study Live Cells

Capillary

Experiments were carried out to test the resolution of phase suppression with two capillaries containing separately a solution of Rhodamine B (lifetime = 1.7ns) and a solution of Rhodamine 6G (lifetime = 4.11ns) (Fig. 3.6). The concentration of each solution was adjusted so that both capillaries could be simultaneously imaged with the same excitation source, gain settings of the detector, objective and emission filters. In this experiment, two detector phases were chosen to suppress the intensity from the capillary of Rhodamine B and two different detector phases were selected to remove the intensity emitted from the capillary of Rhodamine 6G. In the resulting difference images (Figs. 3.6B and 3.6C), the intensity from each capillary is highlighted in the frame of the image with high contrast. Spatial features of the capillary such as the indentation on the top edge of the capillary can also be seen in the difference images (Figs. 3.6B and 3.6C).

Single Cells

Initially, experiments were carried out to determine how well phase suppression could resolve the two configurations of the biosensor on an image of an HT-1080 cell transfected with the mOrange2/mCherry MT1-MMP biosensor (Fig. 3.7). This cell was not treated with MMP inhibitors and therefore, contained a mixture of intact and cleaved biosensors. The mapping of the fractional intensities indicated that the cleaved biosensor (green) was present along the periphery of the cell and the intact biosensor (red) remained in the central portion of the cell (Figs. 3.7B, 3.7C and 3.7D). Two detector phases were chosen to suppress the intensity from the cleaved biosensor and separately two detector phases were chosen to suppress the intensity from the intact biosensor. The two selected

phase images were subtracted so that positive intensities remained in areas of the image containing fluorescent species that were not suppressed. In other words, if the intact biosensor was suppressed, then the cleaved biosensor would appear as a positive value in the difference image. Any negative values in areas of the difference images where intensity from a specific fluorescent species was being suppressed, were due to noise or precision of the phase setting. Only positive values are shown in the phase suppression images (Figs. 3.7E-3.7G) and throughout the images presented in this chapter. As a result, the intensities remaining in the difference images indicate the regions of the cell where the fluorescence emission is dominated by either the intact (Fig. 3.7F) or cleaved biosensor (Fig. 3.7E).

During these experiments, the HT-1080 cells transfected with the biosensor were excited with a 532nm laser and imaged with the homodyne FLIM system. As shown, the regions highlighted by the fractional intensity mapping indicative of each configuration of the biosensor (derived from the polar plot) match the corresponding intensities highlighted by the phase suppression. For example, the green regions in the fractional intensity mapping (Figs. 3.7B) match the intensities in the difference images from the cleaved biosensor (Fig. 3.7E). Therefore, phase suppression can indicate the configuration of the biosensor as well in this case but with only two exposures of the sample.

Improving Temporal Resolution: HT-1080 Cells Cultured on Glass Surfaces

Experiments were conducted to evaluate the temporal resolution of phase suppression for monitoring the kinetics of the mOrange2/mCherry MT1-MMP biosensor in live HT-1080 cells. In the previous analysis of single cells, large changes in the

configuration of the biosensor were observed because the MT1-MMP enzyme was allowed to cleave the biosensor for more than 12 hours at 37C prior to imaging. However, in order to visualize and follow the activation of the MT1-MMP biosensor dynamically, the MMP inhibitor GM6001 can be washed out from the media of a cell pre-treated with the inhibitor. In these experiments the MT1-MMP enzyme would be activated and its activity could be followed at smaller intervals of time with phase suppression. Imaging cells for extended periods required improvements in both the conditions of the cell as well as the environmental conditions on the stage of the microscope.

The initial experiments observed the activation of the MT1-MMP both before and thirty minutes after the removal of the GM6001 inhibitor from the cell's media (Figs. 3.8 and 3.9). Rhodamine 6G was used to determine accurately the phase setting of the instrument prior to the measurements being taken on cells. Four phase angles were selected for the phase suppression in order to suppress the intensity from mOrange2 (cleaved biosensor) and separately to suppress the intensity from the intact biosensor. Full-field homodyne FLIM images were taken in parallel with the images gathered for the phase suppression. During these experiments, images were acquired prior to the washout of GM6001 (Fig. 3.8) as well as at a time approximately thirty minutes following the washout (Fig. 3.9).

As shown by red shading in Fig. 3.8D, prior to the washout of the GM6001 inhibitor, the intact biosensor's fractional intensity was dominant in the majority of the cell body. Some intensity from the cleaved biosensor appeared along the cell's edge (green shading in Fig 3.8C). When the pixels from the regions of interest in Fig. 3.8E

were projected on the polar plots in Fig. 3.8F, the polar coordinates at locations within the cell body were close to 2 ns. Near the bottom of the cell (region 3 in Figs. 3.8E and 3.8F), the polar coordinates corresponded to lifetimes above 2 ns. When phase suppression was applied to suppress the intensity from the intact biosensor (Fig. 3.8A) very little intensity remained in the cell body with only a few low intensity features appearing along the cell's edge. However, when the intensity from the mOrange2 (cleaved biosensor) was suppressed (Fig. 3.8B) the intensity remaining in the difference image (indicative of the intact biosensor) was shown to be distributed throughout the majority of the cell's interior body.

Following the washout of GM6001, the fractional intensity around the edge of the cell was dominated by mOrange2 (cleaved biosensor) (green shading in Fig. 3.9C). The difference image shown in Fig. 3.9A, where the intact biosensor's intensity was suppressed, paralleled the trends indicated by the polar plot analysis using fractional intensities. Thus, when the intensity from the intact biosensor was suppressed, intensity in the difference image, representing free mOrange2 (cleaved biosensor), was found predominantly at the cell's edge (Fig. 3.9A). This latter intensity, corresponding to free mOrange2, matched well to the green regions in Fig. 3.9C where the fractional intensity from the cleaved biosensor was dominant. The intensity from the intact biosensor remained primarily within the central portion of the cell body (Figs. 3.9B and 3.9D). In addition, when projected on the polar plot, the pixels from the regions of interest 1 and 3 are located closer to 3 ns while region 2 remained closer to 2 ns (Fig 3.9E and 3.9F).

However, the study of the biosensor required images to be acquired at much finer steps in time in order to observe biologically relevant phenomena. In Figure 3.10, an HT-

1080 cell transfected with the MT1-MMP biosensor was imaged at 15 minutes intervals for a period of one hour following the removal of the GM6001 from the media. In this example and in the following data sets presented, changes in the culture protocol related to the FBS content and media required a change in the polar coordinates calculated for the intact and cleaved biosensor. Therefore, these new polar coordinate centers were calculated as [0.6265,0.4197] and [0.7399,0.4035]. Intensity images of the cell representing the average of the four images collected for phase suppression are shown at the indicated time intervals in Figure 3.10A. As shown in these images, the formation of a protrusion along the lower left side of the cell occurred concurrently with the retraction of the cell's bottom edge. Two sets of detector phases were chosen to suppress the intensity from the intact biosensor and separately, to suppress the intensity from the cleaved biosensor. The difference images that result from the subtraction from each set of detector phases chosen are shown in the Figures 3.10B and 3.10C. In other words, the intensities shown in Figure 3.10C are the result of the cleaved biosensor and the intensities in Figure 3.10B correspond to emission from the intact biosensor. Following the removal of the MMP inhibitor GM6001, intensity from the cleaved biosensor emerged along the protrusion primarily near the top and also near the bottom left side of the cell. The intensity from the intact biosensor remained in the center of the cell throughout the imaging session.

By further improving the environmental conditions on the microscope's stage and during the cell's culture, the activity of the MT1-MMP biosensor could be monitored with even finer temporal resolution (Figs. 3.11 and 3.12). In these experiments, the HT-1080 cells were cultured on glass slides and pre-incubated with the MT1-MMP inhibitor

GM6001. As a result, the polar coordinates sampled in the various regions of interest at the beginning of each experiment were located near 2ns on the polar plot suggesting that the biosensor was initially intact (Figs. 3.11A, 3.11B, 3.12A and 3.12B). After the inhibitor was removed (washed out from) the media, the cells attached to glass underwent limited morphological changes (Figs. 3.11E and 3.12E). For example, the most noticeable change in the morphology of the cells indicated by the average intensities was a small protrusion which formed along the bottom of the second cell (intensity images in Fig. 3.12E). In both sets of intensity images, the features in the cells indicated by the staining of the biosensor such as the nucleus, the bright area adjacent to the nucleus and the dimmer edges remained consistent throughout the experiment. However, at a time of forty five minutes following the removal of the MMP inhibitor GM6001, the polar coordinates in regions 1 and 3 in Figures 3.11C and 3.11D moved closer to 3ns which suggested that the biosensor was cleaved at those locations. Likewise, in the second example, the polar coordinates in regions 1, 3 and 4 in Figures 3.12C and 3.12D were also located near 3ns implying the presence of the cleaved biosensor at a time of hour after the inhibitor was removed from the media.

In order to asses the configuration of the biosensor in the difference images produced during the imaging with phase suppression, a color coding has been applied to these images. In Figures 3.11F and 3.12F for example, areas colored in green indicate the locations in the cell where the intensity from the difference image (product of the subtraction of two phase images) indicative of the cleaved biosensor is greater than the corresponding intensity in the separate difference image that highlights intensity from intact biosensor. Therefore, the green color in the images indicates the presence of the

cleaved biosensor and in a similar manner, areas in the images colored red correspond to locations in the cell containing the intact biosensor. This method of rendering images produced by phase suppression in color was also applied in the next section which examined the HT-1080 cells transfected with the MT1-MMP biosensor in matrices of collagen-I.

Therefore, the images rendered in Figures 3.11F and 3.12F monitor the state of the biosensor's configuration throughout the entire cell cultured on a glass surface simply using phase suppression. As time progressed after the MMP inhibitor (GM6001) was removed, the active MT1-MMP enzymes cleaved the biosensor throughout the underside of the cell. Intensity in the difference images generated by the phase suppression emerged from the cleaved biosensor while the intensity from the intact biosensor concurrently decreased (Figs. 3.11F and 3.2F). In both of the cells shown (Figs. 3.11 and 3.12), the cleavage of the biosensor began along the edge of the cell and then gradually proceeded inward toward the center of the cell. However, the intensity from the intact biosensor was present consistently in the bright area adjacent to the nucleus even at the final time point sampled. In the majority of cases sampled during this study (data not shown), the cleavage of the biosensor took place around the entire perimeter of the HT-1080 cells cultured on glass. The change in configuration of the biosensor was not biased significantly toward protrusions or extensions of the cell's membrane.

HT-1080 Cells in 3D Matrices of Collagen-I

Live HT-1080 cells were cultured and imaged within 3-dimensional matrices of collagen-I. The matrix of collagen was intended to simulate the environment encountered by a metastasizing cancer cell as it leaves the primary tumor and negotiates through the

extra-cellular matrix (ECM) (in order to enter a part of the vasculature and invade distant tissues). In the preparation of the collagen matrix, maintaining the cell's vital condition in the collagen and positioning the cells in the matrix within the working distance of the objectives used were the primary obstacles in these experiments. Likewise, the HT-1080 themselves will exert a pulling force on the collagen once attached. If the density of cells in the matrix is too high, the pulling forces exerted by all the cells can both shrink and detach the matrix of collagen in a process referred to as matrix contraction. As lengthy testing demonstrated, the attachment of the collagen to the glass surface is a very sensitive process. Specifically, the time that the collagen spends in the incubator after it has been initially applied to culture dish needs to be carefully monitored. Variations in the procedure described to prepare the matrix on order of tens of seconds can also result in a premature detachment of the matrix.

In order to characterize the HT-1080 cells in the 3D matrix, steady-state fluorescence images of the cells were collected in parallel with images of the collagen-I (Fig. 3.13). The steady-state intensity images were generated first before the two-photon laser passed over the field of view to instigate the scatter (second harmonic generation (SHG)) necessary to image the collagen. The backwards SHG signal detected here may not be indicative of all the collagen present but the images of the collagen do indicate that the cells are successfully incorporated into the matrix. In order to prevent the cells from disrupting the collagen, the cells were treated with the MMP inhibitor GM6001 (20mM) immediately following their incorporation into the collagen matrix (approximately 12-18 hours prior to imaging). A definite hole is present (dark area) in the images of the collagen-I mirroring the location of the cells shown in the corresponding steady-state

intensity images. None of the proteins such as actin or the microtubules in the cell's cytoskeleton have non-centrosymmetry or the long coherence length which instigate strong SHG signals. In the SHG images of the collagen-I, the density of the collagen-I is highest near the edge of the cell and slightly decreases throughout the region imaged. The fiber length, pore sizes between the fibers and overall density also vary though between the cells sampled.

The spatiotemporal activation of the MT1-MMP enzyme was monitored within the HT-1080 cells transfected with the MT1-MMP biosensor and cultured in the 3-dimensional collagen matrices (Figs. 3.14-3.18). As before, the cells were pre-incubated with the MMP inhibitor GM6001 prior to imaging and the MT1-MMP enzyme was activated by removing (washing away) the inhibitor from the cell's media.

The results from three experiments in which a configurational change in the biosensor was observed following the removal of GM6001 from the cell's media are shown in Figures 3.14, 3.15 and 3.16. In the first example (Fig. 3.14), immediately following the incubation with GM6001, the coordinates selected from regions of interest (white boxes in Fig. 3.14A), were projected near 2ns on the polar plot (Fig. 3.14B) indicating that the biosensor was intact. Likewise, the majority of the intensity shown in the difference images (generated by phase suppression) was from the intact biosensor prior to the removal of the MMP inhibitor GM6001 ("Before" image in Fig. 3.14F). In this experiment, the morphological changes as evaluated by the fluorescent staining of the biosensor (intensity images in Fig. 3.14E), taking place after the removal of GM6001 were much more significant when compared to the previous experiments conducted on the glass surfaces. An expansion of the cell occurred along the top edge of the cell while

at the same time, the extension along the cell's bottom edge that was initially present, retracted during the imaging period. On the top of the cell, the membrane appeared to expand in a fan-like shape into the matrix of collagen. As shown by the color renderings of the difference images generated by phase suppression, both events were accompanied by a configurational change in the biosensor (going from intact to cleaved) specific to those locations (increase in green shading in Fig. 3.14F). As the top fan-like shaped protrusion became larger, the population of the cleaved biosensors in this area increased incrementally. In the two regions of interest in the top fan-like protrusion (regions 1 and 4 in Fig. 3.14C), the polar coordinates moved closer to 3ns suggesting also that the biosensor was cleaved in those areas. As the central portion of the cell contracted from an elliptical to a circular morphology during the period of imaging, the polar coordinates from these regions (regions 3 and 4) as well as the colored renderings of the difference images (Fig. 3.14F) indicated that the biosensor was intact in these areas (center of cell).

A second example of an experiment conducted to examine the activation of MT1-MMP in transfected HT-1080 cells cultured in a 3D matrix of collagen-I is presented in Figure 3.15. Unlike the previous example, following the removal of the GM6001 inhibitor, the cell's morphology as estimated by the images of average intensity in Fig. 3.15E, changed with multiple protrusions extending and retracting throughout the imaging session. However, at a time of approximately ten minutes after the inhibitor was removed, one prominent protrusion emerged along the top left of the cell. At the leading edges of this protrusion, the configuration of the biosensor progressively changed from intact to cleaved indicating the MT1-MMP enzyme was active. The change in the configuration of the biosensor was verified on the polar plot (region 4 in Fig. 3.15D) as

well as by the colored rendering of the difference images (Fig. 3.15F). For example, the polar coordinates corresponding to the edge of the protrusions (region 4 in Fig. 3.15D) were located near 3ns and therefore corresponded to the cleaved biosensor. On the lower right portion of the cell, a protrusion formed extending into the collagen matrix and later retracted prior to the end of the imaging period (Fig. 3.15E). The extension occurred immediately after the inhibitor GM6001 was removed and continued until a time of forty minutes following the removal of GM6001 when retraction began. In this area, intensity from the cleaved biosensor was most abundant between a time of thirty minutes and thirty five minutes after the removal of the MMP inhibitor. Upon retraction, the intensity from the intact biosensor became more dominant. After one hour following the removal of the MMP inhibitor, the pixels near this protrusion (region 2 in Fig. 3.15C) were projected near the position of the intact biosensor (near 2ns) on the polar plot in Figure 3.15D. In the colored (red/green) images rendered from the phase suppression (Fig. 3.15F), a few spurious green pixels appeared possibly indicating the presence of the cleaved biosensor. However, these pixels were likely the result of noise in the detected signal. Only those green pixels (intensity from the cleaved biosensor in the difference images) in Figure 3.15F concentrated in specific regions of the cell can be quantitatively attributed to the presence of the cleaved biosensor.

In the final example (Fig. 3.16), an HT-1080 cell undergoing both morphological changes corresponding to configurational changes in the biosensor is presented. In this case, the overall morphology of the cell remained constant with two protrusions emerging along the left side of the cell during imaging (see intensity images in Fig. 3.16E). However, in this cell the activation of the MT1-MMP visualized by an increase in

intensity from the cleaved biosensor (green shading in Fig. 3.16F) occurred with a delay as a protrusion emerged along the top of the cell. As before, the pre-treatment of the cells with GM6001 prevented the biosensor from being cleaved (red shading from Fig. 3.16F in "Before" image and polar plots in Fig. 3.16B). After the MMP inhibitor GM6001 was removed, a protrusion formed and retracted in the top left corner of the cell during imaging. This protrusion began to form approximately ten minutes after the inhibitor was removed and was very prominent in the intensity image of the cell twenty minutes after the inhibitor was removed. However, intensity from the cleaved biosensor did not become apparent until thirty minutes after the inhibitor was removed. Intensity from the cleaved biosensor became most prominent midway through the imaging experiment along this protrusion (near the times of thirty five minutes and forty minutes after the removal of the inhibitor). The increase in intensity from the intact biosensor occurred concurrently with the retraction of the protrusion. During the experiment, a protrusion (near region 1 in Fig. 3.16C) grew out from the bottom left side of the cell beginning approximately fifty minutes after the GM6001 was washed out. In this case however, the activation of the enzyme occurred as the protrusion grew. Finer time resolution would be able to more carefully correlate the growth of protrusions and the activity of MT1-MMP. On the polar plot, the movement of the polar coordinates in region 1 shown in Figure 3.16C toward a position near 3ns likely also suggests that the MT1-MMP is active and cleaving the biosensor.

In some cases, morphological changes including the formation of protrusions and extensions of the cell's membrane occurred without a concurrent change in the configuration of the biosensor (Fig. 3.17). The transfected HT-1080 cell described in

Figure 3.17 was cultured in a 3-dimensional collagen matrix and pre-treated with the MMP inhibitor GM6001. As before, two detector phases were chosen to suppress the intensity from the intact biosensor and separately, two detector phases were selected to suppress the intensity from the cleaved biosensor. The difference images generated from these phase images therefore, follow the intensities from the intact and cleaved biosensor in the images (Fig. 3.17F). In the series of intensity images collected during the imaging of the first cell for example, protrusions (extensions) emerged along the top and bottom of the cell (Fig. 3.17E). However, at no time following the removal of GM6001 was there any substantial intensity from the cleaved biosensor in the difference images generated with phase suppression along this protrusion or anywhere in the cell (Fig. 3.17F). During the imaging period, a few green pixels possibly indicative of the cleaved biosensor appeared randomly. These pixels were likely the result of noise. When the pixels from the four regions of interest were analyzed on the polar plot (Figs. 3.17C and 3.17D), no configurational change in the biosensor was observed at a time of nearly an hour following the removal of the GM6001 inhibitor from the cell's media. All polar coordinates including those at the protrusions (regions 1 and 4 in Fig. 3.17C) were located near 2ns indicating that the biosensor was intact.

In Figure 3.18, a second example further demonstrates that morphological changes taking place within the HT-1080 cells following the removal of MMP inhibitors may not require the activity of MT1-MMP. Before the MMP inhibitor (GM6001) was removed, the polar coordinates from the pixels located in four regions of interest highlighted in Figure 3.18A, were all near 2ns on the polar plot (Fig. 3.18B). As time progressed following the removal of GM6001, the average intensity images indicated that

a definite protrusion formed along the lower left side of the cell (Fig. 3.18E) while at the same time, the topmost area of the cell (near region 2 in Fig. 3.18A) underwent an expansion toward the top of the image's frame. At a time one hour after the inhibitor GM6001 was washed out of the cell's media, the polar coordinates from pixels sampled throughout the cell were projected on the polar plot (Figs. 3.18C and 3.18D). In each region of interest, all polar coordinates remained near 2ns which likely corresponds to the intact biosensor. Even in the regions sampled directly along the protrusion (regions 1 and 2 in Fig. 3.18C), the polar coordinates still indicate that the biosensor is likely intact. In the region 1 specifically along the protrusion, some of the pixels were near 3ns possibly indicating that the biosensor was cleaved. However, the signal levels in this region was low and as a result, the data were noisy (please refer to section on the noise of the instrument for more specific explanations). In this case, the average polar coordinate (near 2ns) represents the fluorescent species in that area. Difference images were also generated from the individual phase images selected to suppress the intensity from the intact and separately the cleaved biosensor. In time, there were no definite regions in the cell containing intensity from the cleaved biosensor (Fig. 3.18F). The intensity from the difference image contained contributions dominantly from the intact biosensor.

Discussion

In this chapter, the activity of the MT1-MMP enzyme was examined throughout live HT-1080 cells containing the mOrange2/mCherry MT1-MMP biosensor. On the polar plot, the polar coordinates corresponding to the intact and cleaved biosensor were sufficiently distinct so that the configuration of the biosensor could be classified on a

pixel-wise basis. Although the analysis conducted on the polar plot was based on the relative intensity emitted by each configuration of the biosensor, the set of emission wavelengths detected by the intensified CCD was selected to make the integrated intensities of both configurations of the biosensor approximately equal. Hence, the calculations carried out on the polar plot not only assigned a classification of the biosensor's configuration based on intensity but also, based on the actual normalized concentration of the biosensor present. With the incorporation of phase suppression into the lifetime imaging system, the kinetics of MT1-MMP's activation could be monitored for more than an hour following the removal of MMP inhibitors without the effects of photo-damage killing the cell. The equivalence between the intensities highlighted by phase suppression and the configuration of the biosensor derived from calculations on the polar plot was shown in multiple sets of experimental data. As such, the intensities in the difference images generated from phase suppression also provided an estimation of the normalized concentration of each configuration of the biosensor present.

With the data and analysis presented, new patterns of MT1-MMP's activity in matrices of collagen have been observed specifically near protrusions. In contrast, when cells have been studied in two-dimensional settings both in the literature [32] and in this chapter, the activity of MT1-MMP is spread throughout the entire perimeter of the cell without a specific bias for protrusions. The HT-1080 cells cultured in collagen also underwent more substantial morphological changes than the HT-1080 cells examined on glass surfaces. These protrusions observed along the perimeters of the cells cultured in collagen, are ideal locations from which to investigate how the cancer cells examine and essentially collect information from their local environment. These protrusions observed

consisted both of small point-like extensions as well as large fan-shaped expansions spreading from the main cell body. In some of the presented cases, the activity of MT1-MMP was accompanied by the formation of protrusions while in another example, MT1-MMP's activity was delayed relative to the development of protrusions. A portion of the presented data even implied that the activity of MT1-MMP may not be necessary for a cell to extend protrusive structures.

Although these results confirm that MT1-MMP's role regulating the invasive character of cancer cells is likely quite complex, the presented data motivates more questions than conclusions about the activity MT1-MMP. A detailed investigation of the cell's local environment would be necessary to understand fundamentally the reason why MT1-MMP is active only in certain protrusions as the cell undergoes morphological changes. One possible explanation for the selective activity of MT1-MMP may be related to the density of collagen located in the cell's local environment. In the case of migration for example, the MT1-MMP-dependent migration has already been shown to depend on the density of collagen in the areas immediately surrounding the cell [33-36]. As shown in the images of the collagen-I collected with SHG in this chapter, the density of the collagen and the pore sizes formed between the collagen fibers can vary even in different locations within the same culture dish. The concurrent imaging of the collagen fibers along with the fluorescence emitted by the biosensor would be crucial in order to understand MT1-MMP's role as the cell interacts with collagen matrix. Also, studying the proteolytic damage to the collagen matrix following the activity of MT1-MMP-dependent and MT1-MMP–independent protrusions would reveal very useful information to characterize these interactions. In addition, the incorporation of transmitted light

microscopy would also be useful to look for features in the cell's local environment that would be undetectable by imaging with fluorescence.

In future studies, this project will require improved spatial resolution in both the lateral and axial directions. Visualizing collagen with fluorescently labels such as Fluorescein is also necessary because the 2-photon lasers capable of imaging collagen with SHG would readily kill live cells (specifically when the collagen is not well-ordered). In addition, the HT-1080 cells cultured in the collagen matrix likely do not position themselves precisely parallel to the plane observed by the microscope's objective. In most cases, specific portions of the cell such as features along the edge of the cells (or even the protrusions observed here) likely span multiple planes in the axial dimension. Currently, two modalities of high resolution fluorescence imaging (spinning disk confocal [29] and light sheet illumination [37]) exist which are conducive for live cell imaging. New advances in light sheet illumination may also allow for cells to be imaged individually in live tissues. Furthermore, an overall modulation frequency of 60MHz instead of the 40MHz used in this chapter would provide an approximately twenty percent improvement in the resolution of the two configurations of the biosensor on the polar plot when compared to the resolution obtained in this chapter. Noise could be substantially reduced with newer equipment such as laser diodes whose intensity can be directly modulated and modern intensifiers. Unlike a collimated laser passing through a Pockels cell, directly modulating the intensity of light emitted by a laser diode lowers the noise in the acquired lifetime images because of the increase in the modulation depth (AC/DC ratio) of the emitted light. Newer phosphor screens as well as more sensitive

cathodes on image intensifiers can also reduce noise so that smaller changes in lifetime can be robustly quantified.

Finally, one aspect of imaging biosensors in live cells that has been largely overlooked in the literature is the necessity to monitor the position of a biosensor in the cell after it has adopted a different configuration. For example, if the MT1-MMP biosensor studied here is changing configuration in some specific region of the cell, how can a newly cleaved biosensor be distinguished from a biosensor that was previously cleaved and just moved within the cell. Being able to track a cleaved biosensor after its interaction with the MT1-MMP enzyme or at the very least, being able to establish where the biosensor was initially activated is absolutely necessary to understand the biology conveyed by the activation patterns. Recently traditional tools in data analysis such as auto-correlation are starting to be applied to study and monitor biosensors after being initially activated in live cells [38, 39]. With both improved temporal and spatial resolution, these sorts of statistical tools will no doubt, clarify and more accurately characterize the activation patterns of the MT1-MMP biosensor observed in this chapter.

PhaseDelayImaging Software

The research presented in this chapter required new software principally to acquire images at continuously variable phase shifts (phase of radio frequency injected into the detector's gain). This software coordinated the functions of the Uniblitz shutter, CCD camera and phase shifter (Lorsch) specific to the values entered into the user interface (Supp. Fig. 3.2). In short, the Uniblitz shutter and digital phase shifter can be controlled by appropriately timed TTL pulses emitted from the local PCI card (National

Instruments). The digital phase shifter can be continuously varied with a precision of within $\pm 0.7^{o}$. In the software's control window (Supp. Fig. 3.2), the box labeled "Actual Phase" indicates the true phase shift outputted by the phase shifter once the user requests a specific phase in the "Desired Phase" box. The camera is operated with functions from the QCam API package. The exposure time and binning can be varied depending on the needs of the experiment. Following the acquisition of an image, the windows-based SaveFileDialog directs the user to declare a filename and location to save the image to. These images are stored as binary images with a frame size of 678x518 pixels. Many commercial software packages including MatLab, Autoquant and MetaMorph can open the image for further image processing.

Figures

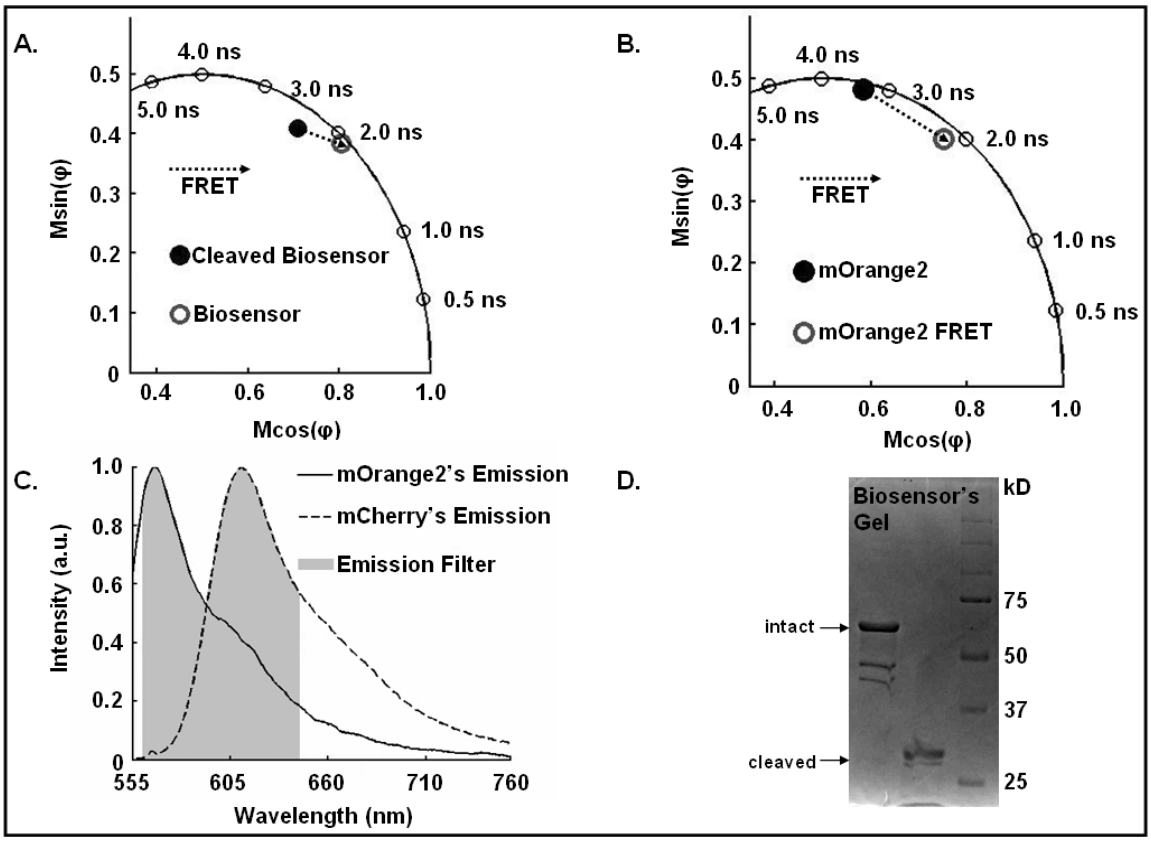

Figure 3.1: Time-resolved in-vitro measurements: (A) The polar coordinates of the MT1-MMP biosensor were measured before and after the biosensor was cleaved by trypsin. Measurements were taken at a modulation frequency of 40MHz through the emission filter shown in (C). (B) The phase delay and modulation ratio of the mOrange2 was also measured on both configurations of the biosensor at an emission wavelength of 570nm ± 10nm. When measured and plotted on the polar plot at a modulation frequency of 40MHz, there is a definite movement of the polar coordinate toward longer lifetimes after cleavage of the biosensor. (C) The normalized emission spectra of mOrange2 and mCherry are displayed along with the filter pass of the emission filter used in (A) (and used for the live cell measurements) highlighted. (D) Separate protein solutions of the intact biosensor and the biosensor cleaved by trypsin were examined in the electrophoresis gel. The leftmost lane contains the intact biosensor and the center lane contains the cleaved biosensor. The far right lane is the indicator lane displaying the reference masses.

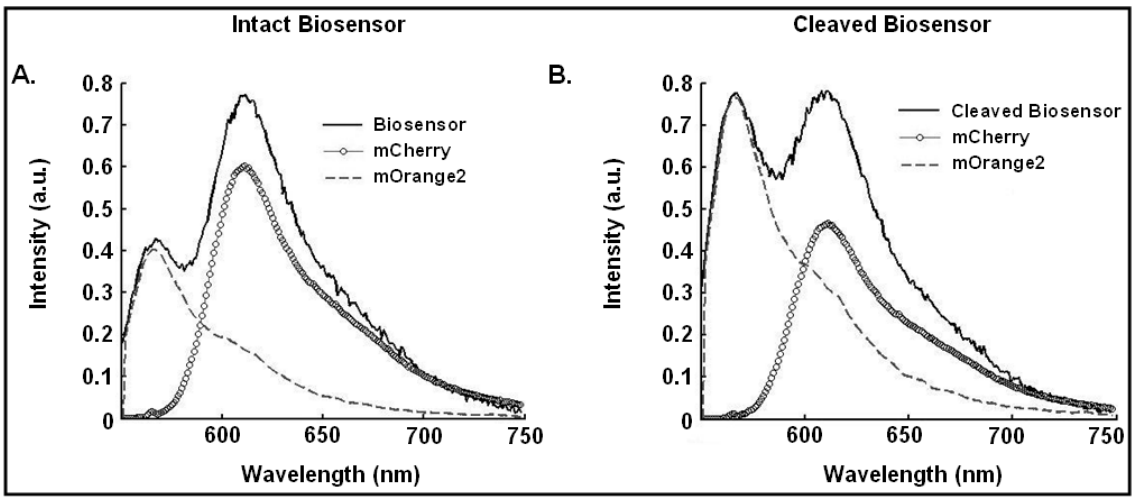

Figure 3.2: Steady-state measurements taken on the MT1-MMP biosensor: (A) The emission spectrum of the intact MT1-MMP biosensor was measured with an excitation wavelength of 532nm. Linear spectral unmixing was applied to resolve the contributions of the mOrange2 and mCherry separately. (B) The emission spectrum of the cleaved biosensor was also measured at an excitation wavelength of 532nm. After the biosensor was cleaved, there is a definite loss in emission from the mCherry and an increase in fluorescence emission from the mOrange2 relative to (A) indicating a loss of FRET.

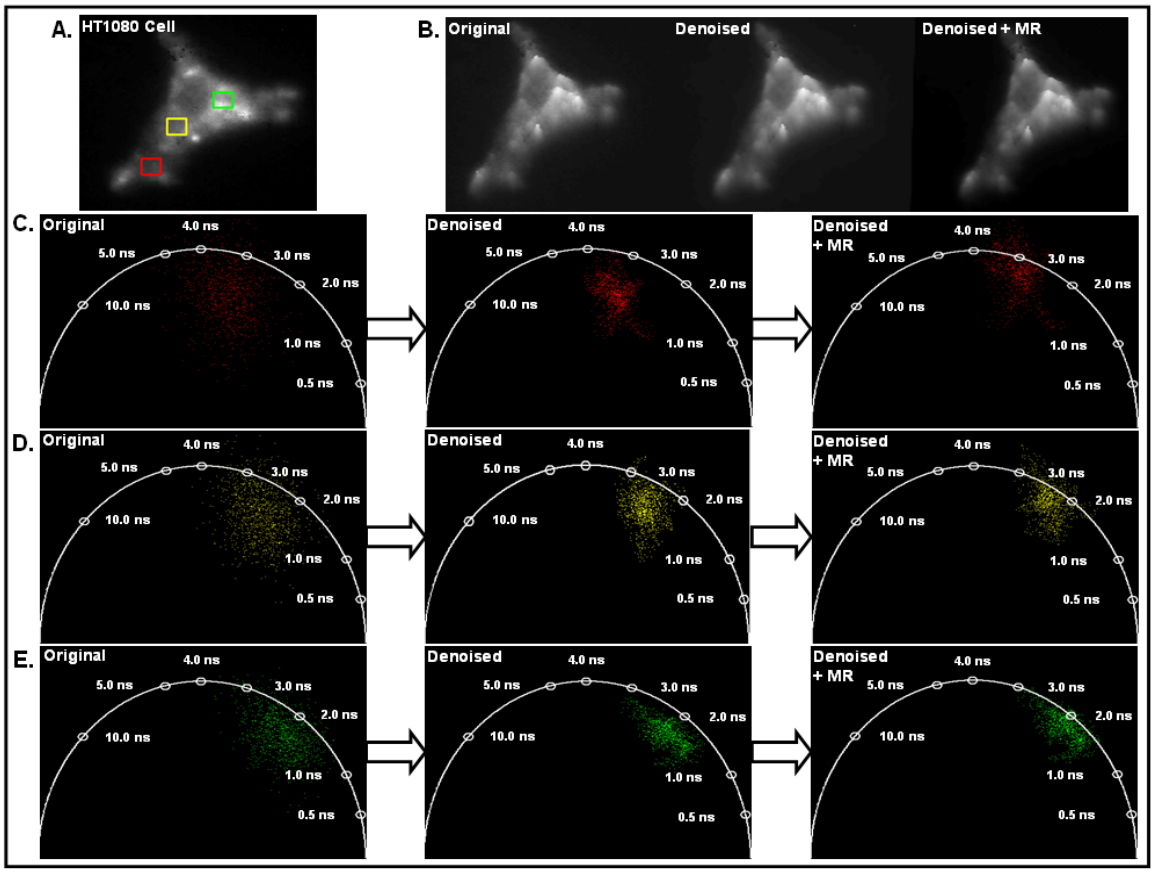

Figure 3.3: Analyzing measurements of live cells with wavelets: (A) An intensity image of an HT1080 cell not treated with the GM6001 inhibitor is shown with the regions of interest for (C), (D) and (E) highlighted. (B) Intensity images of the HT1080 cell not treated with the GM6001 inhibitor describing the morphology of the cell is displayed following the denoising (center image) and the multi-resolution background removal (far right image). (C) The pixels from the red region of interest shown in (A) are projected on the polar plot during the denoising and background removal steps. Near the edge of the cell, there is considerable background likely from the media that the cells are immersed in. (D) The pixels from the yellow region of interest near the nucleus of the cell in (A) are plotted on the polar plot. This region still has very detectable background despite being taken from a region with higher intensity on the cell. (E) The pixels of the green region of higher intensity in (A) are displayed on the polar plot. Interestingly, after the background removal, there appears to be a second lifetime pool here near 2ns as compared to the region in (C) which was near 3ns

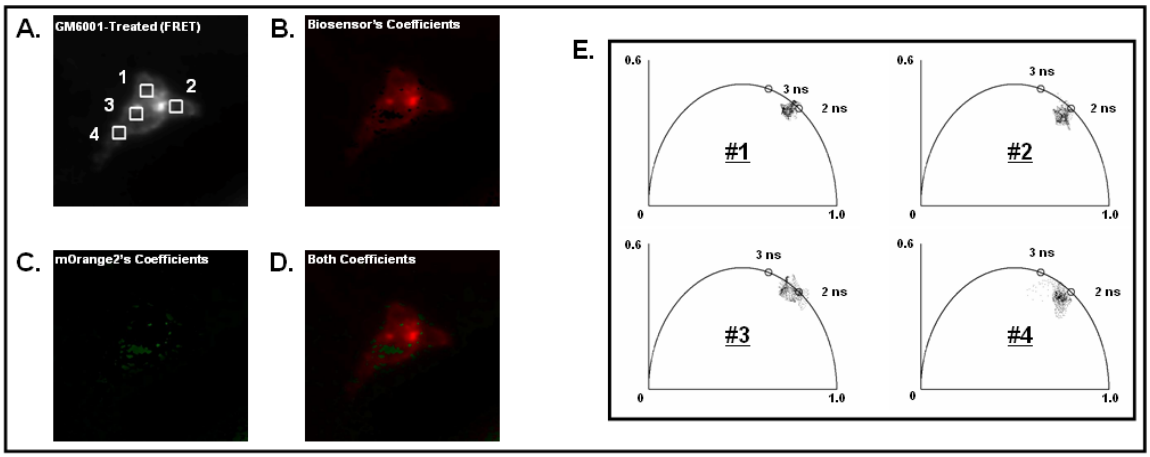

Figure 3.4: HT-1080 cell treated with the GM6001 inhibitor: (A) An intensity image of an HT-1080 cell taken during a FLIM experiment while homodyning is presented with four regions of interest highlighted in white. (B) An IMD (intensity-masked display) image is shown where the red shading indicates where the fractional intensity of the intact biosensor is dominant relative to the cleaved biosensor. (C) In this IMD image, the areas in the cell where the fractional intensity from the cleaved biosensor is dominant are shown in green. (D) When both (B) and (C) are combined, the resulting cell image shows that most of the collected intensity is being emitted from the intact biosensor as indicated by the red shading. (E) The pixels from the regions in interest in (A) are projected on the polar plot in these scatter plots. The plots indicate that there is likely a single lifetime pool near 2ns representing the intact biosensor.

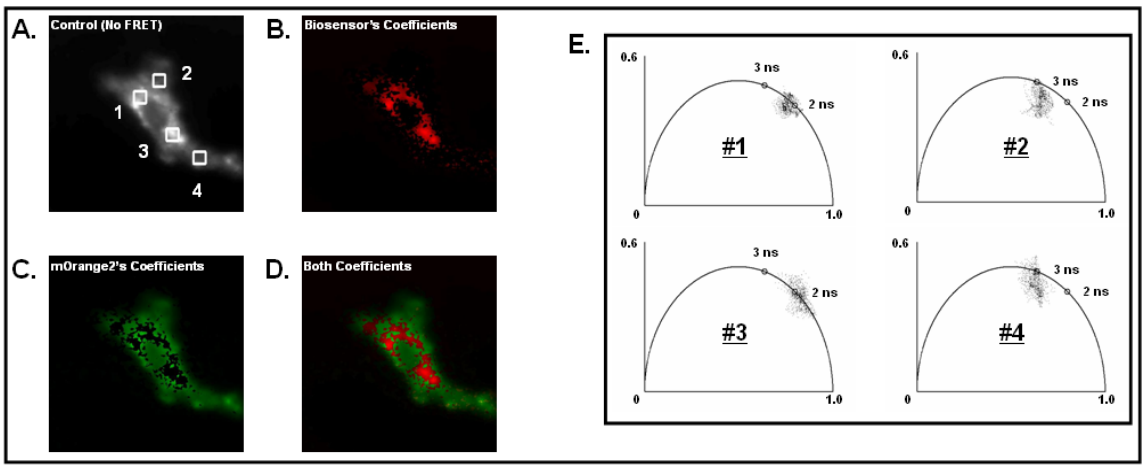

Figure 3.5: HT-1080 cell not treated with the GM6001 inhibitor: (A) An intensity image of an HT-1080 is shown with regions of interests (1-4) highlighted. (B) Red shading is presented indicating where the fractional intensity from the intact biosensor is most prevalent. (C) Highlighted in green are the areas in the cell where the fractional intensity of the cleaved biosensor is dominant in the image. As shown, these areas reside mostly on the edge of the cell. (D) Images (B) and (C) were then combined to form an image where the dominant fractional intensities of both configurations of the biosensor are highlighted together. (E) These scatter plots are projections of the pixels from the regions of interest in (A). Two lifetime pools near 2ns (regions 1 and 3) and 3ns (regions 2 and 4) are clearly visible.

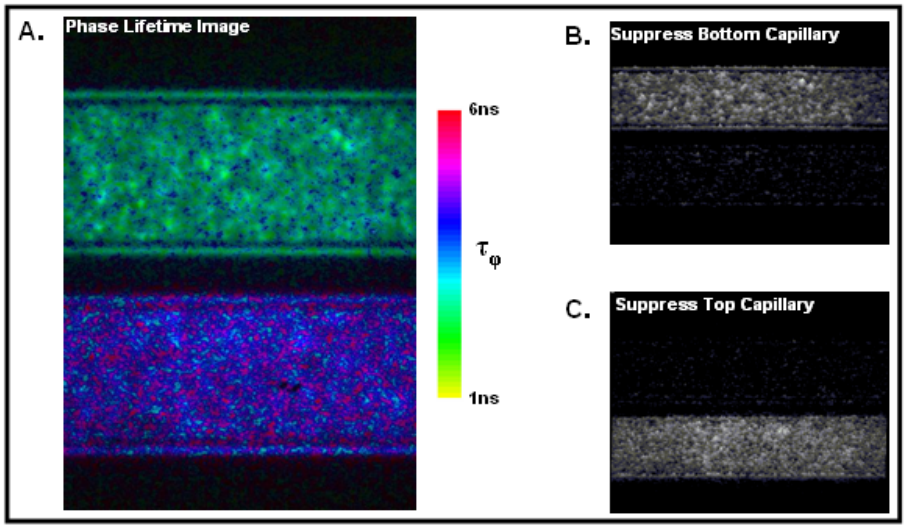

Figure 3.6: Simple example of phase suppression: (A) A lifetime image derived from the measured phase delays describes two micro-cuvettes containing Rhodamine B (top capillary) and Rhodamine 6G (bottom capillary). (B) Two detector phases were selected to suppress the intensity from the bottom capillary. The resulting difference image only contains intensities from the top capillary. (C) This difference image was generated by subtracting two images gathered at two separate detector phases (different from those applied in (B)) in order to suppress intensity from the top capillary.

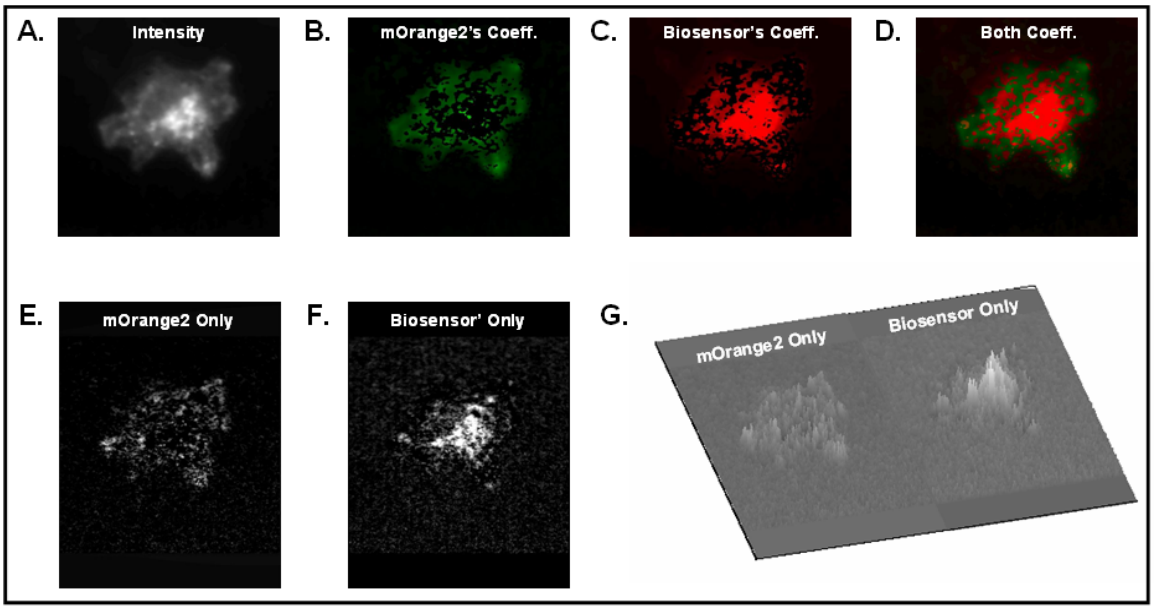

Figure 3.7: Analyzing a single HT-1080 cell with phase suppression: (A) This intensity image of an HT-1080 cell transfected with the MT1-MMP biosensor is the average of the eight phase images collected for a lifetime image. (B) The areas in the image where the majority of the intensity (based on a calculation from the polar plot), is being emitted from the cleaved biosensor are highlighted in green. (C) The areas in red specify the locations in the image where the intensity emitted from the intact biosensor is in the majority based on a calculation from the polar plot. (D) The images from (B) and (C) are combined to show the localization by intensity of both the intact and cleaved biosensor in the cell. (E) This difference image is the result of a subtraction of two images acquired at a set of detector phases selected to suppress the intensity from the intact biosensor. (F) The intensities in this image are the result of applying phase suppression to remove the intensity from the cleaved biosensor. (G) A three-dimensional rendering of the results from phase suppression shown in (E) and (F) is presented.

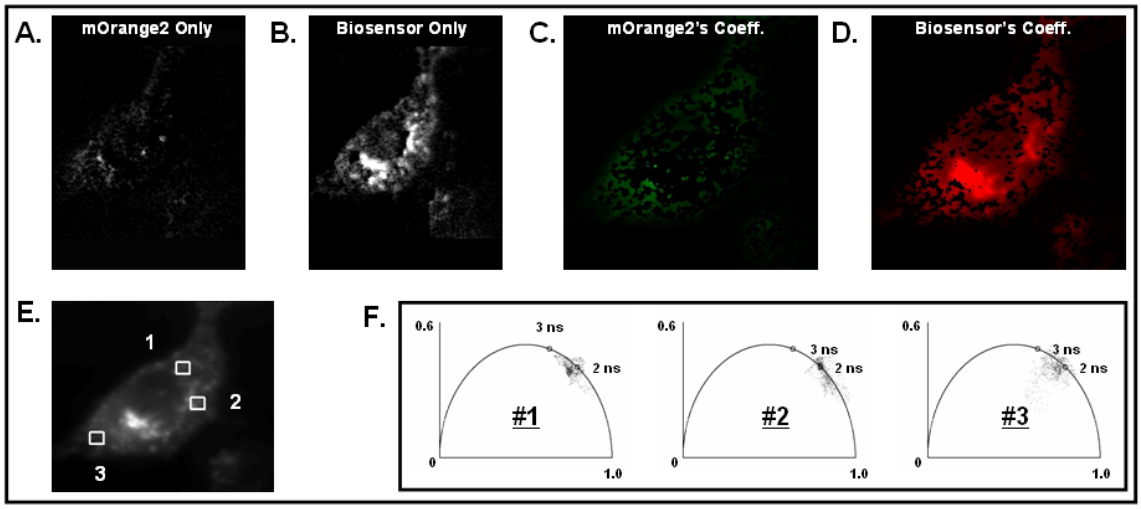

Figure 3.8: Phase suppression applied to study an HT1080 cell before the GM6001 inhibitor was washed out: (A) Phase suppression was applied to suppress the intensity from the intact biosensor in the image, leaving only intensity from the mOrange2 (cleaved biosensor). (B) A set of detector phase angles was also selected to suppress the intensity from the mOrange2 (cleaved biosensor). In this image, the result of that suppression strategy shows that the intact biosensor's fluorescence is being emitted from a majority of the cell's body. (C) A color coding masked by the intensity image in (E) has been applied to the image. The green shading in the various pixels indicates where in the cell the fractional intensity of the mOrange2 (cleaved biosensor) dominates the average intensity measured. (D) The pixels in which the fractional intensity is majority from the intact biosensor are colored in red. This image has been masked by the intensity image in (E). There is a similarity to the pixels shown here to the intensities highlighted in (B). (E) An intensity image of the cell is shown with three regions of interest indicated. (F) The pixels from each of the regions of interest in (E) are projected on the polar plot.

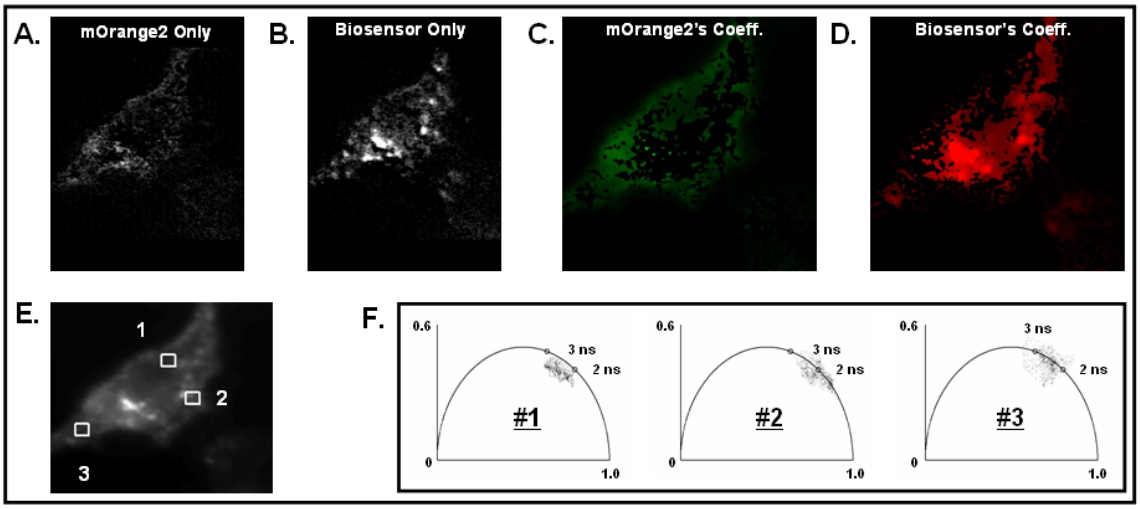

Figure 3.9: Analysis of an HT1080 cell with phase suppression thirty minutes after the GM6001 inhibitor was washed out: (A) Two detector phases were chosen and images were subsequently acquired to suppress the intensity from the intact biosensor. As shown, intensity remained from the mOrange2 (cleaved biosensor) primarily along the edge of the cell. (B) Phase suppression was also used to suppress the intensity of mOrange2 (cleaved biosensor). When performed, the intensity from the intact biosensor was found predominantly in the interior of the cell away from the edge. (C) Overlaid on the intensity image in (E) is a color coding describing the locations where the majority of the average intensity measured in the pixel comes from mOrange2 (cleaved biosensor). (D) Colored in red are the pixels in which the majority of the fractional intensity is from the intact biosensor. (E) An intensity image of the cell following the washout of GM6001 is shown along with three regions of interest indicated. (F). Three polar plots are shown in which the pixels from the regions of interest in (E) are displayed.

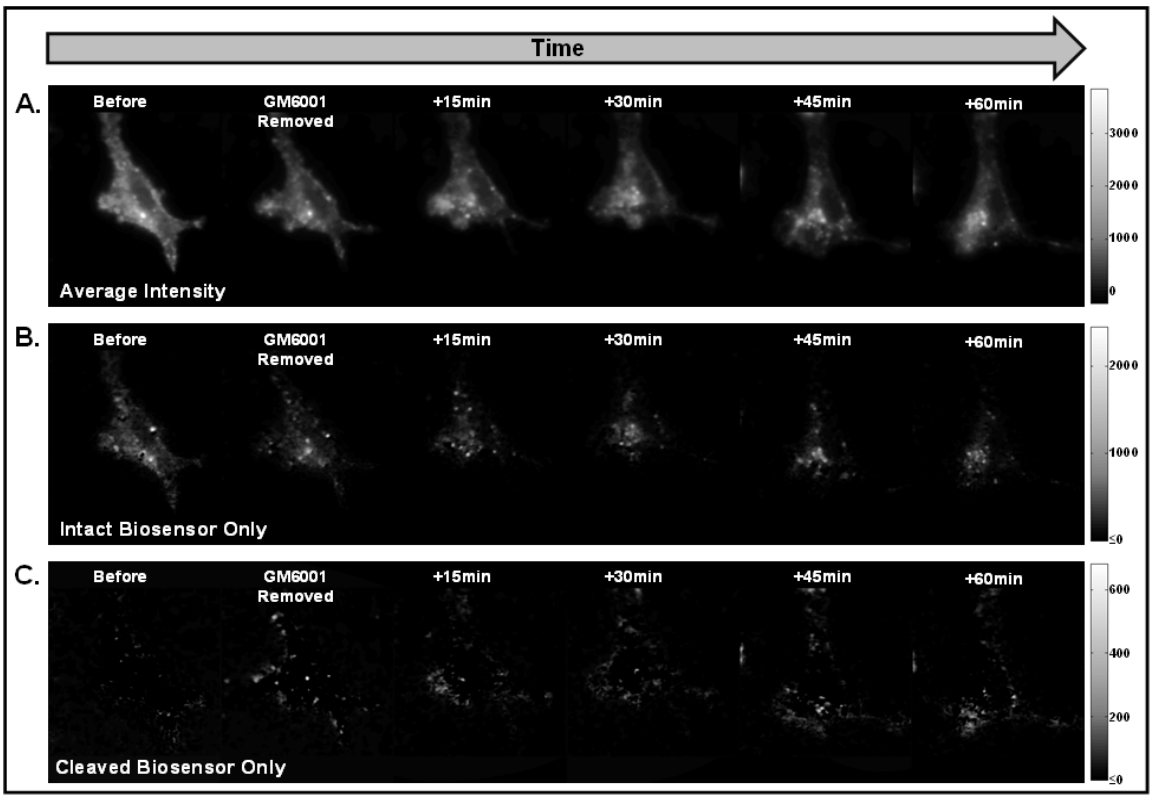

Figure 3.10: Improving the temporal resolution of phase suppression: (A) The intensity images show the morphological changes taking place before and at several time points after the inhibitor GM6001 was removed. (B) Two detector phases were selected to suppress the intensity from the cleaved biosensor. The resulting difference images indicate that the intensity from the intact biosensor remained primarily in the central portions of the cell throughout the experiment. (C) These difference images show that the intensity from the cleaved biosensor emerged along the perimeter of the cell and was specifically concentrated in the protrusion that formed along the lower left corner of the cell.

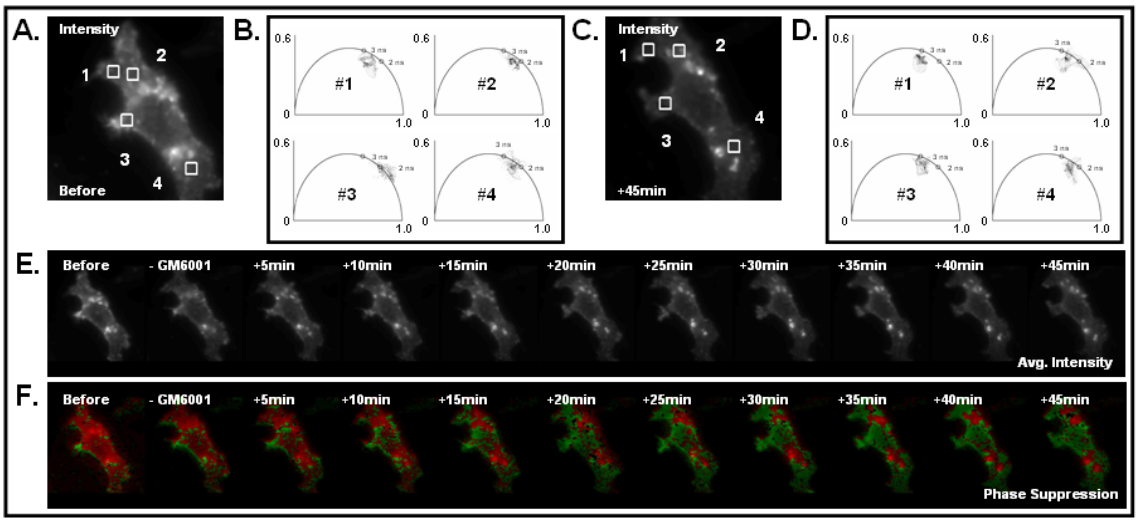

Figure 3.11: Time-lapsed imaging of HT-1080 cells on glass with phase suppression for forty five minutes: (A) This intensity image is the average of the eight phase images collected with the homodyne FLIM system before the MMP inhibitor GM6001 was removed. (B) The pixels from the four regions of interest in (A) are projected on the corresponding polar plots. Most of the polar coordinates are near 2ns likely indicating that the biosensor is intact. (C) The intensity image presented shows that the overall morphology of the cell did not significantly change forty five minutes after the GM6001 was removed from the cell's media. (D) The polar coordinates from the pixels in regions 1, 2 and 3 moved to a position closer to 3ns which implies that the biosensors in these areas are cleaved forty five minutes after the GM6001 was removed. (E) A set of average intensity images taken throughout the experiment with phase suppression are presented. (F) The results from the phase suppression are color-coded in order to describe the areas in the image where the intensity in the difference images are majority from the intact biosensor (red) or from the cleaved biosensor (green).

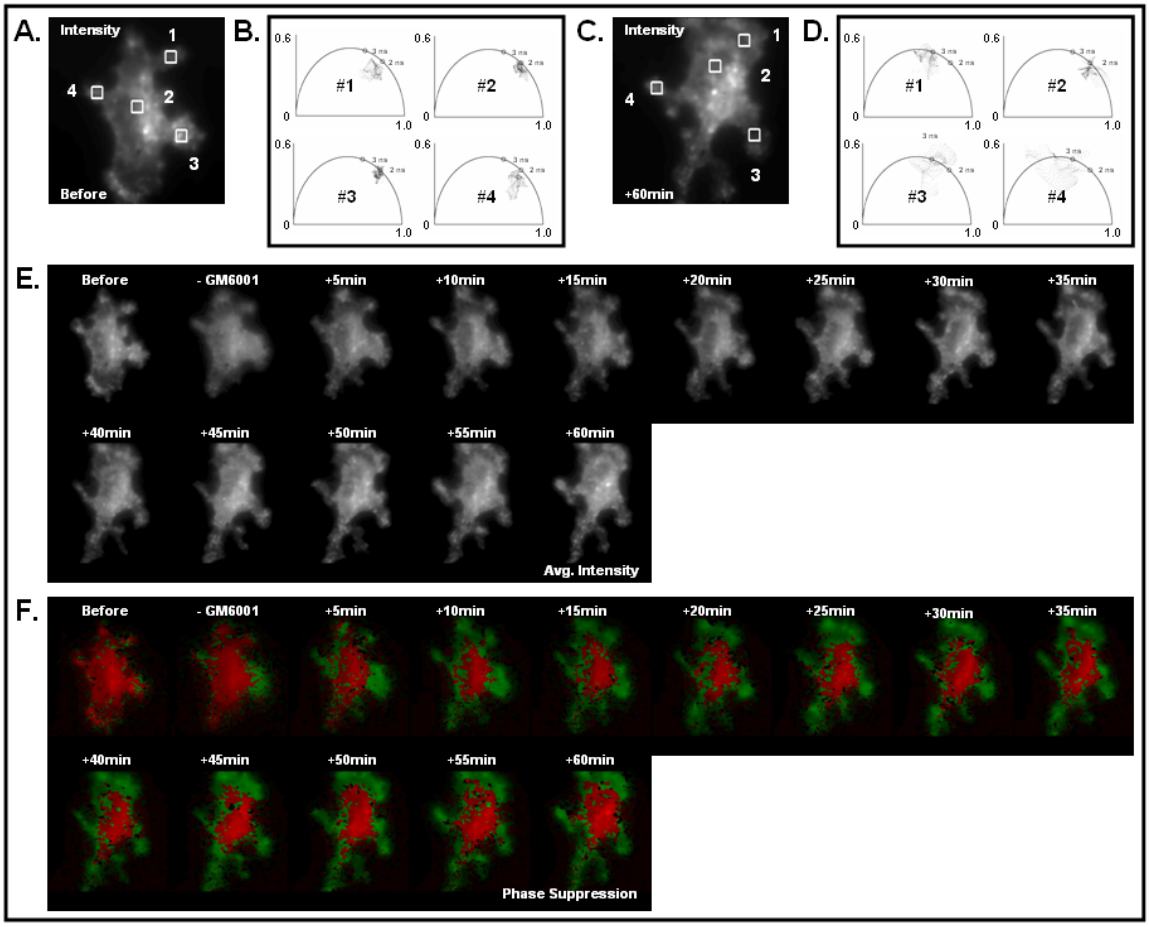

Figure 3.12: Time-lapsed imaging of HT-1080 cells on glass with phase suppression for a period of one hour: (A) Following the pre-treatment with GM6001, the intensity image of this HT-1080 cell clearly shows the nucleus and several extensions along the edge of the cell. (B) The polar coordinates corresponding to the pixels contained within the four regions of interest in (A) are projected near 2ns on the polar plot suggesting that the biosensor is initially intact. (C) As indicated by this intensity image, some morphological changes in the cell took place along the edge near the bottom and top of cell during the one hour experiment. Like (A), this intensity image is the average of the eight phase images acquired during the lifetime imaging experiment (D) In regions 1, 3 and 4, the polar coordinates from these pixels moved closer to the position associated with the cleaved biosensor (near 3ns) on the presented scatter plots. (E) By averaging the four intensity images acquired during the phase suppression experiment, these images describe the changes in the staining of biosensor at the times sampled. (F) The difference images highlighting the intensities from the cleaved biosensor and separately, the intact biosensor were combined with color code to spatially map the areas in the cell where the intact biosensor's intensity is in the majority (red) or where the cleaved biosensor's intensity is in the majority (green).

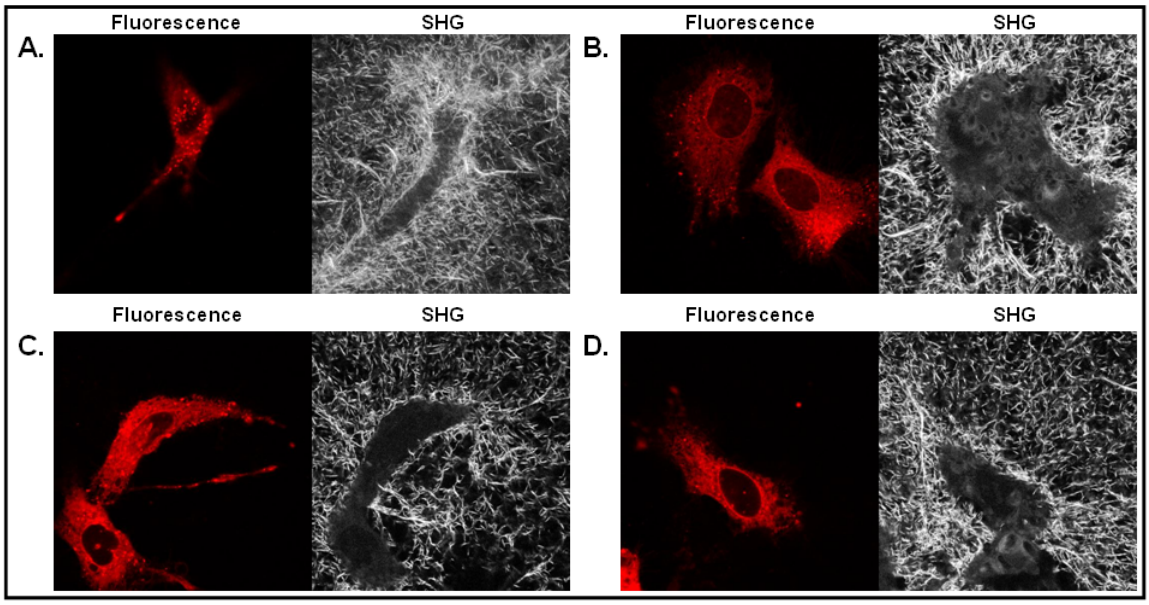

Figure 3.13: Steady-state imaging of transfected HT-1080 cells in a 3D matrix of collagen-I: (A-D) Images of four HT-1080 cells are presented. Images of the collagen-I collected with backwards second harmonic generation (SHG) were acquired in parallel with steady-state fluorescence images of the HT-1080 cells. In order to prevent the degradation of the collagen fibers, these cells were pre-treated with the MMP inhibitor GM6001.

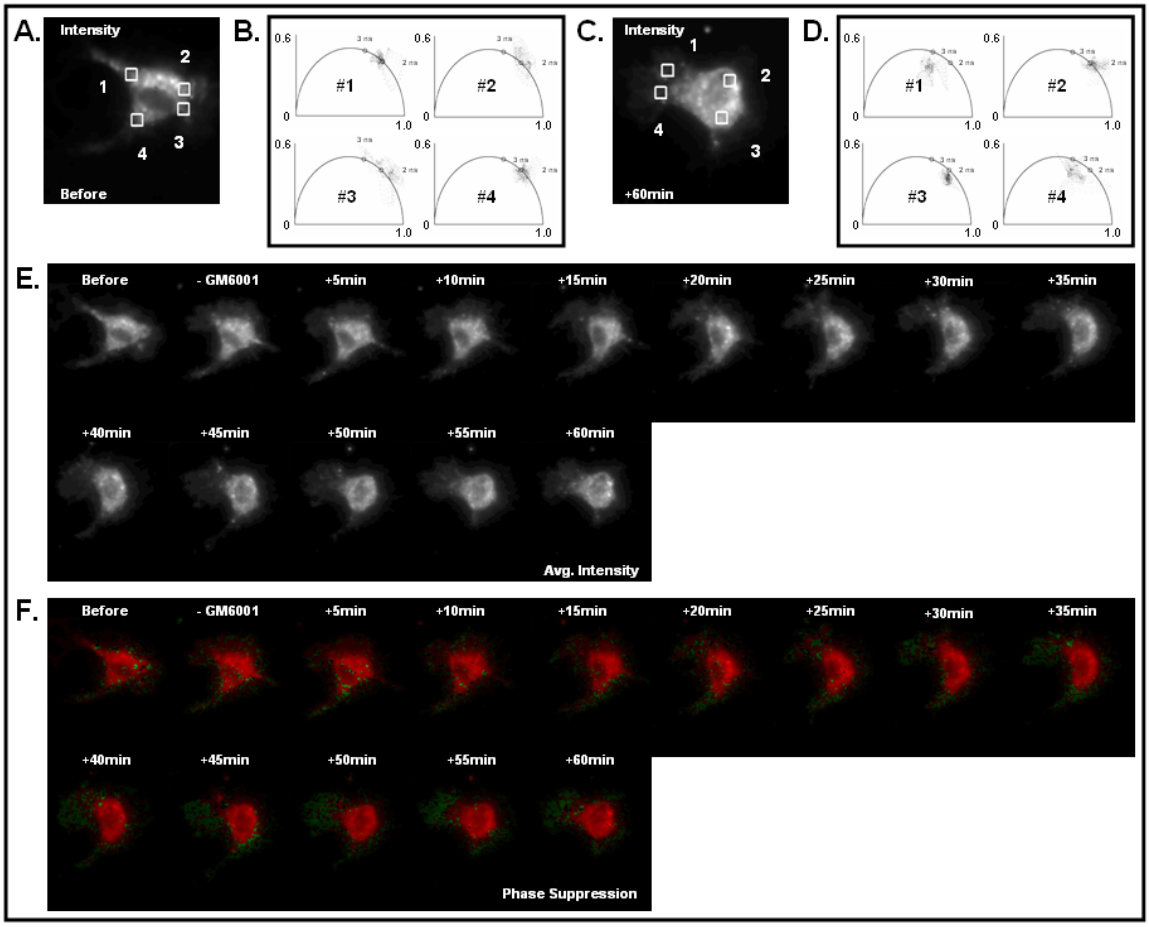

Figure 3.14: Activation of MT1-MMP in a live HT-1080 cell cultured in a 3-dimensional collagen matrix (1): (A) This intensity image was acquired after the HT-1080 cell was pre-treated with the MMP inhibitor for 12-18 hours prior to imaging. (B) The polar coordinates from the pixels in the four regions of interest in (A) are near the location of the intact biosensor (near 2ns) on the polar plot. (C) At a time of one hour after the removal of the MMP inhibitor GM6001, the morphology of the cell distinctly changed as shown in this intensity image generated by averaging the eight phase images acquired during lifetime imaging. (D) The polar coordinates near the left edge of the cell (regions 1 and 4 in (C)) moved to a position near 3ns one hour after the MMP inhibitor was removed likely indicating that the biosensor was cleaved. (E) Each intensity image shown is the average of the four intensity images acquired during phase suppression. (E) In these color-coded results from imaging with phase suppression (red – majority of intensity from intact biosensor, green – majority of intensity from cleaved biosensor), the cleaved biosensor emerged along the protrusions at the bottom and at the top left portions of the cell.

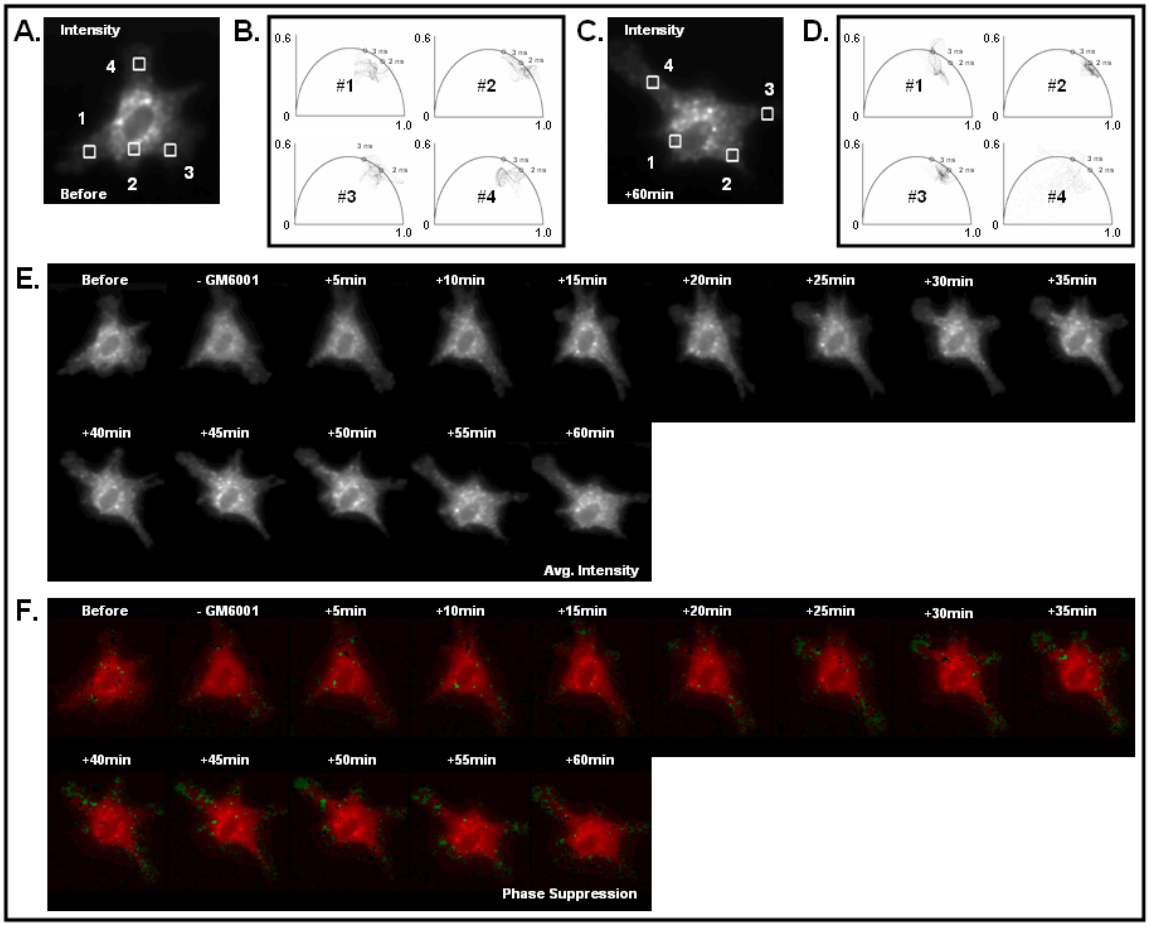

Figure 3.15: Activation of MT1-MMP in a live HT-1080 cell cultured in a 3-dimensional collagen matrix (2): (A) After being pre-treated with the MMP inhibitor, the average of the eight phase images acquired during the lifetime imaging was computed and shows the staining of the biosensor's plasmid, pDisplay. (B) When the pixels from the regions indicated in (A) are projected on the polar plot, the locations of the coordinates indicate that the biosensor is intact (near 2ns). (C) The fluorescent staining of the biosensor changed during the experiment, with new protrusions formed along the top and right side of the cell as shown in this intensity image. (D) At a time of one hour after the removal of the MMP inhibitor GM6001, the polar coordinates from the pixels in region 4 specifically moved toward longer lifetimes, suggesting the presence of the cleaved biosensor. (E) By averaging the four intensity images acquired for analysis with phase suppression, the presented intensity images show the change in overall morphology of the cell in time. (F) The intensities from the difference images containing the intensity from the cleaved and separately, from the intact biosensor, were combined and colored to show where the intensity from intact biosensor was dominant (red shading) and where the intensity from the cleaved biosensor was in the majority (green shading).

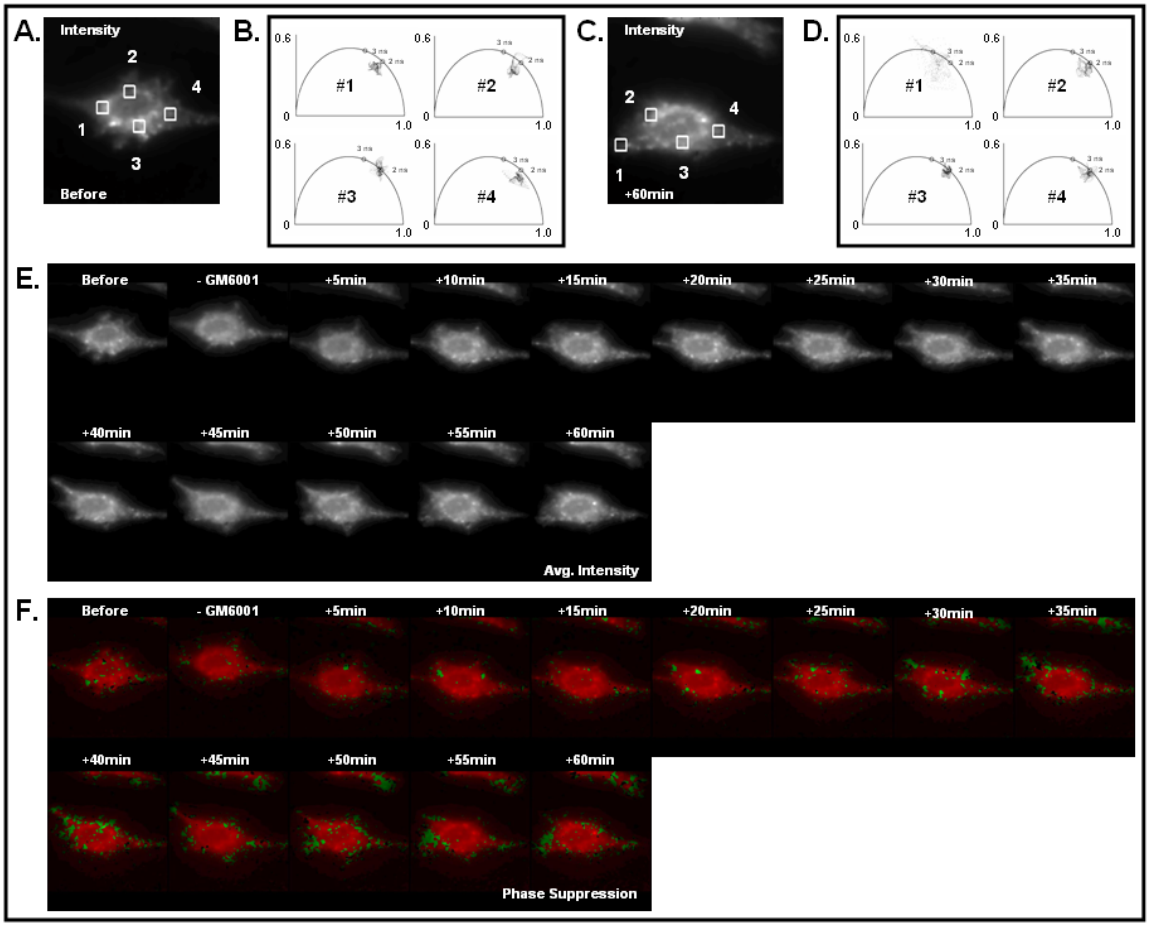

Figure 3.16: Activation of MT1-MMP in a live HT-1080 cell cultured in a 3-dimensional collagen matrix (3): (A) An HT-1080 cell transfected with the mOrange2/mCherry MT1-MMP biosensor was imaged with the homodyne FLIM system after being incubated with the MMP inhibitor GM6001 for 12-18 hours. (B) The polar coordinates corresponding to the four regions in (A) are projected on these scatter plots. Most of the polar coordinates are near 2ns suggesting that the biosensor is intact. (C) This intensity image is the average of the eight phase images acquired by the homodyne FLIM system one hour after the MMP inhibitor was removed. (D) Specifically in region 1 from (C), the polar coordinates indicative of this portion of the cell moved toward 3ns (cleaved biosensor) while the polar coordinates from the other regions (2-4) remained near 2ns (intact biosensor). (E) The staining of the MT1-MMP biosensor was monitored in time by averaging the four phase images collected during the experiment with phase suppression. (F) At the various time points sampled, the presented images are colored to show the areas in the combined difference images (combining the difference image containing intensity from the intact biosensor and separately the difference images containing intensity from the cleaved biosensor) where the majority of the intensity is from the intact biosensor (red) or from the cleaved biosensor (green).

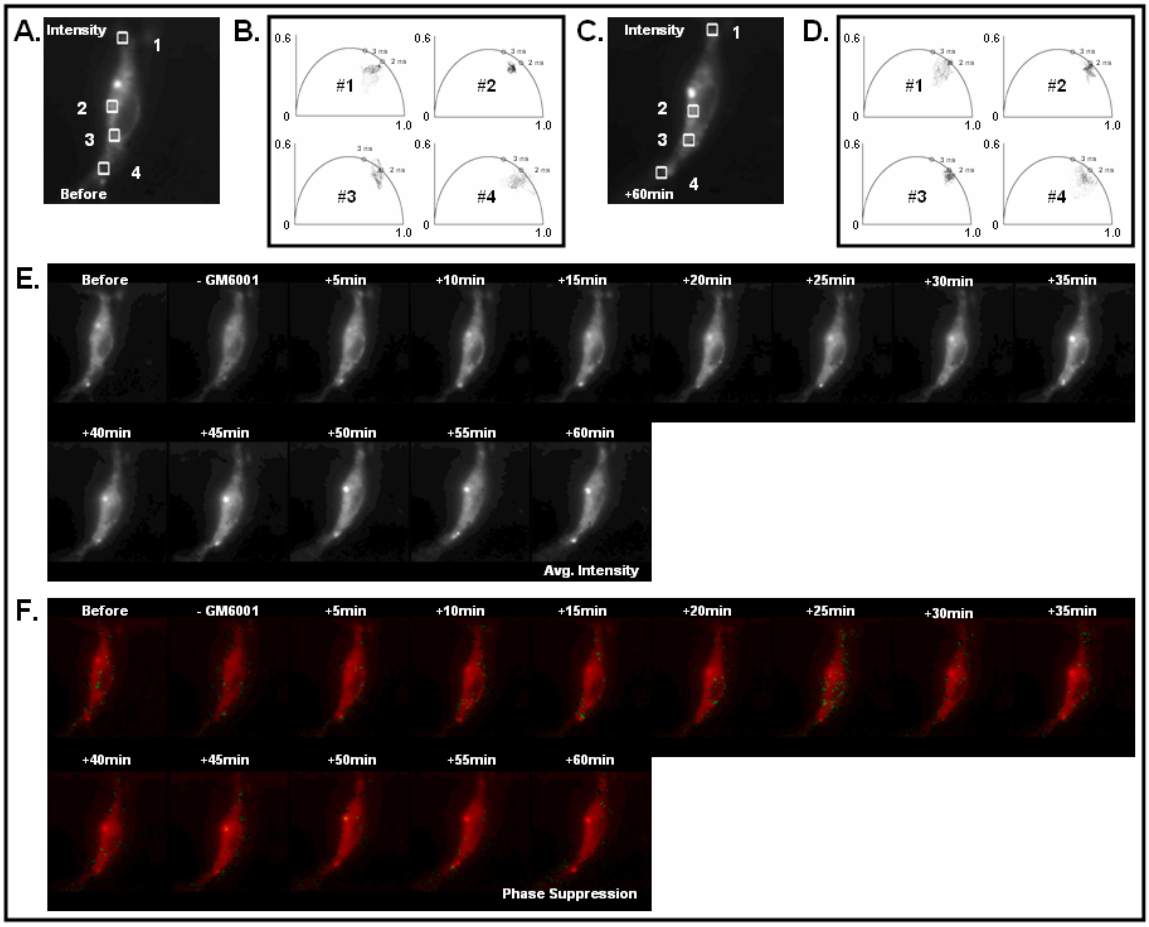

Figure 3.17: Lack of MT1-MMP's activation following the removal of inhibitors in live HT-1080 cells cultured in a 3-dimensional collagen matrix (1): (A) Before the MMP inhibitor GM6001 was removed, the intensity of the HT-1080 cell studied here showed that the cell was well spread (not rounded). (B) Throughout the cell, the polar coordinates corresponding to the pixels from the regions of interested highlighted in (A) were all projected near the location of the intact biosensor (near 2ns) on the polar plot. (C) One hour after the removal of the MMP inhibitor GM6001, some extensions were observed along the top and bottom of the cell as assessed by this intensity image. (D) Even without the presence of the inhibitors, the polar coordinates from the four regions studied within the cell remained near 2ns indicating that the biosensors were intact. (E) The staining of the cell by the biosensor was monitored in time by averaging the four intensity images collected during the imaging with phase suppression. (F) Intensities from the difference images indicative of the cleaved and intact biosensor are presented. Areas in the cell dominated in intensity emitted from the intact biosensor are colored in red and separately, locations in the cell containing intensity mostly from the cleaved biosensor are colored in green.

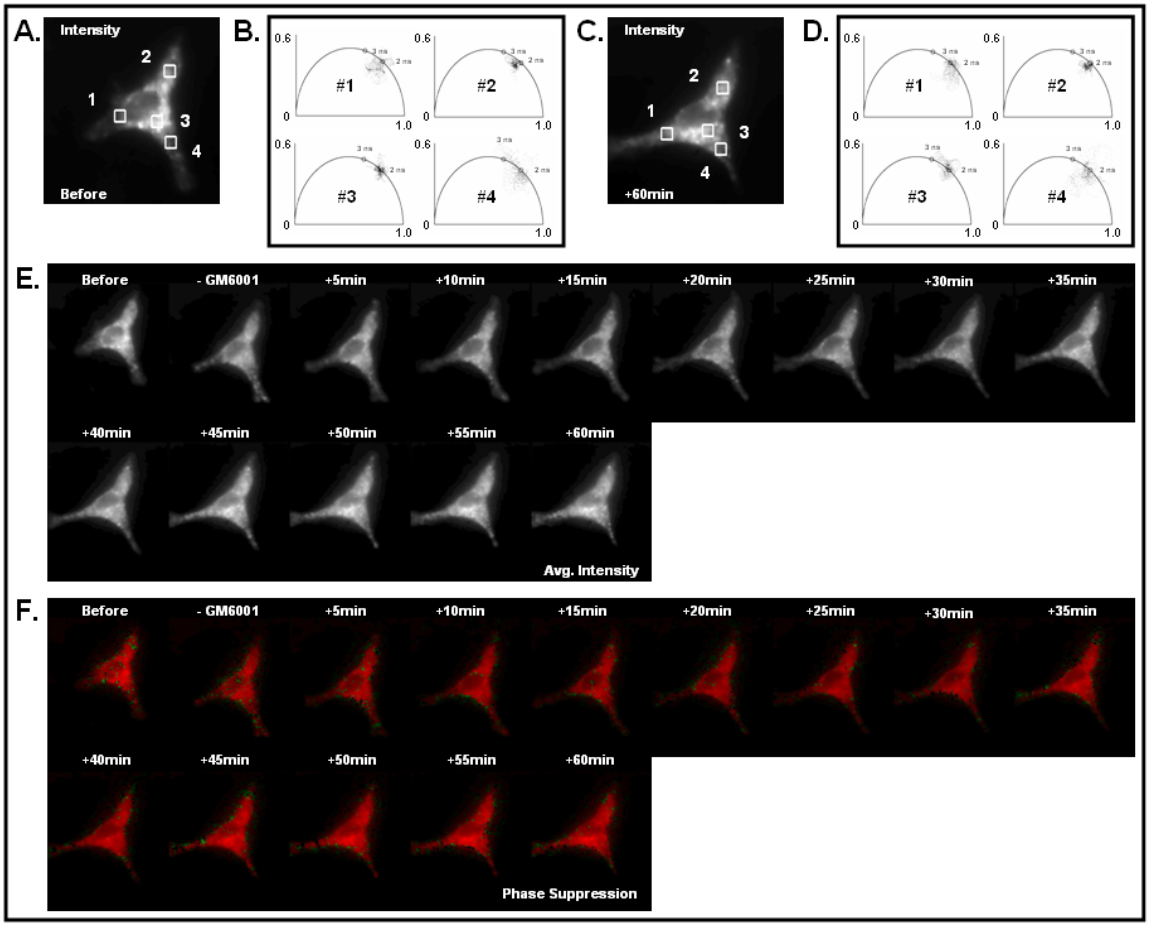

Figure 3.18: Lack of MT1-MMP's activation following the removal of inhibitors in live HT-1080 cells cultured in a 3-dimensional collagen matrix (2): (A) An intensity image shows an HT-1080 pre-treated with MMP inhibitors and cultured in a 3-dimensional collagen matrix. The average of the eight phase images collected during lifetime imaging were used to generate this image. (B) The polar coordinates calculated from pixels in regions selected throughout the cell suggest that the biosensor is likely intact before the inhibitor was washed away. (C) Approximately one hour after the MMP inhibitor was removed, this intensity image indicates that the morphology of the cell did change during the experiment. (D) Even along the bottom of the cell where some extension was noted, all polar coordinates in the regions analyzed within this cell's image remained near 2ns at a time one hour after the inhibitor was removed. (E) The average intensity emitted by the biosensor was tracked in time by averaging the four phase images acquired when applying phase suppression to study the cells. (F) The difference images calculated during the examination of the cells with phase suppression are presented with a color-coding highlighting areas within the cells dominated in intensity by either the intact biosensor (red) or the cleaved biosensor (green).

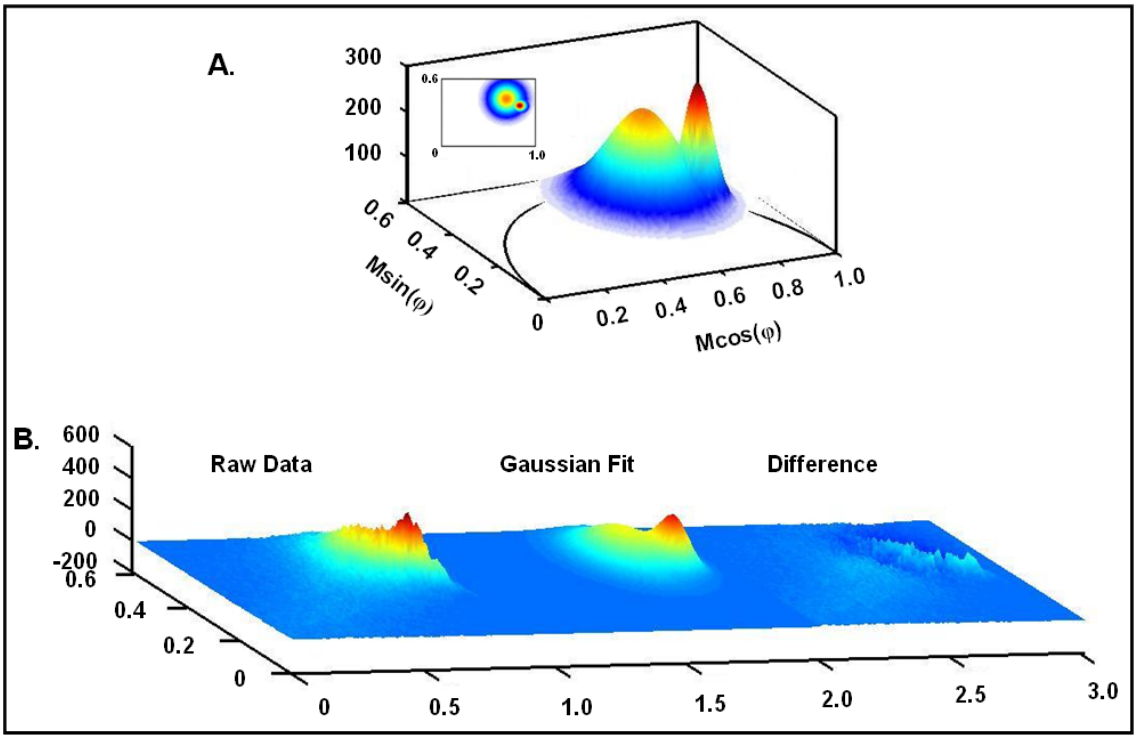

Supplemental Figure 3.1: Gaussian Fitting Applied to the Polar Plot: (A) The two Gaussians functions derived from the 3D histograms of polar coordinates of the HT-1080 cells transfected with the MT1-MMP biosensor (No GM6001) are plotted separately on the polar plot. The smaller distribution corresponds to the intact biosensor occurring mostly at regions of high intensity within the cells while the larger distribution corresponds to the cleaved biosensor. The inset in the top left corner displays a 2D projection of the 3D distribution. (B) The sum of the two Gaussians computed by fitting the histograms on the polar plot (left-most panel) is compared to the data (center panel). The difference between the actual measured polar coordinates inside the HT-1080 cells displayed as a 3D histogram and the Gaussian fits is shown in the panel on the far-right.

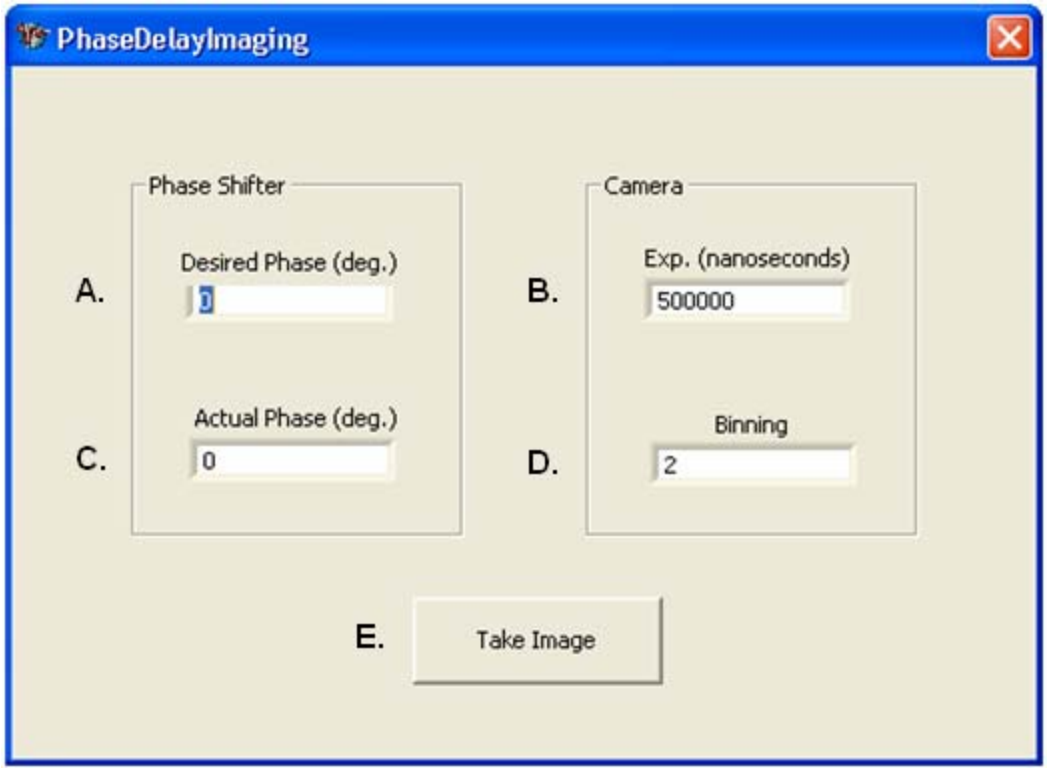

Supplemental Figure 3.2: PhaseDelayImaging Software: (A) This dialog box accepts the user's desired phase as input (B) The exposure time of the camera can be continuously changed by a simple input from the user. (C) The actual phase outputted by the digital phase shifter is presented in this box. The precision of the phase shifter is $\pm 0.7^{o}$. (D) The binning of the individual wells on the CCD chip can also be adjusted easily by the user depending on the needs of the experiment. (E) With the parameters from A-D inputted, this push button sends the commands to control the various components of the instrument and acquires an image. Following the acquisition of the image, the windows-based dialog appears to specify a filename and directory to save the image.

Tables

#cells	x_1 center	y_1 center	x_1 std. dev.	y_1 std. dev.	x_2 center	y_2 center	x_2 std. dev.	y_2 std. dev.	R^2
5	0.679	0.4565	0.111	0.0897	0.3948	0.2626	0.2337	0.2639	0.964
6	0.672	0.4421	0.118	0.1028	0.8293	0.3625	0.04082	0.03304	0.928
7	0.671	0.4352	0.113	0.0938	0.8201	0.368	0.04275	0.03359	0.92
8	0.671	0.4312	0.113	0.0952	0.8156	0.3701	0.04479	0.03244	0.923
9	0.674	0.4356	0.105	0.0848	0.8147	0.3702	0.04436	0.03253	0.912
10	0.675	0.4272	0.105	0.0871	0.8132	0.3674	0.04475	0.03215	0.918

Table 3.1: Gaussian fitting on the polar plot applied to HT-1080 cells not treated with GM6001: The polar coordinates determined using the modulation ratios and phase delays taken from the pixels within the HT-1080 cells containing the MT1-MMP biosensor were binned in a 3-dimensional histogram on the polar plot. The results from fitting the data with two Gaussian functions are indicated as a function of the number of cells examined. The centers of the fitted distributions, the corresponding standard deviations and fit parameters are shown.

References

1. J.P. Eichorst, et al., Phase differential enhancement of FLIM to distinguish FRET components of a biosensor for monitoring molecular activity of Membrane Type 1 Matrix Metalloproteinase in live cells. J Fluoresc. **21**(4). 1763-77.
2. J.W. Borst, et al., ATP changes the fluorescence lifetime of cyan fluorescent protein via an interaction with His148. PLoS One. **5**(11). e13862.
3. M. Jose, et al., (2007), Photophysics of Clomeleon by FLIM: discriminating excited state reactions along neuronal development. Biophys J. **92**(6). 2237-54.
4. M. Millington, et al., (2007), High-precision FLIM-FRET in fixed and living cells reveals heterogeneity in a simple CFP-YFP fusion protein. Biophys Chem. **127**(3). 155-64.
5. M.A. Elsliger, et al., (1999), Structural and spectral response of green fluorescent protein variants to changes in pH. Biochemistry. **38**(17). 5296-301.
6. J.P. Eichorst, R.M. Clegg, and Y. Wang, Red-shifted fluorescent proteins monitor enzymatic activity in live HT-1080 cells with fluorescence lifetime imaging microscopy (FLIM). J Microsc. **248**(1). 77-89.
7. N.C. Shaner, et al., (2008), Improving the photostability of bright monomeric orange and red fluorescent proteins. Nat Methods. **5**(6). 545-51.
8. N.C. Shaner, et al., (2004), Improved monomeric red, orange and yellow fluorescent proteins derived from Discosoma sp. red fluorescent protein. Nat Biotechnol. **22**(12). 1567-72.
9. J. Goedhart, et al., (2007), Sensitive detection of p65 homodimers using red-shifted and fluorescent protein-based FRET couples. PLoS One. **2**(10). e1011.

10. R.M. Clegg, (1992), Fluorescence resonance energy transfer and nucleic acids. Methods Enzymol. **211**. 353-88.

11. T. Förster, (1948), Zwischenmolekulare Energiewanderung und Fluoreszenz. Annalen der Physik. **437**(2). 55-75.

12. T. Förster, (1948), Intermolecular energy migration and fluroescence. Ann. Phys.. **2**. 55-75.

13. T. Förster (1951) *Fluoreszenz Organischer Verbindungen*, Vandenhoek & Ruprecht, Göttingen, Germany.

14. P. Schneider and R.M. Clegg, (1997), Rapid acquisition, analysis and display of fluorescence lifetime-resolved images for real-time applications. Reviews of Scientific Instrumentation. **68**(11). 4107-4119.

15. B.Q. Spring and R.M. Clegg, (2009), Image analysis for denoising full-field frequency-domain fluorescence lifetime images. J Microsc. **235**(2). 221-37.

16. T.W. Gadella, Jr., T.M. Jovin, and R.M. Clegg, (1993), Fluorescence lifetime imaging microscopy (FLIM): Spatial resolution of microstructures on the nanosecond time scale. Biophysical Chemistry. **48**. 221-239.

17. T.V. Veselova and V.I. Shirokov, (1972), A spectral fluorometric study of the luminescence of exiplexes of 3-amino-AT-methylphthalimide with acetone, pyridine, and dimethylformamide. Iz. Akad. Nauk SSSR Ser. Fiz. **36**. 1024.

18. T.V. Veselova, A.S. Cherkasov, and V.I. Shirokov, (1970), Fluorometric method for individual recording of spectra in systems containing two types of luminiscent centers. Optical Spectroscopy. **29**. 617-618.

19. J.R. Lakowicz and H. Cherek, (1981), Phase-sensitive fluorescence spectroscopy: a new method to resolve fluorescence lifetimes or emission spectra of components in a mixture of fluorophores. J Biochem Biophys Methods. **5**(1). 19-35.

20. J.R. Lakowicz and K.W. Berndt, (1991), Lifetime-selective fluorescence imaging using an rf phase-sensitive camera. Reviews of Scientific Instrumentation. **62**(7). 1727-1734.

21. J.R. Lakowicz and H. Cherek, (1982), Resolution of Heterogeneous Fluorescence by Phase-sensitive Fluorescence Spectroscopy. Biophys J. **37**(1). 148-150.

22. R.M. Clegg and P.C. Schneider, *Fluorescence Lifetime-Resolved Imaging Microscopy: A General Description of Lifetime-Resolved Imaging Measurements*, in *Fluorescence Microscopy and Fluorescent Probes*, J. Slavik, Editor. 1996, Plenum Press: New York. p. 15-33.

23. Q.S. Hanley, et al., (2001), Fluorescence lifetime imaging: multi-point calibration, minimum resolvable differences, and artifact suppression. Cytometry. **43**(4). 248-60.

24. M. Ouyang, et al., Simultaneous visualization of protumorigenic Src and MT1-MMP activities with fluorescence resonance energy transfer. Cancer Res. **70**(6). 2204-12.

25. Y. Wang, et al., (2005), Visualizing the mechanical activation of Src. Nature. **434**(7036). 1040-5.

26. H. Tsurui, et al., (2000), Seven-color fluorescence imaging of tissue samples based on Fourier spectroscopy and singular value decomposition. J Histochem Cytochem. **48**(5). 653-62.

27. C.B. Raub, et al., (2007), Noninvasive assessment of collagen gel microstructure and mechanics using multiphoton microscopy. Biophys J. **92**(6). 2212-22.

28. M.A. Digman, et al., (2008), The phasor approach to fluorescence lifetime imaging analysis. Biophys J. **94**(2). L14-6.

29. C. Buranachai, et al., (2008), Rapid frequency-domain FLIM spinning disk confocal microscope: lifetime resolution, image improvement and wavelet analysis. J Fluoresc. **18**(5). 929-42.

30. S.G. Mallat, (1989), A Theory fo Multiresolution Signal Decomposition: The Wavelet Representation. IEEE Transactions on Pattern Analysis and Machine Intelligence. **11**(7). 674-692.

31. R.M. Willet and R.D. Nowak, (2004), Fast multiresolution photon-limited image reconstruction. IEEE International Symposium on Biomedical Imaging. **2**. 1192-1195.

32. M. Ouyang, et al., (2008), Visualization of polarized membrane type 1 matrix metalloproteinase activity in live cells by fluorescence resonance energy transfer imaging. J Biol Chem. **283**(25). 17740-8.

33. M.H. Zaman, et al., (2006), Migration of tumor cells in 3D matrices is governed by matrix stiffness along with cell-matrix adhesion and proteolysis. Proc Natl Acad Sci U S A. **103**(29). 10889-94.

34. K. Hotary, et al., (2006), A cancer cell metalloprotease triad regulates the basement membrane transmigration program. Genes Dev. **20**(19). 2673-86.

35. F. Sabeh, et al., (2004), Tumor cell traffic through the extracellular matrix is controlled by the membrane-anchored collagenase MT1-MMP. J Cell Biol. **167**(4). 769-81.

36. K. Wolf, et al., (2003), Compensation mechanism in tumor cell migration: mesenchymal-amoeboid transition after blocking of pericellular proteolysis. J Cell Biol. **160**(2). 267-77.

37. J. Huisken, et al., (2004), Optical sectioning deep inside live embryos by selective plane illumination microscopy. Science. **305**(5686). 1007-9.

38. M. Vilela, et al., Fluctuation analysis of activity biosensor images for the study of information flow in signaling pathways. Methods Enzymol. **519**. 253-76.

39. E. Hinde, et al., Millisecond spatiotemporal dynamics of FRET biosensors by the pair correlation function and the phasor approach to FLIM. Proc Natl Acad Sci U S A. **110**(1). 135-40.

Chapter 4

Educational Research

Abstract

In collaboration with Prof. Robert Clegg, a portion of my graduate studies have been dedicated to developing new experiments and resources for advanced undergraduates and graduate students working through the Physics 552 (Optical Spectroscopy) course. Over the span of four offerings of the course, we had the opportunity to continually evaluate the response of students to the laboratories in the course and also make changes necessary to facilitate their understanding of various topics. The underlying theme of this work was two-fold: (1) Design simple experiments that would convey the fundamentals of lifetime imaging. (2) Develop experiments to introduce the students to advanced topics with research-grade fluorescence instruments such as spectral unmixing, phosphorescence and time-resolved anisotropy. In this chapter, I have provided the labs that I developed and wrote. My colleague Kai Wen Teng contributed to the experimental section in the lab that examines phosphorescence.

Phosphorescence Lab

Introduction

In this lab, you will be examining the photophysical characteristics of the dye Acridine Orange by combining many of the concepts and procedures that you have learned throughout the course. In addition, we will look at ways to measure the phosphorescence of Acridine Orange and examine applications of how both its fluorescence and phosphorescence emission can be used to study complex biological systems.

Background

Acridine Orange itself is a weak base and therefore, can easily enter and stain living mammalian cells. The staining of Acridine Orange is specifically targeted for intracellular structures containing DNA such as nucleoli. Although, Acridine Orange is well established as an effective DNA intercalator, evidence also suggests that Acridine Orange can weakly bind to the exterior of the DNA helix by weak electrostatic interactions. As an intercalator, Acridine Orange has been shown to both stack and form clusters when bound to DNA.

The benefit of using Acridine Orange as a stain is that the fluorescence and phosphorescence emission can provide information about the types of structures that the dye is bound to as well as indications about its local environment. In solution, Acridine Orange can be mainly characterized by green fluorescence with a lifetime near 1.7ns-1.9ns. When Acridine Orange forms dimers or higher order aggregates (on DNA for example), a strong red fluorescence can be observed. The lifetime of the red fluorescence of Acridine Orange has been reported to be between 5ns and 20ns depending on the extent of aggregation. Interestingly, in the absence of oxygen, red phosphorescence emission (>590nm) has also been observed both in vitro and in live cells with lifetimes on the order of milliseconds. Thus far, the phosphorescence has only been observed in areas of the cell primarily characterized by green fluorescence.

Despite the uncertainty that still remains about the staining of Acridine Orange in live samples, an understanding of the phosphorescence emission can potentially allow for extremely high contrast imaging of specific cellular features (especially when combined with fluorescence imaging).

Thus far, the majority of the course has been spent examining energy transitions between the singlet states in our molecules to measure fluorescence spectra and lifetimes. In any molecule that we studied previously and also in the Acridine Orange that we are currently measuring, the energy levels that an electron can occupy can be characterized (for the most part!) by several basic properties including the electronic energy, vibrational energy, rotational energy and spin. In short, the difference in the transitions between the singlet states that we have been studying and those with triplet states that lead to phosphorescence emission stems from the different spin configurations in the singlet and triplet states. All singlet states in this hypothetical molecule contain electrons with opposite spins whereas triplet states contain electrons with parallel spins.

Phosphorescence emission typically requires the transition from an excited singlet state to the triplet state by a pathway called intersystem crossing. This sort of transition is very often the result of a transition between two vibrational energy levels (having the same energy – isoenergetic) from electronic states of different multiplicities. This is technically a forbidden transition. However, a process called spin-orbit coupling makes this transition possible by essentially flipping the spin of the electron. Spin-orbit coupling requires an interaction of the orbital angular momentum of the outer electrons with the spin of the excited electron to facilitate the spin flip.(There is also a nice intuitive analogy on the bottom of page 30 in Valeur discussing spin-orbit coupling).

In order to observe the phosphorescence emission of Acridine Orange, all oxygen in solution must be removed by an oxygen scavenging agent. In this lab, we will be using the enzyme Glucose Oxidase for oxygen removal. Oxygen quenches the emitted phosphorescence by non-radiative energy transfer from the excited triplet state (Please see Lakowicz for examples). Therefore, lots of oxygen in solution (or in your cell) will significantly reduce the intensity of the phosphorescence emission and shorten the lifetime of your phosphorescence decay. When studying Acridine Orange, the intensity from the phosphorescent emission can be greatly increased also by cooling the sample particularly to liquid nitrogen temperatures (77K). Low temperatures significantly inhibit the diffusion of oxygen in solution, which then leads to an increase in the phosphorescent emission as a result of limited oxygen quenching.

In this lab, we will be using the Prof. Clegg's steady-state fluorometer combined with an attachment to measure steady-state phosphorescence (Figure 4.1). The phosphorescence attachment consists of two primary components: (1) the internal rotating cylinder (2) the outer holder which mounts to the fluorometer. The outer holder (2) has windows which resemble slits cut into it for the excitation light to enter and the emission to leave at 90^{o} relative to the excitation through either the left or right emission channel. The windows cut into (2) remain fixed throughout the experiment. The internal cylinder (1) has only two windows cut into it which are 180^{o} apart.

This phosphorescence attachment functions to see the light emitted from the sample at some time after the excitation light has been incident on it. This is accomplished by the fast rotation of the internal cylinder (1). As this cylinder turns, one window will allow for the brief excitation of the sample. As this window continues to rotate after the excitation event, it will pass between the sample and the detector. If the time between the excitation and the moment when the window passes between the sample and detector are on the approximate order of the phosphorescence lifetime of the sample, the detector will observe photons from phosphorescence. Although only a single window was discussed here from component (1), the same logic would follow also for the second window. This particular attachment allows one to continuously adjust the speed of rotation so that a wide range of phosphorescence lifetimes can be measured.

A definite advantage of this measurement is that all light from the excitation channel can be completely blocked which eliminates the need for any emission filter to detect the phosphorescence emission.

Experiments

Recording Fluorescence Spectrum

Acridine Orange Spectrum

1. Pipet the following into a 1 mL cuvette:
   - 530 uL of PBS (Phosphate buffered saline)
   - 14 uL of Acridine Orange stock. (5.7 OD)

2. Take an emission spectrum of the sample using the user-defined setting *Acridine Orange***.**

Acridine Orange on DNA Spectrum

1. Pipet the following into a 1 mL cuvette:
- 500 uL of PBS.
- 30 uL of DNA stock (100 OD)
- 14 uL of Acridine Orange stock.

2. Take an emission spectrum of the sample using the user-defined setting *Acridine Orange DNA*.

3. Do not discard the content of the cuvette

Intensity Measurements with Phosphorescence Attachment

First we must remove the sample holder from the PC1 fluorometer, and replace it with the SLM phosphorescence attachment. Your TA will assist you with this procedure.

Acridine Orange on DNA Intensity Measurement (Control)

1. Place your 1mL cuvette containing the Acridine Orange and DNA sample into the center of the phosphorescence attachment

2. Begin measuring intensity vs. time using the user-defined method *Phosphorescence Intensity.*

   -Please also have your TA increase the slit sizes on both monochromators, remove polarizers and place a filter in the emission channel. (Removing the polarizers increases the signal/noise and the emission filter prevents reflections from reaching detector).

-Please also turn the lights off and cover the sample chamber with a dark cloth.

3. After 30 seconds of measurements, activate the phosphorescence attachment. Record the intensity for 30 seconds with the phosphorescence attachment on. Repeat step 3. That is, you should have 120 seconds of data where 0-30sec phosphorescence attachment is off, 30-60sec phosphorescence attachment is on, 60-90sec phosphorescence attachment is off and 90-120sec phosphorescence attachment is on.

Acridine Orange on DNA Phosphorescence Spectrum

1. Pipet the following into a clean 1 mL cuvette:
   - 443 uL of PBS.
   - 30 uL of DNA stock.
   - 14 uL of Acridine Orange stock.
   - 2 uL of catalase (the eppendorf labeled with c).
   - 6 uL of glucose oxidase (labeled with g).

   The enzymes for oxygen scavenging are now added; as soon as the substrates (dextrose) are added into the cuvette the deoxygenating reaction will begin. Prepare a stopper for the 1 mL cuvette and a strip of parafilm to quickly seal the cuvette as soon as we add dextrose in the next step.

2. Add 49 uL of dextrose and quickly seal the cuvette with stopper and wrap the stopper around with a parafilm.

3. Place the cuvette into the sample holder of the SLM phosphorescence attachment. Activate the phosphorescence attachment and turn the speed to 10.

4. Please select the user-defined method *Phosphorescence Spectrum*. Cover the sample holder with a dark cloth, turn off the lights in the room and hit start.

5. The oxygen scavenging agent takes some time to get rid of the oxygen. You will take another spectrum after 15 minutes. Please also take one last spectrum.

Acridine Orange on DNA Phosphorescence Intensity Measurement

1. Please select the user-defined method *Phosphorescence Intensity*

2. We will first inspect the phosphorescence intensity by turning the phosphorescence attachment on and off while running at the maximum speed.

Start the recording of the intensity with the phosphorescence attachment off, then turn the phosphorescence attachment on after 30 seconds. Repeat this procedure for a total of 120 seconds, that is a total of 4 on/off intervals.

3. Next, we will inspect the phosphorescence intensity as a function of spinning frequency. Select user-defined method *Phosphorescence and Frequency*. Activate the phosphorescence attachment, turn to maximum speed and begin data acquisition.

4. Starting with the maximum spinning frequency of 2 gradually decrease the spinning frequency by 0.2 every 30 seconds. (See table in appendix for actual spinning frequencies).

Demonstrating the Principle of Our Phosphorescence Detection

This experiment should be done in small groups while the spectra are being recorded from the previous experiments. In this experiment, there is a setup built behind the fluorometer that will demonstrate the principle of how we are detecting phosphorescence and the benefits of imaging with phosphorescence.

Setting up the System

1. Please take note of and make a sketch of the setup prior to beginning.

2. Please position both the ruby and the sample of rhodamine so that they can be imaged simultaneously by the camera through the opening in the chopper.

3. Connect the 'Sync" output located on the chopper's control box to the input of the frequency counter. Adjust the larger control dial located on the chopper's control box to achieve a chopping frequency of 100Hz.

4. Please re-connect the 'Sync' output from the chopper to the trigger input on the oscilloscope

Data Acquisition

1. Take note of the traces on the oscilloscope and identify the waveform driving the LED's intensity modulation and the waveform corresponding to the shuttering of the camera by the chopper.

2. Set of the phase of the frequency generator to 0^{o}. Please acquire and save an image of the sample on the desktop of the computer.

3. Repeat step (2) using phases of 45^{o}, 90^{o}, 135^{o} and 180^{o}. Monitor the traces on the oscilloscope as you change the phase of the function generator.

Questions

1. Correct your phosphorescence spectrum for unwanted background:

   First, determine the equation for the straight line extending from the beginning to the end of your spectrum.

   Subtract the background from spectrum. Your response to (1) should include the phosphorescence spectrum before the background subtraction and separately after the background subtraction

2. What causes the green peak that you see in your phosphorescence spectrum? If you measure the lifetime using the intensity from the green peak, will that measured lifetime be the same as the lifetime you would measure using the intensity from the red peak? Why?

3. We had asked the class to measure the intensity of the sample as a function of the spinning frequency of the phosphorescence attachment. This sort of experiment can allow you to measure the lifetime of your sample.

   In the appendix of Prof. Clegg's 1991 article (indicated on website and in (1)), he has the following equation describing the intensity measured by a detector using a phosphorescence device similar to the one applied in this lab.

$$\begin{aligned}
&\textbf{Integrated phosphorescence intensity} \\
&= k_p \cdot \int_{\Delta t}^{\Delta t + T_0} \text{Triplet}(\Delta t) \cdot d(\Delta t) \\
&= \left(\frac{k_p}{k_T}\right) \cdot \text{Triplet}_{ss} \cdot (1 - e^{-k_T T_0}) \cdot \left(\frac{1 - e^{-(R_T + k_T)T}}{1 - e^{-(R_T T + k_T T')}}\right) \cdot e^{-k_T \Delta t} \\
&= \left(\frac{\Phi_p \cdot G_0 \cdot k_G}{k_T}\right) \cdot (1 - e^{-k_T T_0}) \cdot \left(\frac{1 - e^{-(R_T + k_T)}}{1 - e^{-(R_T T + k_T T')}}\right) \cdot e^{-k_T \Delta t}, \qquad \text{(A6)}
\end{aligned}$$

   Please refer to Figure (1) in the reference (1) for a graphical definition of many of the variables shown above. (Please note that we have made a correction that does not appear in the paper.)

   . Please describe briefly why the intensity that you measured during this experiment increased as well increased the spinning rate of the phosphorescence attachment.

   Please plot the average intensity that you measured as a function of frequency.

There will be an excel file provided containing 11 intensity measurements taken at each speed of the phosphorescence attachment. Take the average of each of the 11 sets of intensities..

At the end of your calculations, you should have 11 intensity values and 11 frequencies. Please plot these (frequency on x-axis and average intensity on y-axis).

PLEASE JUST SUBMIT A PLOT FOR QUESITON #3. NO FITTING IS REQUIRED. BELOW ARE THE RESULTS OF THE TAs ONLY IF YOU ARE INTERESTED.

4. Present a simple schematic of the setup. In this experiment, what was the function of the frequency generator?

5. Please present the images acquired during the experiment. Along with the images, please sketch and label the corresponding scope traces for the driving voltage of the LED and the shuttering of the camera. (In other words, each image should be accompanied by a drawing of the two traces (camera shutter and LED) that were observed on the scope during the experiment).

Table 4.1: Frequency Table for Phosphorescence Attachment

Dial	Frequency (Hz)
0	27
0.2	34
0.4	41
0.6	47
0.8	53
1	59
1.2	64
1.4	70
1.6	75
1.8	80
2	85

Reference

[1] Marriott et al., " Time-resolved imaging microscopy. Phosphorescence and delayed luminescence imaging" Biophysical Journal Vol. 60 No. 6, pp 1374-1387, 1991

Lab: Anisotropy Decay (New Part Added to Anisotropy Lab)

Introduction

The polarized fluorescence emission of a fluorophore can relate detailed information about the rotational characteristics of a sample. In the previous section, we examined the steady-state anisotropy of a series of fluorescein both as a function of quenching (shortening of lifetime) and as a function of viscosity in the local environment. In both cases, an analysis based on the Perrin plot was able to yield rotational correlation times, viscosities and even lifetimes. Measuring the time-dependent anisotropy (anisotropy decay) is also a direct way to determine the lifetime, fundamental anisotropy and the rotational correlation time of a fluorophore in a specific sample. Measuring the anisotropy decay involves only a single sample and does not require a series of samples to extract physical information. However, as done in this lab, we will need to measure the time-dependent fluorescence of our sample at many modulation frequencies and hence it will be time consuming.

Background

In this experiment, you will be exciting the sample with vertically polarized light. The emission will be collected in the left emission channel which is perpendicular to the excitation channel. The emission polarizer will be rotated so that you can detect the fluorescent emission that is polarized both perpendicular $\left(I_{\perp}(t)\right)$ and parallel $\left(I_{||}(t)\right)$ relative to the excitation's polarization. If the sample is excited by a very short pulse of vertically polarized exciting light, the anisotropy decay is simply the time course of the anisotropy $r(t)$ shown below,

$$r(t)=\frac{I_{||}(t)-I_{\perp}(t)}{I_{||}(t)+2I_{\perp}(t)}$$

With this definition, the separately decaying intensities that are polarized perpendicular and parallel to the polarization of the exciting light can be written as,

$$I_{||}(t)=\frac{I_{\perp}(t)\left(1+2r(t)\right)}{1+r(t)}$$

$$I_{\perp}(t)=\frac{I_{||}(t)\left(1-r(t)\right)}{1+2r(t)}$$

In the cases studied today, the function $r(t)$ will decay as an exponential. Cases when the decay may be non-exponential include when quenching is taking place for example. However, the pre-exponential factor and the decay constant describe the fundamental anisotropy (r_o), lifetime (τ) and rotational correlation time (θ) as shown,

$$r(t)=r_o e^{-t/\theta}$$

If there are multiple fluorescent components in the sample being directly excited, the function $r(t)$ can be written as a sum where each component has a fundamental anisotropy and rotational correlation time each weighted in the sum by the corresponding fractional contribution to the steady-state intensity.

In the frequency domain, the sample will be excited with an intensity-modulated and polarized excitation light source. The goal in this experiment is related to the intensity-modulated polarized components of the sample's fluorescence emission to the physical parameters describing the fluorophore. The analysis stems from the convolution of the two polarized components of the fluorescence emission with the waveform of the exciting light. Therefore, each polarized component of the emission can be described as a sinusoidal function oscillating at the same frequency that the intensity of the exciting light is being modulated at. Likewise, there will be a phase delay and amplitude of oscillation associated with both polarized components of the emission. Unlike measuring lifetimes in the frequency domain, the phase delay and amplitude of oscillation detected for each polarized component is not compared to that of a known reference fluorophore. Instead, the differences in the measured phases $(\Delta\phi)$ and the ratio of the amplitudes of oscillation (Γ) taken from the two polarized components of the emission are calculated. As a result, all instrumental corrections for the phase delay and amplitude of oscillation cancel and no reference is needed.

In order to quantitatively relate $(\Delta\phi)$ and (Γ) to physical constants describing the sample, the amplitude of oscillating and phase delay need to be defined using Fourier analysis. At a specific frequency, the oscillating polarized components of the fluorescence emission can be expressed as a sum of sinusoidal functions each weighted by the corresponding sine and cosine transforms. The entire intensity-modulated fluorescence emission can be re-constructed if all frequencies of oscillation are considered. The sine and cosine transforms essentially indicating how much each frequency of oscillating contributes to the overall signal can be defined for a polarization (p) as follows,

$$N_p = \int_{t=0}^{\infty} I_p(t)\cos(\omega_E t)\,dt$$

$$D_p = \int_{t=0}^{\infty} I_p(t)\sin(\omega_E t)\,dt$$

The evaluation of these integrals is quite complicated and can be found in the accompanying reference to the lab. However, with a trigonometric identity, the amplitude of oscillation (M_P) and phase delay (ϕ_P) describing the polarized fluorescence emission at a polarization (p) are,

$$\phi_P = \tan^{-1}\left(\frac{N_P}{D_P}\right)$$

$$M_P = \sqrt{N_P^2 + D_P^2}$$

The difference in phase delay and the ratio of the amplitudes of oscillation measured from the two polarized components of the fluorescence emission are functionally dependent on the lifetime, fundamental anisotropy, frequency of oscillation and the rotational correlation time. They can be written as,

$$\Delta\phi = \tan^{-1}\left(\frac{D_{||}N_{\perp} - N_{||}D_{\perp}}{N_{||}N_{\perp} + D_{||}D_{\perp}}\right)$$

$$\Gamma = \left(\frac{N_{||}^{\,2} + D_{||}^{\,2}}{N_{\perp}^{2} + D_{\perp}^{2}}\right)^{1/2}$$

When all of the sine and cosine transforms are evaluated, the terms $(\Delta\phi)$ and (Γ) become complicated functions with dependencies on the modulation frequency (ω_E), the rotational correlation time (θ), the lifetime (τ) of the sample and the sample's fundamental anisotropy (r_o). Therefore, with iterative fitting of measurements of $(\Delta\phi)$ and (Γ) taken at multiple modulation frequencies, all the physical constants of the sample can be defined. A more concise description of the derivation provided here can be found in (1).

Experiment

1. Mount the 448nm laser diode behind the SLM's sample chamber. Please be careful and see your TA for assistance.

2. Align the diode so that there is plenty of light reaching the sample chamber to excite the sample. Insert the 448nm bandpass filter (small round filter) into the filter holder in the excitation channel.

3. Please prepare a solution of Fluorescein in a mixture of 50/50 water/glycerol in one of the large 4.5ml cuvettes and place it in the sample holder.

4. Please find the experiment located within the user-defined menu call "Fluor Anis Decay" and load it.

5. Please run the experiment and coordinate amongst your colleagues to operate the shutters and polarizer when instructed by the software. The data acquisition is automated here.

6. Before the experiment has concluded, please record the G-factor _____

Questions

1. Why do we not need use a reference (sample with known lifetime) to detect the anisotropy decay? We had to use a reference in the previous measurements in the frequency domain.

2. The software reported a lifetime of Fluorescein following the fitting. Does this value make sense? Why would the lifetime of fluorescein change in different solutions

3. Why are measurements at multiple frequencies necessary? Why did we not just extract the rotational correlation times, lifetime and fundamental anisotropy from a measurement at a single frequency?

Reference

[1] Lakowicz, J.R. et al., "Review of Fluorescence Anisotropy Decay Analysis by Frequency-Domain Fluorescence Spectroscopy" Journal of Fluorescence Vol. 3 No. 2, pp 103 – 115, 1993

Lab: Spectral Unmixing with Lifetimes (New Part Added to Quantitative Fluorescence Lab)

Introduction

For many experiments, it is necessary to visualize the dynamics of different fluorophores in a sample. However, the absorbance and emission spectra of many of the common fluorophores overlap and as a result, finding unique sets of excitation and emission wavelengths to distinguish each fluorophore may be difficult. Linear spectral unmixing is a technique that can follow changes in the emission of distinct fluorophores even if their spectra overlap. Computationally, the contributions of each fluorophore to the measured intensity can be determined using measured intensities taken at small wavelength intervals across the entire spectrum. When combined with concurrent measurements of the lifetime in the frequency domain, spectral unmixing can reveal detailed information about contributions of intensity from component fluorophores at various concentrations. In this lab, you will measure a sample containing Fluorescein and Rhodamine B in order to learn how to acquire a data set necessary for spectral analysis and how to unmix spectrum to extract component spectra. In parallel, the measured phase delay and modulation ratio will be projected on the polar plot in order to evaluate the spectral unmixing.

Background

The purpose of spectral unmixing is to determine the contribution of different fluorophores to a measured intensity. In other words, if the measured intensity is $I_{Meas}(\lambda_{Em})$ at an emission wavelength (λ_{Em}), the unmixing will reveal how much of that intensity is result of different fluorophores with overlapping spectra $(F_1(\lambda_{Em}), F_2(\lambda_{Em}), F_3(\lambda_{Em}), ...)$. As shown below, the contributions of the different fluorophores to the measured intensity are described by the coefficients (a_i).

$$I_{Meas}(\lambda_{Em}) = a_1 F_1(\lambda_{Em}) + a_2 F_2(\lambda_{Em}) + a_3 F_3(\lambda_{Em}) + \ldots +$$

In this lab, we will be measuring emission spectra for the unmixing calculations. Each spectrum can be considered as a single column matrix. As such, we will be using a matrix-based calculation to unmix our measured spectra. Please see the references for this lab for examples of iterative fitting algorithms that can also be used to unmix spectra. With a measured emission spectrum $[S_{Meas}]$ and a set of known spectra of the individual fluorescing components $[S_{REF}]$, the spectral unmixing determines the abundance vector $[a]$ which satisfies the following relationship,

$$[S_{Meas}] = [S_{REF}][a]$$

The abundance vector relates how much each individual spectrum in the reference matrix contributes to the measured spectrum. During the analysis in this lab, you will multiply both sides of the above equation by the inverse of the reference matrix in order to

determine the abundance vector (1). In the case of this lab where there are two fluorophores.

To begin the analysis, spectra need to be acquired of the component fluorophores in the mixture (referred to as reference spectra, $[S_{REF}]$). The matrix $[S_{REF}]$ is shown below as a function of emission wavelengths $(\lambda_1, \lambda_2, \lambda_3, ...)$.

$$[S_{REF}] = \begin{bmatrix} S_{FL}(\lambda_1) & S_{RhB}(\lambda_1) \\ S_{FL}(\lambda_2) & S_{RhB}(\lambda_2) \\ S_{FL}(\lambda_3) & S_{RhB}(\lambda_3) \\ . & . \\ . & . \\ . & . \end{bmatrix}$$

In order to accurately unmix the measured spectrum $[S_{Meas}]$, the reference spectra $[S_{REF}]$ must be collected under conditions similar to those of the sample (solvent, temperature, detector…). The abundance vector calculated for each spectral component of the reference matrix will therefore, be given with respect to the reference spectrum.

The reference matrix is not square and hence its inversion is not straight-forward. We will be finding a pseudo-inverse with singlular value decomposition (SVD). When the reference matrix $[S_{REF}]$ is decomposed by SVD, three matrices referred to as $[u]$, $[s]$ and $[v]$ are calculated. The pseudo-inverse of the reference matrix can then be calculated as,

$$[S_{REF}]^{-1} = v * \left[1/s \right]^{\dagger} * u^{\dagger}$$

Please remember that the matrix containing the singular values (s) has many zeros as elements when you go through the above calculation. Therefore, the abundance matrix can be then be as follows

$$[a] = [S_{REF}]^{-1} [S_{Meas}]$$

Experiment

Sample Preparation

1. Prepare a sample of pure Fluorescein in water using the provided stock (See TA for amounts to add). The solution should be prepared in the corning tube labeled "Fluorescein Student".

2. Prepare a sample of pure Rhodamine B n water using the provided stock. (See TA for amounts to add) The solution should be prepared in the corning tube labeled "Rhodamine Student"

Measuring Lifetimes

1. Load 1.5ml of the newly prepared solution of Fluorescein to one of the 4.5ml cuvettes. Place this sample in the position on the sample turret marked 's'

2. Load 1.5ml of the solution labeled "Fluorescein Reference" into a 4.5ml cuvette. This is Fluorescein in 0.1N NaOH with a lifetime of 4.3ns. Please load this into the sample turret in position 'r'

3. Please place the 570nm bandpass filter in the emission channel and verify that the PMT gain is set to 7.

4. Please configure the software with the following parameters and then run the lifetime measurement

   Integration Time = 5 seconds
   Modulation Frequency: Select 20 Frequencies between 10MHz and 100MHz
   Reference Lifetime: 4.3ns

5. When the lifetime is complete, please measure a steady-state spectrum of the fluorescein selecting emission wavelengths from 530nm to 620nm with a step size of 10nm. Please turn off the RF amplifier for this measurement and please set the slit size on the emission monochromator to 8.

6. Please repeat the same experiment using the Rhodamine B sample as the sample.

Spectral Measurement

1. Please prepare a solution containing 500ul of the student's Fluorescein sample and 1.5ml of the student's Rhodamine B solution. Load this solution into one of the 4.5ml cuvettes

2. Please mix the sample thoroughly and place it in the sample turret in the position 's'. The reference for this measurement will be the Fluorescein solution in 0.1N NaOH.

3. The TAs have prepared a method for you. Please load "P552 Spectral" from the user defined methods. Please acquaint yourself with the protocol so that you know what will be happening.

4. Please run the experiment.

5. When completed, please run a steady-state emission spectrum of the mixture selecting emission wavelengths from 530nm to 620nm with a step size of 10nm. Please turn off the blue RF amplifier for this measurement and please set the slit size on the emission monochromator to 8.

Questions

1. Prepare a polar plot at 60MHz.
2. Plot on the polar plot the coordinate for pure Fluorescein (sample) and pure Rhodamine B (sample). Please use the measured lifetimes for this calculation. Show your calculation of the polar coordinates for full credit
3. Plot the polar coordinates for all of the measured data points taken on the mixture at 60MHz from 530nm to 620nm. You can use the phase delay and modulation ratios directly from the *ifx file.
4. Please comment on you data. Are the polar coordinates taken from the sample containing the mixture at the various emission wavelengths where you would expect? Why?
5. On a single graph, please plot and label the emission spectra collected from the measurement of the fluorescein alone, the Rhodamine B alone and from the solution of the mixture. There are (3) spectra total for this graph.
6. Please perform the unmixing calculation. Report the values of the abundance vector describing the contribution from the Fluorescein and separately the Rhodamine B. Show your calculation for full credit. If you have written a script, please print it, label it and attach it to your report.
7. Please consider the measurement taken at 580nm and go through the following calculations.
    a. First, report the total intensity measured from the steady-state spectrum at this wavelength for the sample containing the mixture of Fluorescein and Rhodamine B
    b. Using the abundance coefficient for Fluorescein, calculate how much of the intensity from (A) is from Fluorescein.
    c. Using the abundance coefficient for Rhodamine B, calculate how much of the intensity from (A) is from Rhodamine B
    d. Using (A), (B), (C) and the known polar coordinates of Fluorescein and Rhodamine B, please simulate and plot the theoretical polar coordinate for

the sample containing the mixture of Fluorescein and Rhodamine B at the emission wavelength of 580nm and at a modulation frequency of 60MHz.

e. How did the simulation from (D) compare to the data? What could be possible sources of error in either the calculation or the measurement?

Reference

[1] Tsuri et al., "Seven-color fluorescence imaging of tissue samples based on Fourier spectroscopy and singular value decomposition" Journal of Histochemistry and Cytochemistry Vol. 48 No. 5, pp 653-662, 2000

Lab: Applying Mixing to Detect Lifetimes

Introduction

In the previous lab studying lifetimes, the class measured the lifetime of ruby in some very fundamental ways to become acquainted with the time domain and frequency domain methods for detecting lifetimes. In this lab, we will study how frequency mixing can be used to detect lifetimes. Frequency mixing is essential in order to measure lifetimes on the order of nanoseconds and also for lifetime imaging applications. In today's lab, you will learn to apply both the heterodyne and homodyne methods of frequency mixing to detect lifetimes.

Background

As you learned previously, when a sample is excited with light having its intensity sinusoidally modulated, the resulting emission of the sample also has its intensity sinusoidally modulated at the same frequency as the excitation light. There is a phase shift and demodulation in the intensity-modulated light emitted from the sample relative to the excitation light which is a result of the convolution of the fundamental fluorescence response of the sample with the excitation light.

Two mixing techniques called heterodyning and homodyning can be applied to simplify the frequency domain method for measuring lifetimes particularly when measuring lifetimes on the order of nanoseconds or using slow detectors such as CCDs . In both cases, the sinusoidally modulated emission signal of the sample is mixed with a signal being injected into the gain of the detector. For the homodyne case, the result of this mixing leads to a sequence of steady-state signals that can be observed to derive the lifetimes. For the case of heterodyning, a low frequency component is produced in the resulting mixed signal in the detector containing the relevant phase and modulation data to determine the lifetimes. As such, these mixing techniques simplify the analysis of a signal typically in the megahertz range to the detection of either a steady-state signal or a low frequency signal (on the order of hundreds of hertz).

To explain the usefulness of the mixing techniques described above, we will be begin with the function describing the intensity-modulated excitation light E(t), that you have see before,

$$E(t) = E_o + E_\omega \cos(\omega_E t + \varphi_E)$$

In this case, ω_E is the intensity modulation frequency of the exciting light and φ_E is the inherent phase of the instrument that will be corrected for with the reference standard.

In our samples, it is assumed that there is the possibility of having many fluorescing species. Each of these species has a characteristic fluorescence response to delta pulse excitation that defines its lifetime as shown below,

$$F_{\delta}(t) = \sum_i \alpha_i e^{\frac{-t}{\tau_i}}$$

Therefore, to determine the response of our samples to repetitively modulated excitation light, we need to convolute or spread $F_\delta(t)$ over the function describing the excitation light E(t) which leads to F_{meas}

$$F_{meas} = E_o \sum_i \alpha_i \tau_i + E_\omega \sum_i \frac{\alpha_i \tau_i}{\sqrt{1+(\omega\tau_i)^2}} \cos(\omega_E t + \varphi_E - \varphi_i^F)$$

The equation describing F_{meas} should be fairly familiar to the analogous equation studied in the ruby lab. In this case, the constants F_o and F_w have been solved for analytically. As before, this equation shows that the emission of the sample in response to an intensity-modulated excitation light also has its intensity modulated at the same frequency ω^E as the exciting light. The phase and modulation percentages that we will measure today come from the above summations.

The basis of the heterodyne and homodyne technique is to inject an additional radio frequency signal G(t), into the detector as the F_{meas} is being recorded. Here is G(t),

$$G(t) = G_o + G_\omega \cos(\omega_G t + \varphi_G)$$

The signal then that can be taken from the detector is therefore the product of G(t) and F_{meas}. For the heterodyne case, the frequency of G(t) only differs from the frequency of E(t) by a few hundred hertz. On the other hand, when applying homodyne methods, the frequency of G(t) equals the frequency of E(t). After low pass filtering (plugging in a trig identity if you try this yourself), the signal that is taken from the detector is,

$$\{G(t) * F_{meas}(t)\}_{LF} = G_o E_o \sum_i \alpha_i \tau_i + \frac{G_\omega E_\omega}{2} \sum_i \frac{\alpha_i \tau_i \cos((\omega_G - \omega_E)t - \varphi_E + \varphi_G + \varphi_i^F)}{\sqrt{1+(\omega^E \tau_i)^2}}$$

Despite the many terms in the equation, you can see that this equation is centered around the cosine term with the frequency of ω_E-ω_G. In homodyne detection, the frequency of the cosine term goes to zero (ω_E=ω_G). Therefore to determine the resulting phase and modulation percentage, the phase shift of the waveform injected into the detector (φ_G) is varied relative to φ_E. Typically φ_G is varied over a full period and the result your are left is a full period of the cosine function described above. This can be fit to figure out the phase and modulation percentage. When heterodyning is applied, ω_E-ω_G is very small on the order of hundreds of hertz. This frequency, ω_E-ω_G, remains constant throughout the experiment and allows for this low frequency component to be filtered for and detected. An analysis of this low frequency waveform (in a manner similar in concept to the ruby lab) can also be used to extract the relevant phase and modulation data that you are after.

Experiment (Measuring Nanosecond Lifetimes by Homodyning)

The experiment performed in this section will demonstrate how nanosecond lifetimes are detected using the homodyne method. For this, you will be using Prof. Clegg's fluorescence lifetime imaging instrument. We will measure a sample having a lifetime on the order of nanoseconds. You will measure at a single modulation frequency and then project the lifetime data gathered on the polar plot for visual analysis. Your TA will operate the FLIM instrument. However, please take note of all relevant components and scope outputs.

Data Acquisition

1. Open the program "PhaseDelayImaging".

2. Collect images of the dish of Rhodamine 6G at the following phase shifts of the detectors gain (0°, 45°, 90°, 135°, 180°, 225°, 270°, 315°). Your TA will assist you with the exposure times.

   Store the files with name **"Rhod6G_##_degree"** where ## is the detector phase that you are measuring at

   Please repeat (2) using the dish containing pure Rhodamine B.

   Store the files with name "**Rhodb_##_degree**" where ## is the detector phase that you are measuring at

Data Analysis (In-Class)

1. Open the MatLab code "homodyne_analysis.m" located in the folder that contains your data. As it runs, please select regions of interest on both the Rhodamine 6G and the Rhodamine B images when prompted

2. Please type "cftool" into the MatLab command window.

   Variables for fitting the Data

   Below is a description of the arrays that you will need for the fitting.

Variable Name	***Description***
angle_radians	detector phase written in radians
for_fit_Rhod6G_array	intensity data from Rhod6G's region
for_fit_RhodB_array	intensity data from RhodB's region

   Please write down the following in the space provided:

A) Equation (5) normalized to its DC offset with a single modulation depth (M_{Sample}) and phase (φ_{Sample})

B) (M_{Sample}) for Rhodamine 6G at 40MHz

C) (φ_{Sample}) for Rhodamine 6G at 40MHz

3. Fit the "angle radians" and "for_fit_Rhod6G_array" to the normalized version of equation (5) derived above and report the following values

$\frac{G_\omega E_\omega}{2G_o E_o}$	
φ_E	

4. Please fit the "angle_radians" and "for_fit_RhodB_array" to the normalized version of equation (5) now with the information gathered from (3). Please indicate the (M_{Sample}) and (φ_{Sample}) of the Rhodamine B below.

$M_{Sample,,RhodB}$	
$\varphi_{Sample,RhodB}$	

Experiment (Measuring Lifetimes by Heterodyning)

In this section of the lab we will demonstrate heterodyne technique visually by mixing the frequency applied to the excitation's intensity modulation (LED) with the CCD frame rate (30 frames/sec). To have a heterodyne with the frame rate, the intensity of the excitation light (LED) will be intensity-modulated as we have done in the previous lab. The LED is simply turned on and off at a desired frequency to achieve intensity modulation. The signal from the mixing of excitation's intensity modulation and the CCD

frame rate that we observe corresponds to the frequency $\Delta\omega$ that was applied to the excitation's intensity modulation. The low frequency heterodyne signal retains the modulation and phase information of the fluorescence response, which will allow us to extract the fluorescence lifetimes.

In this experiment, the mixing using the frame rate of the camera can be understood if two consecutive frames acquired by the camera are considered. It is assumed at the excitation light is being intensity modulated at a frequency near 30Hz. In these two frames, the high frequency components from the mixing expansion essentially cannot be distinguished in the two frames. In other words, the average intensities of the high frequency terms in the mixing expansion are nearly identical in the two frames. However, the average intensity of the slow term oscillating at the difference frequency $\Delta\omega$ is not the same in these two frames. You will actually see this average intensity (of the term oscillating in intensity at a frequency $\Delta\omega$) change with your eyes. An example using just the ruby of this visual heterodyne is shown in Figure 4.2.

Data Acquisition

1. Experiment with changing the frequency of the excitation's intensity modulation on the synthesizer. Try frequencies very close to 30Hz first and then move to about 32Hz. Write down your observations.

2. Set your excitation modulation (intensity) frequency to 29.5Hz on the synthesizer and record a movie using the Ken-A-Vision software

Data Analysis (In-Class)

1. Copy your movie (*.avi) onto the desktop of one of the data analysis computers. MatLab will already be open

2. In the MatLab code (movie_analysis.m), enter the requested information from the user at the beginning of the script including the filename, cross-correlation frequency (Δf) and the number of frames. Run the code.

   Running the Code

   1. Select at region of interest inside the ruby in the image by creating a polygon with the mouse (left clicks). Triple-click when you have finished (closed the polygon)

   2. Select a region of interest inside the Rhodamine cuvette in the image by creating a polygon with mouse in a similar manner. Triple-click to close the polygon.

   3. Save a copy of the image displaying your regions and the plot on the desktop with your names.

4. Type “cftool” into the MatLab command window to enter the curve fitting tool

Fitting the Data

1. Below is a table of the three arrays you will need for the fitting.

Variable Name	***Description***
time_arr	time axis written in radians
rhodb_arr	intensity data from RhodB's region
ruby_arr	intensity data from Ruby's region

2. Please fit the data describing the Rhodamine B according to equation (5) and assuming a lifetime of 0ms. Please report the value of $\varphi^G - \varphi^E$ = _

3. Using the $\varphi^G - \varphi^E$ determined previously, determine the phase φ_F of the ruby below and determine its lifetime.

$\varphi_{Sample,Ruby}$	
τ_{Ruby}	

Experiment (References for Nanosecond Lifetimes)

Picking a fluorophore as the reference to measure a lifetime in the range of nanoseconds can dramatically influence your ability to resolve the lifetime of interest. In this section, you will be measuring the lifetime of acridine orange (lifetime = 1.8ns) using a fluorescent reference and scatter as a reference. The solution called scatter contains glycogen suspended in water. It is non-fluorescent and can be considered to have a 0ns lifetime. The fluorescent sample that will be also used as a reference is fluorescein in 0.1N NaOH (lifetime = 4.3ns).

Data Acquisition: Fluorescent Reference

1. The Vinci software will already be open on the computer. Please place the solution of Acridine Orange in the sample chamber in the position labeled ‘s’ and the solution of Fluorescein in the position labeled ‘r’

2. Configure the software to scan 20 frequencies between 10MHz and 100MHz.

3. Please set the emission wavelength on the left emission monochromator to 530nm Please open the slits on the left emission monochromator to 16

4. Please enter the reference lifetime of fluorescein (4.3ns) into the software.

5. Please see appendix at end of lab to verify your settings in the software.

6. Please hit the green play button and begin the experiment

7. Save your data

Data Acquisition: Non-Fluorescent Reference

1. Please remove the solution of Fluorescein and put the solution (scatter) of glycogen in the sample holder in the position labeled 'r'.

2. Please set the emission wavelength for the reference to 440nm. Please keep the emission wavelength for the sample at 530nm.

3. Please see the appendix to verify your settings in the software

4. Please hit the green play button and begin the experiment

5. Save your data

Data Analysis (in-class)

1. Please enter the Vinci Analysis software. Please open one of your data files.

2. In the top toolbar, please select fitting and then lifetimes.

3. Please fit the data to a single component lifetime.

4. Please repeat steps (1-3) for both data sets

   Please record the lifetimes derived for each fit and the corresponding fit parameter in the following table

$\tau_{AcridineOrange}$	
χ^2	

$\tau_{AcridineOrange}$	

χ^2	

Questions

1. For the ruby lab, you used Rhodamine B as your reference. Rhodamine B has lifetime on the order of a few nanoseconds (as does Rhodamine 6G the reference for the homodyne experiment). Why can't we call the reference lifetime 0sec here as you did in the ruby lab?

2. Mention two criteria (photophysical parameters) that you would need to consider when picking an appropriate reference for a nanosecond lifetime measurement.

3. Our FLIM instrument employs only a single modulation frequency. Please think of an advantage to using a single modulation frequency. (You may consider the fact that we use it for imaging applications).

4. Please plot the (M_{Sample}) and (φ_{Sample}) for each of the two samples measured by homodyning (Rhodamine 6G (use calculations done in class) and Rhodamine B as polar coordinates on a polar plot with frequency of 40MHz.

5. What happened to the heterodyne signal when the chopping frequency is very close to 30 Hz? or right at 30 Hz?

6. Please draw a simple schematic of the experimental set up that you see here.

7. What would be a disadvantage of using a higher cross-correlation frequency here? For example 2 Hz? (Remember frame rate is fixed at 30 frames/second)

Figures

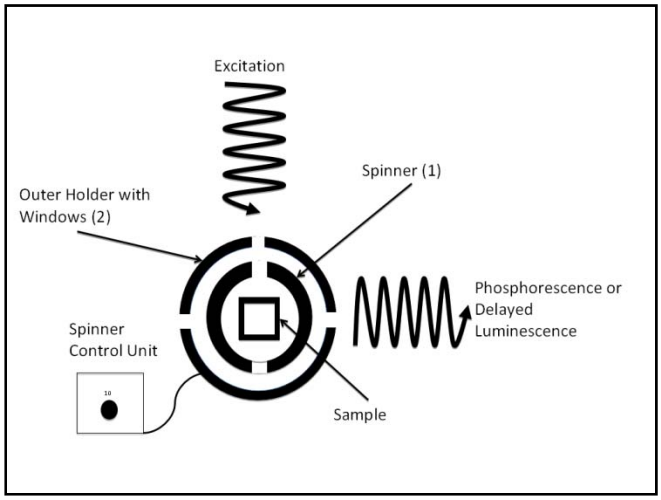

Figure 4.1: Phosphorescence attachment for the steady-state fluorometer: The outer ring (labeled as '2') of this device remains fixed during the experiment and contains three openings (windows) through which light can pass. The inner ring (labeled as '1') has two windows. As the inner ring spins at speeds defined by the user, the fluorescence emission of the sample can be collected at variable intervals following excitation. When emission is observed however, the exciting light is blocked and cannot be incident on the sample. (Diagram created by Kai Wen Teng and used here with his consent)

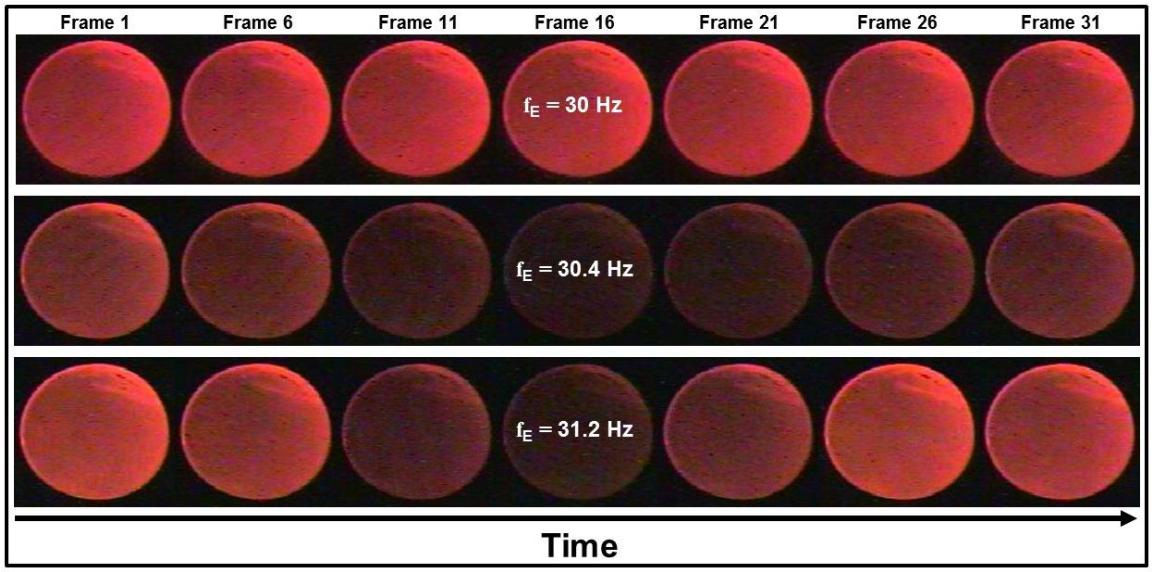

Figure 4.2: The detection of ruby's time-dependent fluorescence emission is performed by heterodyning using frame rate of the CCD camera (f_G = 30Hz): The low frequency response as a result of the frequency mixing is shown in the figure. When the excitation's intensity is modulated at 30Hz, a constant fluorescence emission is observed (top row). As the frequency of the excitation's intensity modulation is increased (two bottom rows), the detected fluorescence intensity oscillates more rapidly. The observed periods of oscillation are approximately consistent with the expected difference frequencies of 0.4Hz and 1.2Hz respectively.